

Geometry and Statistical Physics of Retinal Ganglion Cell Mosaics and Orientation Preference Maps

Eine Masterarbeit vorgelegt von **Manuel Schottdorf**
geboren am 29. März 1989 in Bad Kissingen



Institut für theoretische Physik und Astrophysik
der
Julius-Maximilians-Universität
Würzburg

am 1. Dezember 2012

Arbeit zum Erwerb des akademischen Grads Master of Science

Betreuer:

Prof. Dr. **Wolfgang Kinzel** (Lehrstuhl für Theoretische Physik 3)
Prof. Dr. **Fred Wolf** (MPI für Dynamik und Selbstorganisation)

CONTENTS

Contents	i
1 Introduction	1
2 Fundamentals	5
2.1 A Brief History of Neuroscience	6
2.2 The Visual System	9
2.3 Orientation Maps	18
2.4 Structure of this Thesis	20
3 Hexagonal RGC mosaics and OPMs	23
3.1 Introduction	24
3.2 Results	26
3.3 Discussion and Conclusion	50
3.4 Materials and Methods	53
4 Aperiodic RGC mosaics and OPMs	69
4.1 Introduction	70
4.2 Results	71
4.3 Discussion and Conclusion	85
5 Conclusions	87
5.1 Conclusion and Perspective	88
5.2 Zusammenfassung und Ausblick	90
5.3 Acknowledgements	92
Bibliography	93

INTRODUCTION

“Science is a graveyard of grand principles that fail in the end to explain the real world.”

Fred Guterl: “Searching for Clues to Calamity” [68]

1. INTRODUCTION

After more than 50 years of extensive study, we are still far away from a thorough understanding of the underlying neurocircuitry and the engineering principles of vision. The identification and classification of the neural inventory of the retina, the light sensitive organ in the eye, has advanced rapidly in the last years; some go as far as to say that it is “nearing completion” [110]. Many questions related to the visual cortex, however, remain unanswered. The visual cortex is part of the central nervous system, the brain. The difficulties in understanding the behavior of the brain on a microscopic level emerge from the huge number of elements and the massive interconnectivity of its constituents. About $8.6 \cdot 10^{11}$ neurons, interconnected by an estimated number of 10^{15} synapses process the information streaming continuously into the human mind [72]. Vision as one of the most basic senses has been predestined to scientific study, not only because sensory inputs can be easily provided but because the visual cortex is small compared to the rest of the brain. In many respects it might serve as a model system to advance the scientific understanding of the engineering principles of the brain. About 50 years ago David Hubel and Torsten Wiesel observed that cortical neurons are orientation selective and that the visual cortex of many animals is structured into maps of similar response properties, most prominently, maps of orientation preference (OPMs). Although firstly described 50 years ago, the underlying engineering principles of OPMs are still not well understood. The topic of this thesis is the analytic and numeric study of a model for OPM emergence recently proposed, using an interference effect of retinal ganglion cell (RGC) mosaics to drive OPM formation. This model is a novelty because it rejects cortical self-organization as pivotal for OPM formation and substitutes an experience-independent mechanism in the retino-thalamic pathway. Consequently, should this model hold, the importance of intra-cortical organization might have been substantially overestimated. In this thesis, we analyze the statistical and geometrical properties of retinal ganglion cell mosaics, cortical orientation preference maps and their interaction. We rely on both, exact results and Monte-Carlo simulations for the comparison of model properties with experimental data.

The **first chapter** of this thesis contains a detailed introduction which is intended to give the reader the necessary background information to understand the findings of chapters two and three. The first part summarizes the history of neuroscience briefly. It illustrates where the field stands and which challenges remain to contextualize this thesis’ findings. The second part describes the visual system. It summarizes physiological and neuroscientific facts and experimental evidence which we build on in the following chapters to interpret our findings. In the **second chapter** of this thesis, we describe the model for OPM emergence. We solve it analytically and analyze perturbative effects using numerical tools. Our findings challenge the model which we try to improve subsequently. In the **third chapter**, we introduce a slightly modified approach which has certain advantages over the original model. However, we

still find model predictions which are distinct from experimental results. The **conclusions** summarize the results of the chapters two and three, give a perspective on the interpretation of this thesis' findings and comment on future work to do.

This thesis presents a series of arguments which lead to the conclusion that this newly proposed model is insufficient to understand the emergence of OPMs. Consequently, experience-dependent and self-organizing processes are essential for OPM formation. Despite the model's flaws, it is reasonable to assume that an external retino-thalamic bias has an influence on OPM formation. Thus, the next logical step is the integration of an external bias into self-organization models. It might well be that this (presumably noisy) bias is essential to account for some of the properties of the spatial layout of OPMs.

FUNDAMENTALS

“By [the brain], in an especial manner, we acquire wisdom and knowledge, and see and hear and know [...]. But by the same organ we become mad and delirious and fears and terrors assail us. All these things we endure from the brain when it is not healthy. [...]. In these ways I am of the opinion that the brain exercises the greatest power in the man.”

Hippocrates: “On the Sacred Disease” [74]

2. FUNDAMENTALS

2.1 A BRIEF HISTORY OF NEUROSCIENCE

The oldest archeological record of cranial surgery dates back to the 6th millennium BC. A hole was drilled into a human skull, laying open the brain. Healing indicates a substantial period of time for which the “patient” survived [3]. Due to missing written records, it is difficult to say why these trephinations have been performed. Despite a great deal of speculations as to the reasons, a comparison with native african communities allows to guess potential motives. The most prominent ones are therapeutic in the sense of removing bone fragments after a fracture and to cure headaches, epilepsy and mental disorders by allowing evil spirits to escape [3, 58]. It should be noted that similar procedures have been performed in medieval Europe as the removal of the *Stone of Madness* in Hieronymus Bosch’s painting reminds us. After this brief side note regarding the history of cranial surgery, we begin the history of neuroscience in the time of the ancient civilizations where written records allow us to trace the advancements made.

The first preserved record containing an anatomic description of the brain is in the “*Edwin Smith Papyrus*” from around 1550 BC which is a surgical text containing medical procedures and treatments for various conditions [157]. Despite their rich medical knowledge, physicians of ancient Egypt considered the heart to be the seat of mind, perception and memory. Their knowledge regarding anatomy originated in religious tradition and no clear line can be drawn between priests, magicians and physicians. Cutting open the body, dissecting organs and finally mummifying the dead did not only create a vast knowledge of the human frame but served one greater goal: achieving immortality. This specifically religious component, interfering with a *scientific* study of the body, stands in contrast with the relatively modern modus operandi of ancient Greek philosophers and physicians. In this part of the world, driven by curiosity rather than religiousness, two philosophical schools challenged each other: Hippocrates taught that the brain is the location of the human mind [74]. On the other side there is one of Hippocrates’ contemporaries, Aristotle. In his view, the heart is the seat of intellect. The reason for this opinion, beside others, is that the heart is connected to all parts of the body; it is essential to life and the last organ to stop working before death [67]. Despite disagreement on anatomical details, both agreed that it is the bodily fluids which contain sensations and which generate mental states; with the brain either as center of the sensations, or as radiator for cooling of blood, overheated by the heart. Greek physicians as *Herophilos* and *Erasistratus* systematically performed human dissections and are considered early pioneers of the scientific method [14, Chapter 15]. Their experimental knowledge laid the foundation of the philosophical dispute on the nature of the mental phenomena. Sadly, most of their knowledge regarding physiology and anatomy has been lost. Major parts of what we know about them is quoted in Galenus’ work, a Roman physician who lived around 150 AD [46]. Advancing previous theories,

2.1. A Brief History of Neuroscience

he tried to combine the notion of the brain being the seat of mind with the doctrine of vital fluids. He described cavities, filled with cerebral liquid in the brain. Today we call these cavities ventricles. His observation fit the prevailing theory that the body operates according to a balance of vital fluids. The sensations were thought of a movement of liquids to the brain via nerves. Consequently, he predicted that nerves are in fact hollow tubes, just like blood vessels which transport the vital fluids to the cavities of the brain. He claimed to have observed this nervous cavity, however, further study became increasingly difficult. The introduction of Christianity made it impossible to continue the systematic study of anatomy and to test the prediction of hollow nerve fibers [142]. The transition back to a religious paradigm stopped the empirical and scientific inquiry for the sake of sanctity and Galenus' theory was not challenged. His theory was philosophically advanced and christianized by Albertus Magnus, a philosopher and Doctor of the Church who assigned mental functions to the cranial ventricles [107, 108]. Remarkably, Galenus' teachings should prevail the next thousand years until the early modern ages.

With the upcoming Renaissance, dissections of animals as well as human corpses became possible again and outstanding figures as Leonardo da Vinci [136] and Andreas Vesalius [169] worked on detailed anatomic studies (both around 1500 until 1550). Their experimental approach advanced the knowledge of the brain rapidly, finally allowing the experimental test of Galenus' theory. Around 1550, Andreas Vesalius remarked that he could not find any cavity in a nerve.

“I am unable to differentiate nerves by the cavity within them as I have never seen such a cavity or channel, even in the optic nerve.”

Andreas Vesalius: “On the Fabric of the Human Body” [169, p. 165]

Yet, it could have been that the cavities are just very small; and so Vesalius' findings were not considered evidence enough. About one hundred years later, the Dutch scientist Antonie van Leeuwenhoek found that even using his newly constructed first light microscope, he cannot find a cavity inside the nerves. In a paper published in the philosophical transactions of the royal society, he writes

“Having acquainted Dr. Schravesande, that I could not perceive no cavity in the Optic Nerve, he told me, that Galen had on a clear sunshiny day seen a hollowness therein, encouraging me to view that Nerve again with more attention [...]. These holes or cavities being in the dried Nerve, I am of the same opinion still (as I was before) that the nerve or fibers are made up of soft fluid globules.”

A. van Leeuwenhoek: “Microscopical Observations of Mr. Leewen-hoeck, concerning the Optic Nerve” [102]

2. FUNDAMENTALS

With the advancements of microscopy after van Leeuwenhoek, Felice Fontana studied individual nerve fibers and is said to be the first scientist to describe the axon of a nerve cell as a distinct feature in 1781 [65]. Despite all experimental evidence, philosophers continued to advance the theory of hydraulically controlled mechanics and the fluid-mechanical theory of the brain function, specifically Rene Descartes [59].

The artificial generation of electrostatic charge using the newly invented influence machine, constructed by Francis Hauksbee in 1706, allowed Luigi Galvani in the second half of the 18th century to show that muscles twitch when nerves are stimulated electrically [137, 168]. With the end of the 18th century, the nervous system had been completely dissected and described macroscopically. Combined with the observations of the electrical nature of the brain, the fluid-mechanical model which prevailed for about 1800 years was finally abandoned. Following the dawn of modern science, advancements have been made rapidly. In 1839 Theodor Schwann presented the cellular theory that all tissue is made of microscopic cells [52, 112, 149, 170], although the notion of cells is said [92] to date back to the 17th century [75]. However, to confirm this theory, advanced coloring techniques and microscopy were necessary. In particular the nervous system has been thought of as a network of different cells fused together like blood vessels of the circulatory system. This notion is quoted as Joseph von Gerlach's idea in a review from 2007 [41, 61]. It is of course very appealing since it offers a simple explanation as to the transport of information across the cellular network. Advancements in staining techniques made by Camillo Golgi, in particular Golgi's famous method of silver impregnation introduced in 1872 [64] as described by [112] allowed to show that nerve cells are in fact individual units. This discovery follows from Cajal's work [23] as described in the same review. Building upon this discovery, the term "synapse" was introduced by Arthur Sherrington and Michael Foster to name the contact between individual nerve cells [57]. For their discoveries, Santiago Ramón y Cajal and Camillo Golgi were awarded the 1906 Nobel Prize in Medicine or Physiology "in recognition of their work on the structure of the nervous system".

New technologies using electricity made it possible to analyze the electrical activity of nerve cells. In the middle of the 19th century, Carlo Matteucci showed that biological tissue generates electricity. Trying to verify these findings, Emil du Bois Reymond discovered the action potential in 1848 [15] and Hermann von Helmholtz measured the conduction velocity of action potentials on a frog nerve fiber [70, 71]. Nernst's work on ion movements [122] allowed him and Bernstein [9, 123] to develop an early model for action potentials by ion currents across the plasma membrane. With the invention of the oscilloscope briefly after the first World War, Joseph Erlanger and Hermann Gasser measured the exact shape of an action potential in 1922. Both have been awarded the Nobel Prize in 1944. In the following years, action potentials have been found and studied in various species. Scientists thought that they

are generated by an ion gradient across the cellular membrane, however, no concrete model was available. This notion goes back to work of Julius Bernstein and Hermann Helmholtz as we saw. Finally, Hodgkin and Huxley built an effective model of action potential generation by voltage dependent ionic conductivity within the cellular membrane. This model allowed them to describe the shape of the action potential measured in a giant squid axon. Both Hodgkin and Huxley have been awarded the Nobel Prize in 1963. The underlying physiological reasons were described by Neher and Sakman using the newly invented Patch-Clamp technique. Modern technologies and the knowledge of the electric nature and the cellular inventory of nervous tissue allowed a new field of study, the systematic analysis of the brain's working principles. Using simple tools as pointy electrodes, David Hubel and Torsten Wiesel analyzed the mammalian visual system: presenting a visual stimulus allowed to measure the electrical response of nerve cells. Thus, for the first time, scientists observed the brain processing information. For their ground breaking work on the visual system both have been awarded the Nobel Prize in 1981. In the next section on the structure of the visual system, most of the findings presented are results of their research or directly related to their work. Today, we have reached a state of knowledge which allows to reconstruct speech from human auditory cortex activity [135] and to reconstruct vision from visual cortex activity [125] but despite the remarkable advancements in the last hundred years, many questions remain unanswered.

Since this thesis focuses on the visual system, we stop our brief review of the history of neuroscience here and continue to describe the layout of this particular sensory system. Following the next section, we present the question addressed in this thesis.

2.2 THE VISUAL SYSTEM

The visual system is the most intensively studied sensory system in mammals. The fundamental visual system consists of three major parts. Firstly, there is the eye with an embedded light sensitive organ, the *retina*. Nerve fibers originating in the retina project to a region in the thalamus, the *lateral geniculate nucleus*. From there, axons project to the *primary visual cortex*. In the primary visual cortex, the received information is processed in a way we discuss later. We focus on the properties of this information processing. In the next three sections, we describe each instance of the visual pathway.

The Eye & the Retina

The first element of the visual pathway is the eye. A sketch is shown in **Fig. 2.1A**. It is a simple imaging system with variational focal length and variational aperture. Incoming light is imaged upside-down onto an organ specialized in light detection: the retina. In the retina, *rod* and *cone* cells convert

2. FUNDAMENTALS

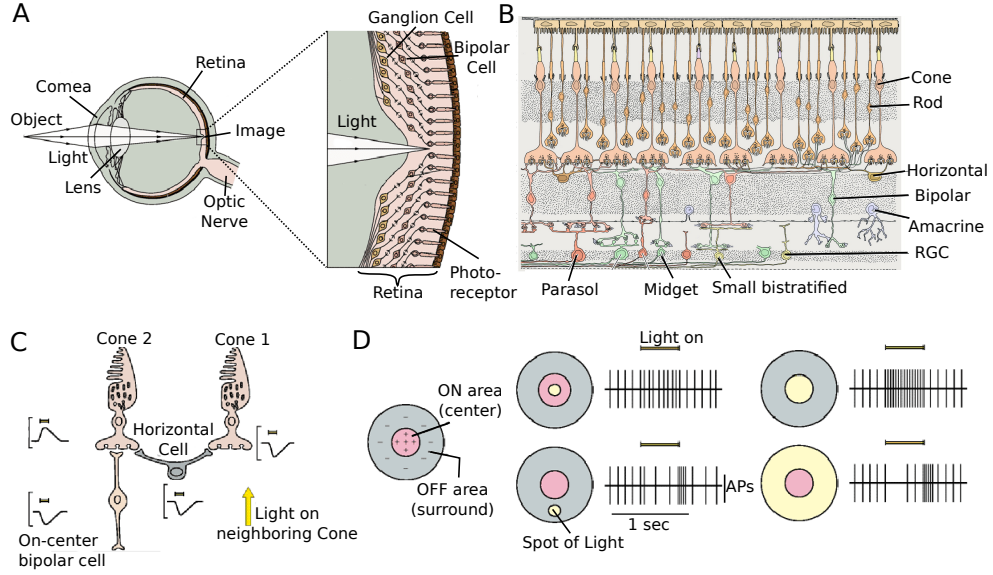


Figure 2.1: **A** A saggital cut through the eye and the retina. **B** The cellular inventory of the primate retina. Light enters from below. **C** Neuro circuitry of the retina. Cone one hyperpolarizes a horizontal cell. The hyperpolarized horizontal cell depolarizes cone two. Thus, a light stimulus on cone one is inhibitory for the shown ON center bipolar cell and inhibitory for the connected RGC (not shown). The insets show the intracellular potential. **D** Receptive field of an ON ganglion cell. A illumination pattern (left) creates a certain spike train in the ganglion cells (right). The bar corresponds to the time span where a stimulus is presented. The figures are copied and adapted from [89] and [54].

a light stimulus to an electric signal. Rods, cones and the subsequent layers of the mammalian retina are shown in **Fig. 2.1B**. Rods are extremely sensitive for white light, yet with a small temporal resolution. One photosensitive pigment is responsible for an achromatic response. The rods' black-white vision with high sensitivity is what allows light perception at night. There are about 20 times more rods than cones. Cones are less light sensitive, have a high temporal resolution and are responsible for day vision. They are equipped with different photopigments, thus capable of distinguishing colors. Three different pigments in cones allow us to sample from three different primary colors. Rod and cone cells do not generate action potentials. The voltage across the membrane increases in response to light. The pixel-information in rod and cone cells is subsequently processed by three types of neurons, *horizontal cells*, *bipolar cells* and *amacrine cells*, before it is processed and communicated to the brain by *retinal ganglion cells* (RGCs). Bipolar cells sample directly from rods and cones. The increase in cellular potential in

cones causes a decrease in glutamate release to the bipolar cells. There are two types of bipolar cells, depending on their ion channel inventory. One type is hyperpolarized, the other type is depolarized by glutamate. Therefore there are bipolar cells activated by light (ON center bipolar cells) and bipolar cells activated by a lack of light (OFF center bipolar cells). As rods and cones, bipolar cells do not generate action potentials. Retinal ganglion cells sample from bipolar cells and generate action potentials. RGCs project directly to the brain.

As RGCs collect information from many rods and cones, their *receptive field* is no longer dot-like. The receptive field is the region on the surface of the retina which is stimulus sensitive. The microcircuitry responsible for the ganglion cell's receptive fields is shown in **Fig. 2.1C**. The response of cone 1 to illumination is inverted by the horizontal cell. Subsequently, the horizontal cell depolarizes cone 2. Therefore a stimulation of cone 1 is inhibitory for cone 2. The circuitry generates a very characteristic receptive field. Ganglion cells respond with a high firing rate to a spot of light in a central region surrounded by a dark annulus (ON center) or vice versa: a dark spot in the center surrounded by a bright annulus (OFF center). Note that a uniform illumination does not generate activity. This so called *center-surround* structure is illustrated in **Fig. 2.1D**. The left section shows an ON center cell, the right section an illumination and the corresponding spike train. A central illumination increases the firing rate, an illumination in the surround decreases it. In the center of the retina, the typical size of the receptive field's central region is a few minutes of arc for the primate retina. At the periphery of the retina, the typical size increases to 3 to 5 degrees [89].

In general there are three types of retinal ganglion cells in the primate retina, distinguished by their receptive fields: *parasol cells* (10%), *midget cells* (80%) and *small bistratified cells* (10%). Both parasol and midget cells have a center surround receptive field, although the receptive field of parasol cells is much larger. Bistratified RGCs have no surround region and react to an overall change in luminosity. As rods and cones are interconnected by horizontal cells, retinal ganglion cells are interconnected by amacrine cells. There are about 30 different types of amacrine cells which are highly specialized. For example, the dopaminergic amacrine cells adjust the retina's responsiveness under bright and dim light [110]. Most of the retina can be considered a black-box because there are no projections from the brain to the retina. In this thesis, we therefore assume the retina to deliver exclusively center-surround input into the brain. The situation for primates presented here [54] is very similar for the cat although the nomenclature is different [156, 164]. What is called a midget cell in the primate retina is called a X-cell in the cat retina. Accordingly a parasol cell is called a Y-cell [40, p. 54]. X-cells have a small linearly summing receptive field, Y-cells have a larger and non-linear receptive field [110]. Midget and parasol cells are distinguished according to the shape of their receptive fields, as are X- and Y-cells. However, the cells are

2. FUNDAMENTALS

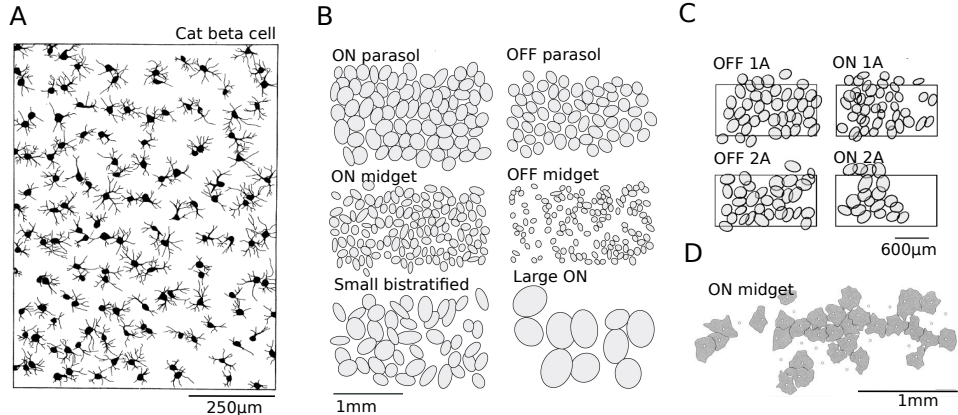


Figure 2.2: **A** Section of the beta cell mosaic of a cat. This is the mosaic which, among others, is used in the second half of this thesis [172]. **B** Receptive field mosaic of a primate retina. Shown are contours of 1.3σ to Gaussian fits [54]. **C** Receptive field mosaic of a rat [5]. **D** The mosaic of dendritic trees of neurobiotin labeled midget cells in a human retina [36].

also distinguished histologically/morphologically. What is called a Y-cell in electrophysiology is an alpha cell in morphology, similarly X-cells are called beta cells [110, 162]. Note, however, that ON and OFF cells are neither histologically nor structurally distinguishable. To distinguish between an ON and an OFF center ganglion cell, usually electrophysiology is employed.

For this thesis we focus on RGCs and their mosaics. There is plenty of information available for different species as humans [36, 37], rabbits [44], rats [5, 147] and cats [172, 174, 175]. Examples for different ganglion cell mosaics is given in the following figures. **Fig. 2.2A** shows the beta cell mosaic of a cat. This figure shows the somata positions [172]. **Fig. 2.2B** shows the receptive field mosaic of a primate. This figure does not show the ganglion cells' somata but a contour of 1.3σ to a Gaussian fit to the receptive fields, measured with an electrode array [54]. We refer to this figure as *receptive field mosaic*. **Fig. 2.2C** shows the receptive field mosaic of a rat. As with primates and cats, there are different types of receptive fields [5]. **Fig. 2.2D** shows a human inner midget cell mosaic. Indicated are dendritic trees of cells, labeled with neurobiotin. Inner midget cells are considered to be ON type RGCs although this is not certain without an electrophysiological measurement [36]. A common model for the shape of a receptive field's center is a Gaussian as we have seen in **Fig. 2.2**. A model for the entire receptive field, taking the surround into account, is the difference of two Gaussians [42, 49, 145, 183]. This model is quite successful, however, on a fine scale receptive fields are not as regular [60]. A complete cat's alpha cell mosaic is shown in **Fig. 4.1** in chapter 4.2. The ganglion cell's axons form the optic nerve. The two optic nerves meet in

2.2. The Visual System

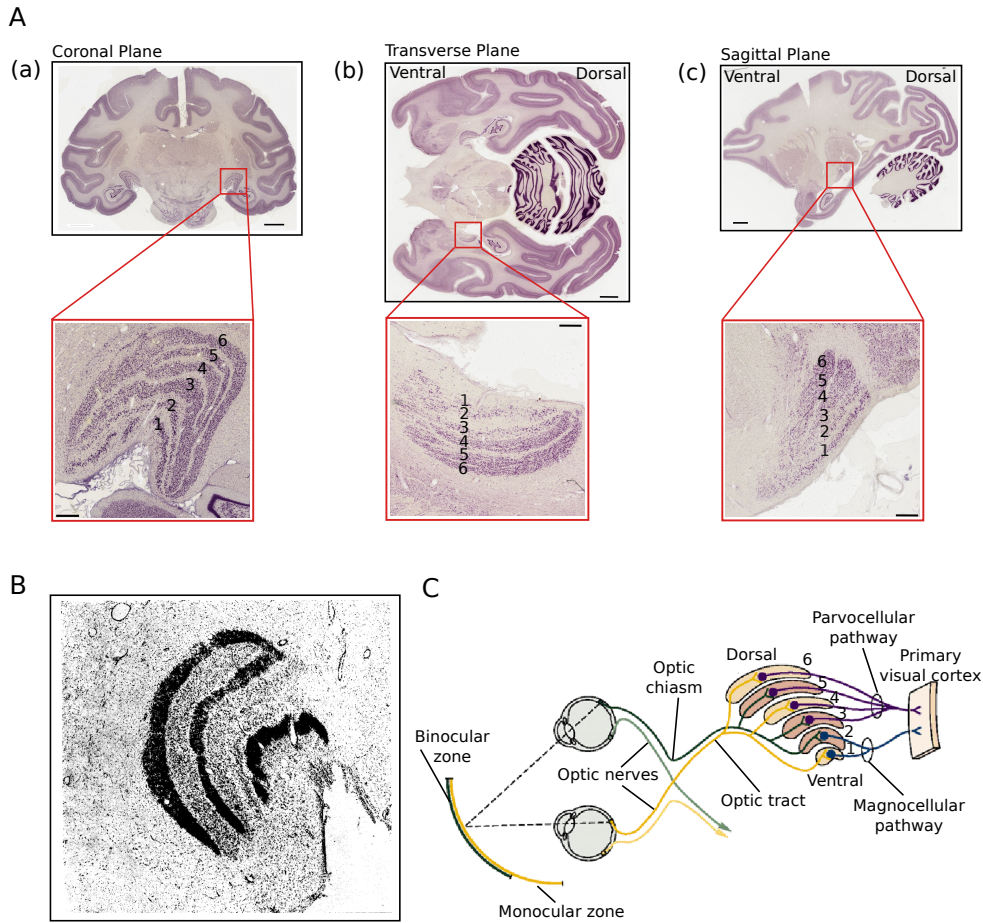


Figure 2.3: **A** Three cuts through a nissl stained adult macaca mulatta brain. Data from brainmaps.org [115]. **(a)** A coronal cut. The inset shows the position of the LGN. The magnified region is shown below. The characteristic 6 layers are numbered. The scale bars correspond to 0.5 cm and 0.5 mm respectively. **(b)** Same figure as (a) of a transverse cut through the brain. **(c)** Same figure as (a) and (b) of a sagittal cut through the brain. **B** Autoradiograph of a monkey LGN. Label injected into right eye [83]. **C** Position of the LGN in the visual pathway [89].

the optic chiasm where the nasal sides of the image are interchanged. The optic tract projects to the thalamus, in particular the *lateral geniculate nucleus* (LGN). This is the first region of the brain where retinal input arrives.

2. FUNDAMENTALS

The LGN

The nissl stained lateral geniculate nucleus, a region of the thalamus, of a macaque monkey is shown in **Fig. 2.3A (a)-(c)**. It shows coronal (a), transversal (b) and saggital (c) cuts through the brain. The location of one of the two LGNs is indicated by the red box and magnified below. Nissl's technique is a nucleic acid staining method, labeling specifically a neuron's soma. Thus, it is a good labeling technique for the cell-body rich gray matter and the LGN. The characteristic six layer structure (layer one to layer six) of the LGN is illustrated in the magnified images.

The neurons of the LGN are connected with axons of retinal ganglion cells. This connection can be measured by injecting radioactive nutrients into an eye which are absorbed by the RGCs and transported along the axon to the LGN. The autoradiograph of a monkey LGN after application of tritiated proline and tritiated fucosein is shown in **Fig. 2.3B**. The radioactive marker has been injected in one eye only. The stripe structure shows prominent ocular dominance layers in the LGN [83]. Using similar techniques, it turns out that parasol cells are connected the cells of the *magnocellular pathway* and midget cells are connected to cells of the *parvocellular pathway*, two distinct parallel pathways to the visual cortex¹. The six histologically distinct layers of the LGN are organized in four layers of the parvocellular pathway and two layers of the magnocellular pathway. The organization of the LGN's neural layers is schematically shown in **Fig. 2.3C** [89].

Neurons of the magnocellular pathway are not color sensitive, however, respond to a low luminance contrast. P-cells are color sensitive and require a great luminance contrast and high spacial frequency. A loss of P-cells leads to a complete loss of color vision. A third type is the *keniocellular pathway* to which bistratified retinal ganglion cells are connected. Their receptive field is very large in comparison to magnocellular and parvocellular neurons. LGN neurons have the same center-surround receptive fields as retinal neurons. This similarity is the main reason for modeling the LGN as relay station. It is remarkable to note that only about 10%-20% of the synaptic connections to LGN neurons originate in the retina. The vast majority originate in different regions of the brain, including feedback from the brain stem and the cortex. In this sense the function of the LGN is not clear at all [89]. Axons leaving the LGN follow the optic radiation to primary visual cortex.

The Visual Cortex

The *cortex* is the outermost layer of the mammalian brain. For the major part, it is composed of cell bodies and unmyelinated fibers. It is synonymously

¹ Alternatively, geniculate neurons of the parvocellular pathway are called P-cells. Neurons of the magnocellular pathway are called M-cells.

2.2. The Visual System

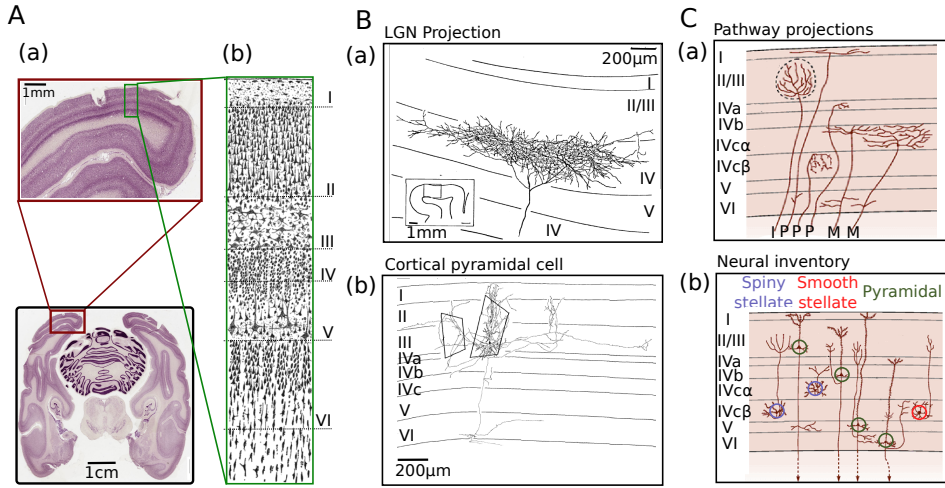


Figure 2.4: **A** Neuroanatomy of the visual cortex. (a) Transverse cut through a nissl stained M. Mulatta brain. The position of the visual cortex is indicated and magnified. The gray/white matter composition is clearly visible. Images are copied from brainmaps.org [115]. (b) Semischematic drawing of a nissl stained human visual cortex with indicated layers [22]. **B** Circuitry in the cortex. (a) LGN projects to primary visual cortex. Shown is a rapid Golgi stained cat geniculate afferent [103]. (b) Horseradish Peroxidase labeled pyramidal cell in the macaque primary visual cortex [113]. **C** Schematic illustration of the cortex. (a) Parvocellular, magnocellular and intralaminar neurons of LGN project to different layers of V1. (b) Neural inventory of the cortex. Pyramidal cells can project to different regions of the brain. Spiny and smooth stellate cells are local. Smooth ones are inhibitory. Spiny stellate and pyramidal cells are excitatory [89].

called *gray matter* in contrast to the myelinated nerve fibers connecting distant regions of the brain, called *white matter* which make out major parts of the brain's interior. The high cellular density makes the cortex stand out in a Nissl stain as shown in **Fig. 2.4A (a)**. The image shows a transverse cut through a Macaque monkey's brain. The red box shows the position of the primary visual cortex. In the magnified image of the red box shown above, the cortex appears as purple substance. Corresponding to the two cerebral hemispheres, mammals have two visual cortices on both occipital lobes. The visual cortex consists of the primary visual cortex or striate cortex, also called V1 and extrastriate visual cortical areas, named as V2, V3 … V5. The primary visual cortex is about 1 mm thick (see figure) and consists of several distinct layers of tissue. A common numbering scheme is the one developed by Brodmann [21]. In this scheme, there are six layers of cortical tissue, shown in the sketch in **Fig. 2.4A (b)** [22]. The first outermost layer is a dense layer,

2. FUNDAMENTALS

almost without cellular bodies, formed from axons and dendrites of layer II to V pyramidal cells. A small number of inputs from the parvocellular pathway arrives here. Layers II and III contain somata and dendrites of pyramidal cells. Layer II receives relatively little LGN input and is sparsely connected to layer IV in contrast to layer III which is heavily interconnected with layer IV. Layer IVA does not contain any pyramidal cells which distinguishes it from layer III. Layer IVB has a low cell density, followed by Layer IVC with a high cell density. Layer IVC is important for conveying information of the visual pathways and is subdivided into IVC α and IVC β . Layer IVC α is the layer the magnocellular pathway projects to; IVC β is the layer for the parvocellular pathway. There is substantial feedback from layer IVC α to layer IVB. Layer V neurons project primarily to layers III and I. Layer VI sends axons to IVC β and some back to the LGN. Layer VI also receives direct input from the LGN [100]. The layer boundaries are not strict. They should rather be considered as an over-the-thumb mesoscopic neuroanatomic structure. Furthermore, this numbering scheme is not the only one in the scientific community. Several alternatives have been proposed [22]. We follow this numbering scheme because it is the most common one [89].

Despite the massive feedback from the visual cortex to the LGN, analyzing thalamic projections gives a hint as to the information flow. In general, the LGN projects to the middle layers whereas feedback fibers originate in the upper and lower layers. **Fig. 2.4B (a)** shows a LGN projection into the cortex in a cat's brain. This projection terminates in layer IV. **Fig. 2.4B (b)** shows a layer III pyramidal cell with its horizontal connections, labeled by the injection of horseradish peroxidase. It forms synaptic connections to cells in the vicinity and to more distant cells. Such experiments allow to analyze the circuitry of the visual cortex.

As explained above and shown in **Fig. 2.4C (a)**, M- and P-cells of the two major visual pathways project to different layers [89]. The neural inventory of the visual cortex is morphologically complex, however there are two primary types of neurons: inhibitory interneurons and excitatory neurons. Pyramidal cells are excitatory and can contact distant regions in the brain. They are usually larger than the highly localized interneurons. Stellate neurons can be excitatory or inhibitory and are highly localized. This is illustrated in **Fig. 2.4C (b)**. Cells of the primary visual cortex have substantially different receptive fields, compared to thalamic or retinal neurons. Cortical receptive fields are elongated with specific ON and OFF regions [141] as shown in **Fig. 2.5A (b)**. The corresponding data is measured by insertion of an electrode into the cortical tissue while simultaneously presenting a stimulus **Fig. 2.5A (a)**. Elongated receptive fields are orientation selective. Presenting a grating stimulus of different orientations evokes different responses, see **Fig. 2.5B**. Plotting the total firing rate of a cortical neuron as a function of the stimulus orientation gives a *tuning curve*, as shown in **Fig. 2.5C**. The drawn line is a Gaussian fit to the measured response.

2.2. The Visual System

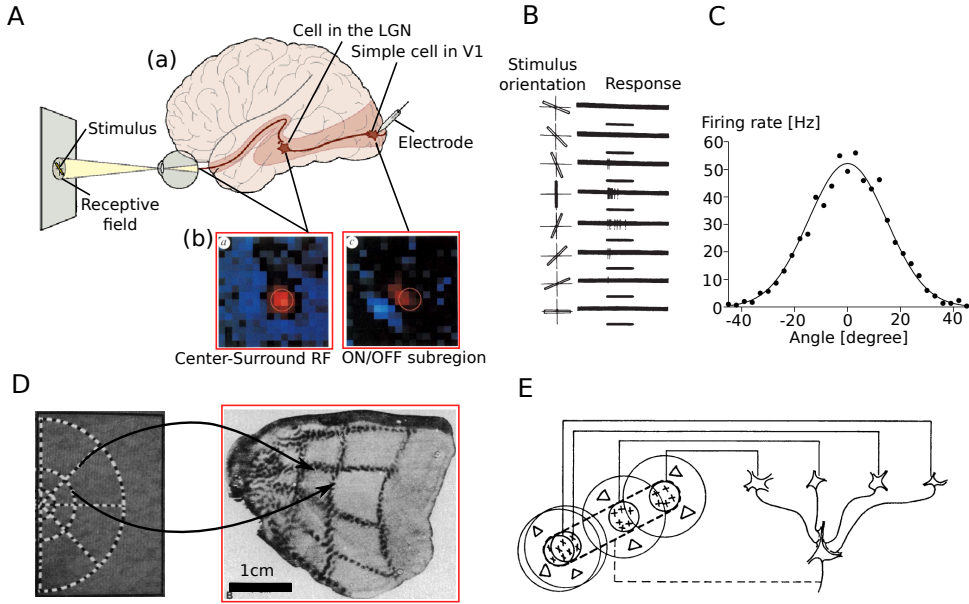


Figure 2.5: **A** Sketch of the visual systems. **(a)** The three stations of the visual pathway: Eye, LGN and V1 [89]. **(b)** Retinal and geniculate receptive fields have a center-surround structure. Cortical receptive field are elongated with distinct subregions [141]. **B** A bar stimulus in different orientations (left) evokes different responses in a cortical neuron (right) [82]. **C** The measured firing rate of a cortical neuron as function of the orientation of a stimulus (dots); drawn is a Gaussian fit of width $\sigma = 15^\circ$ [40]. **D** An object (left) creates an excitation in the visual cortex (right), measured as autoradiograph with labeled glucose [163]. **E** A linear sum of center-surround receptive fields of LGN neurons has the shape of a cortical receptive field [80].

A second important feature of cortical neurons is that they mirror retinal inputs topographically. This is called *retinotopy*. **Fig. 2.5D** shows a stimulus presented to a monkey and **Fig. 2.5C** the cortical response to that stimulus, measured with an autoradiograph, obtained by metabolization of radioactive glucose [163]. The pattern is distorted by *cortical magnification*, however, there is a one-to-one correspondence between a point in visual space and a point on the cortex. The cortical magnification is usually expressed in millimeters on the cortex per degree visual angle. This value varies roughly by a factor of 100 between regions of the cortex, connected with the fovea or peripheral parts of the retina [38, 109]. The response properties of cortical neurons in different layers are similar. In this sense, the cortex is a two dimensional sheet.

An early proposal to model cortical receptive fields is by linear summation of geniculate projections. Adding several center-surround receptive fields at

2. FUNDAMENTALS

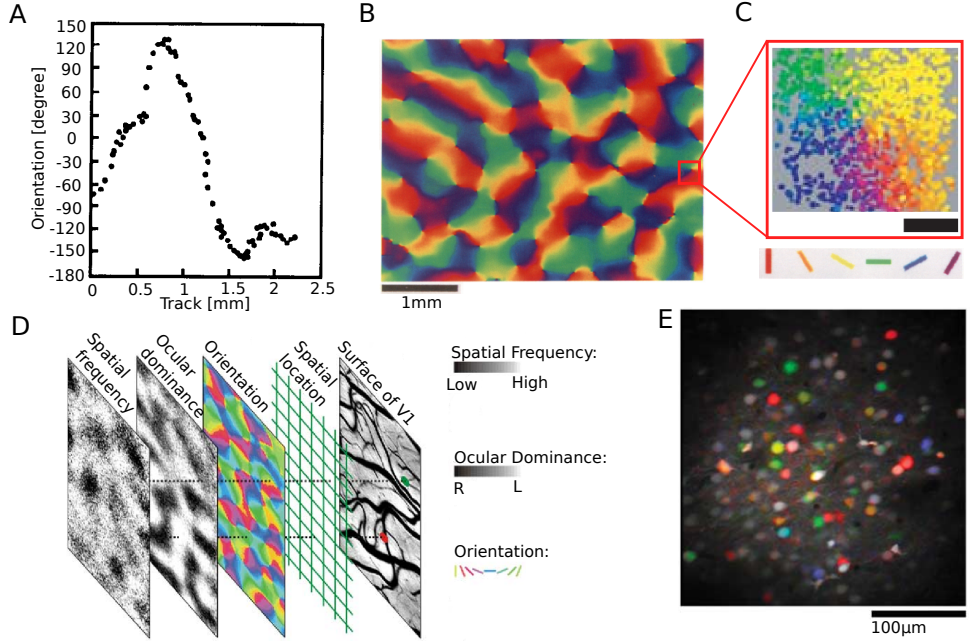


Figure 2.6: **A** Orientation preference measured with an electrode tangentially penetrating a monkey visual cortex [12]. **B** A map of orientation preference measured with optical methods in a monkey [12]. **C** Magnification of a topological defect: the singularity is well defined on a single cell level. This measurement has been done with two-photon microscopy in the cat visual cortex. Scale is 100 μm [130]. Note that this is not an actual inset of B but illustrates the cellular structure of a pinwheel. **D** As with orientation, the surface of the cortex is subdivided into maps of preferred spatial frequency and ocular dominance. **E** Orientation preference of neurons in rat primary visual cortex measured with two-photon microscopy. There is no map-like organization [129].

different points in visual space generates an elongated structure as shown in **Fig. 2.5E**. Combining this idea with retinotopy implies, that the local orientation preference is determined by the ganglion cell mosaic. Discussing this question is the focus of this thesis.

2.3 ORIENTATION MAPS

As already explained, the response properties of neurons perpendicular to the cortex' surface are similar. Their orientation preferences match. Tangentially, the preferred orientation changes [12, 80, 82]. This is shown in **Fig. 2.6A**. Following these early electrode penetration experiments, new optical methods allowed to image maps of preferred orientations. Briefly, a grating is presented

2.3. Orientation Maps

to the test object. Neurons of this orientation preference become active. This activation is visible in optical absorption imaging. Taking several pictures of the visual cortex for different grating orientations allows to draw a map of preferred orientation without penetration of the cortex [12]. These experiments revealed a remarkable structure of the visual cortex. An example for a primate visual cortex is shown in **Fig. 2.6B**. An orientation preference map as the one shown has topological singularities, so called pinwheels, embedded. Experimentally observed pinwheels have all possible orientations represented once around the pinwheel center. If the orientation preference changes clockwise, we call it a pinwheel of positive sign. If the change is counter-clockwise, we call it a pinwheel of negative sign. Pinwheels where orientations are represented more than once are not experimentally observed. These singularities exist down to a cellular level. **Fig. 2.6C** shows an image obtained with two-photon microscopy and calcium imaging from cat V1. Each dot is a cell soma. The color corresponds to the preferred orientation. The surface of the visual cortex does not only show orientation preference. Neurons also have preferred spatial frequencies and ocular dominance. This is illustrated in **Fig. 2.6D**. It turns out that orientation preference maps (OPMs) exist in a variety of mammals as in different species of monkeys, cats, ferrets, sheep, tree shrews and humans [13, 25–27, 77, 96, 130, 165]. **Fig. 2.6E** shows an image of a rat’s visual cortex, imaged with the same technique as **Fig. 2.6C**. The neurons in this image have a preferred orientation, but no large scale order is visible! In fact, rats lack orientation maps [62, 129, 134]. The pattern observed on rat visual cortex is called a *salt-and-pepper* pattern. The same observation has been made with rabbits [121] and squirrels [167]. As a matter of fact, many rodents lack orientation maps and until today the reason is not clear.

Orientation preference maps of the galago, the tree shrew and the ferret are shown in **Fig. 2.7A**. The pinwheel density per cortex area as function of the *hypercolumn* size is shown in **Fig. 2.7B**. As a rule of thumb, the smaller the animal, the higher the number of pinwheels per mm^2 although this is not a necessity [98]. A hypercolumn is defined as a region of size Λ^2 . This is a natural choice because orientation preference maps are aperiodic with a typical scale, defined as Λ . Consequently, their power spectrum is isotropic with a characteristic frequency. This is shown for the power spectrum of a cat’s OPM in **Fig. 2.7C**. After normalization of the pinwheel density with this typical scale, it turns out that this density is the same for all four species considered here. This is shown in **Fig. 2.7D**. In fact, after normalization many universal properties show up. **Fig. 2.7E** shows the pinwheel distance distribution between nearest neighbors **(a)** and nearest neighbors of same and opposite sign **(b)**. Not only are the local statistics universal - also non-local statistics have similar properties. This is illustrated in **Fig. 2.7F**. **Fig. 2.7F (a)** shows the pinwheel density measured in circles of different radii. **Fig. 2.7F (b)** shows the standard deviation of this number for various circle radii. The powerlaw found is universal.

2. FUNDAMENTALS

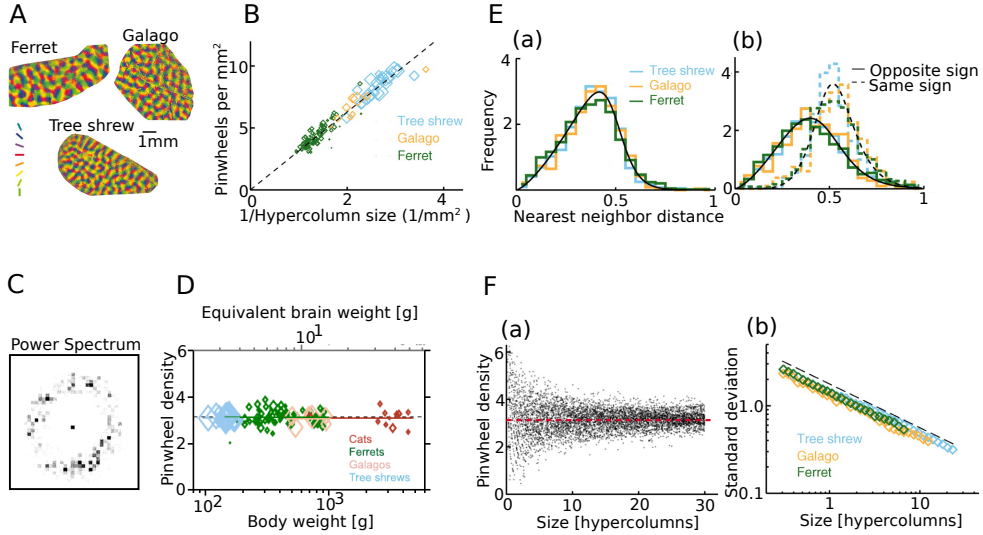


Figure 2.7: **A** Orientation preference maps in galago, tree shrew and ferret are similar [96]. **B** Shown is the number of pinwheels per surface area on the visual cortex [96]. **C** The power spectrum of an OPM is isotropic with typical frequency. This frequency sets a natural periodicity scale of the maps [127]. **D** Pinwheel density normalized with the typical scale of the maps. The line indicates 3.14, the average over different species [98]. It should be noted that there is substantial scatter among different individuals. **E** Normalized with the typical scale, OPMs have universal properties regarding **(a)** the pinwheel nearest neighbor distribution and **(b)** the pinwheel neighbor distribution of same and opposite sign [96]. **F** Similarly OPMs have common non-local properties. **(a)** Shown is the pinwheel density measured in circles of different radius. As the radius increases, the pinwheel density approaches 3.14. **(b)** The standard deviation of the curve in **(a)** is universal [96].

These observations show a remarkable universality of OPMs in different species; a universality of which the properties are difficult to create [96]. On the other side there are rodents with no obvious large scale structure as to orientation preference of cortical neurons. This dichotomy is not well understood.

2.4 STRUCTURE OF THIS THESIS

The next chapter discusses the idea that OPMs emerge from well structured retinal ganglion cell mosaics. This notion, which is built on ideas from the late 1980s received a lot of attention recently because it does not require intra-cortical interaction to form OPMs. In this chapter, we discuss the idea that hexagonal retinal ganglion cell mosaics create orientation preference maps by a Moiré-Interference effect, mapped into the cortex by retinotopy.

2.4. Structure of this Thesis

After analytically calculating a cortical cell's receptive field and its amplitude spectrum, we show how to extract preferred orientation and preferred spatial frequency, thereby improving a previous method. We compare the distribution of preferred spatial frequencies with experimental data and show that preferred spatial frequency is not determined by the distance between ON and OFF ganglion cells. Following the description of single cells' properties, we calculate the corresponding OPM. We describe the OPM, its amplitude spectrum and the pinwheel density analytically and quantitatively. We confirm our exact findings numerically and include a quantitative description of the effects of positional noise on a lattice-like RGC mosaic. In summary, this chapter presents a number of findings which challenge the Moiré-Interference model.

In the second chapter, we try to overcome the encountered challenges by modification of the original model. We present a new type of pairwise interacting point process which we use to reverse engineer ganglion cell mosaics from realistic OPMs. We obtain aperiodic mosaics which resemble those observed regarding the nearest neighbor distribution. These mosaics are not hexagonal, yet they create OPMs. In these model maps, we find a strong angular correlation of ON/OFF ganglion cell pairs. We compare the model prediction with X-cell mosaics of the cat. In published mosaics available to us, we cannot find a trace of angular correlation.

There are two major findings presented in this thesis. First, the spatial layout of OPMs generated from hexagonal ganglion cell mosaics in a linear feed-forward model does not have the same properties as the layout of experimentally observed maps. Second, ganglion cell mosaics do not have the necessary spatial statistics to generate OPMs. This leads to the conclusion that experience-dependent and self-organizing processes are essential for OPM formation.

HEXAGONAL RGC MOSAICS AND OPMS

‘From man or angel the great Architect did wisely to conceal, and not divulge his secrets to be scanned by them who ought rather admire; or if they list to try conjecture, he his fabric of the heavens left to their disputes, perhaps to move his laughter at their quaint opinions wide hereafter, when they come to model heaven calculate the stars, how they will wield the mighty frame, how build, unbuild, contrive to save appearances, how gird the sphere with centric and eccentric scribbled o’er, and epicycle, orb in orb.’

John Milton: “Paradise Lost” [118]

3. HEXAGONAL RGC MOSAICS AND OPMs

3.1 INTRODUCTION

The tangential organization regarding orientation preference of neurons of the primary visual cortex (V1) has originally been observed 50 years ago [80, 81]. More recently, optical imaging technologies revealed a map-like organization of orientation preference [12, 13, 66, 84, 165, 178] with topological defects (pin-wheels) embedded on a cellular level [130]. OPMs are aperiodic with a typical scale [116, 127] and show an intriguing structure across different species with remarkably universal properties [96, 98, 117]. This universality indicates an underlying engineering principle which is still unclear. OPMs have been modeled using different approaches [39, 47, 50, 51, 90, 93, 101, 104–106, 128, 139, 140, 152, 158, 159, 180] of which most rely on some sort of self-organization. However there is experimental evidence indicating that there are experience independent mechanisms which influence the formation of OPMs. Orientation selectivity in visual cortical neurons can be observed as soon as kittens open their eyes [81]. Organization into OPMs develops independently from visual input [24, 32, 33] and is remarkably static [25, 63]. This implies the influence of an external mechanism fed into the cortex as firstly noticed by Soodak [153, 154]. After silencing the cortex, visual cortical neurons remain orientation selective. The preferred orientation correlates with the orientation predicted by the thalamic afferents [26]. The same holds for the unsilenced cortex, yet the correlation is not as strong [87]. One can interpret these findings as afferents of which the connections' strength is determined by Hebbian learning to match a cortically self-organized map. Nevertheless, this reflects an interplay between afferents and a self-organized structure of the cortex. Note that this is not the only reported interplay between OPMs and features on the retina [1].

Retinal ganglion cells (RGCs), specific neurons in the retina collecting visual information [54, 110, 171] communicate this information to the brain. The ganglion cells' receptive fields (RFs) have a very distinct center-surround structure [49, 78, 145]. So called ON cells respond strongest to an illumination of a central spot surrounded by a dark annulus and for OFF cells vice versa. The RGC's axons form the optical nerve and contact neurons in the lateral geniculate nucleus (LGN). The associated thalamic receptive fields resemble retinal receptive fields [141]. Cortical neurons receiving thalamic input show orientation selectivity. This selectivity is associated with an asymmetric receptive field, usually an elongated structure with an ON and an OFF subregion [79, 80]. This feature distinguishes cortical cell receptive fields (RFs) from the receptive fields of ganglion cells in the retina and geniculate receptive fields in the LGN. An early approach to construct a V1 neuron's RF is by linear summation of thalamic receptive fields [79, 80]. V1 neurons have corresponding positions on the retina defined by retinotopic maps [38, 45, 163]. The combination of both ideas implies that orientation preference is influenced, if not determined by the RGC mosaic [26, 80, 153, 154]. Studies on the ganglion cell mosaic (for the cat e.g. [174]) allowed its simulation [48, 143, 186] and

3.1. Introduction

subsequently the calculation of orientation maps defined by retinal input [131, 132, 143, 144].

The Soodak-Ringach model [131, 132, 143, 144] building on previous ideas [79, 80, 153, 154] models OPMs as Moiré-Pattern of hexagonal ON and OFF RGC mosaics [4, 124]. Early studies showed how cortical receptive fields and orientation preference emerge by stochastic wiring of thalamic inputs [143]. Applying this idea to the entire cortex lead to the qualitative calculation of maps of orientation preference, anisotropy, spatial frequency and metabolic activity [144]. More recent publications by Paik et al. [131, 132] aim for quantitative results, making specific predictions. The first prediction is that OPMs have hexagonal symmetry. This hexagonal structure could be found in tree shrew, ferret and cat data [132], however, the techniques applied to analyze experimental data have recently been questioned [97]. The second prediction is a different angle representation and a specific distance-distribution between pinwheels of clockwise and counter-clockwise sense [131]. The non-uniform angle representation around pinwheels has been found in tree shrew maps. The distance-distributions reported are compared to the same tree shrew maps and found consistent, however, there is no comparison to the rich data set already available [96].

This chapter gives a systematic, quantitative and reproducible understanding of receptive fields and OPMs from an interference effect of hexagonal ON and OFF ganglion cell mosaics. We calculate cortical receptive fields exactly and show how they correspond to Gabor-Wavelets. The analytic expression for receptive fields allows to fit experimentally observed receptive fields and to estimate model parameters. We present a new approach in identifying a preferred stimulus, improving the previous method [144]. The effect of lattice noise on an OPM in the linear feed-forward model are far from understood. Neither is it clear if and how the interference model can reproduce the universal properties of OPMs found in different species [96, 98]. We address both question by calculating OPMs, their power spectra and the pinwheel-density analytically. We show that the pinwheel-density in OPMs resulting from the Moiré-Interference is $\rho = 2\sqrt{3} \approx 3.48$ and, hence, is too large to fit observations in different species. We express OPMs as phase of a complex field, written in terms of plane waves [158, 159]. For increasing noise on the ganglion cell mosaic, we show that the peaks of the Moiré-Modes are absorbed into a background with a Gaussian amplitude spectrum. We show that the hexagonal OPM predicted by the Soodak-Ringach is identical to the solution of a self-organization model, previously postulated to described joint pattern formation of ocular dominance and OPMs. To calculate pinwheel-distance distributions [131], one needs to estimate the typical scale of a map. We discuss the difficulties of applying the established wavelet-method [94, 95] of estimating the typical scale of a Soodak-Ringach OPM.

After a mathematical description of the Soodak-Ringach model, we firstly calculate receptive fields and their properties. Next, we calculate their power

3. HEXAGONAL RGC MOSAICS AND OPMs

spectra and show how to extract preferred stimuli. The exact result allows us to analyze previous methods [143, 144] and to improve them. We compare our findings regarding preferred spatial frequency with literature values [20] and find that the model predicts a distribution too narrow to fit this data. In the next section we turn our attention towards OPMs and their properties. We calculate OPMs and their power spectra for a noise free mosaic exactly. This noise-free OPM can be written as the phase of a complex field $z(\mathbf{x})$ composed of 6 plane waves. Next, we calculate OPMs created by noisy mosaics. We describe their spectra and show that it is very difficult to create aperiodic OPMs with a typical scale as experimentally observed [76, 116, 127]. Finally, we find that OPMs generated by the Soodak-Ringach model show a characteristic anisotropic angle representation. There is experimental evidence for an overrepresentation of orientation preference for cardinal angles [31] and further evidence for visual experience promoting an isotropic angle coverage [30]. However, there is no evidence for the type of orientation preference anisotropy that the Soodak-Ringach model predicts.

3.2 RESULTS

The Model and Receptive Fields

Fig. 3.1A illustrates the model described here. RGCs are monosynaptically connected to LGN cells. The LGN neurons mirror the ganglion cell mosaic and the ganglion cell's receptive fields. Neurons of primary visual cortex merge the receptive fields of several LGN neurons thus expressing receptive fields with an orientation preference. Different neurons across layer IV of the visual cortex sample from different LGN neurons. They have different receptive fields and thus different orientation preference. Specifically, sampling from a hexagonal mosaic of ON and OFF RGCs, as shown in **Fig. 3.1B**, creates a cortical receptive field (**Fig. 3.1C**) of which the preferred orientation changes periodically across the visual cortex (**Fig. 3.1D**). The left hand side of **Fig. 3.1D** shows the orientation preference of all cortical neurons, whereas the right hand side shows the low pass filtered orientation preference map. Receptive fields (**Fig. 3.1C**) and orientation maps (**Fig. 3.1D**) are calculated analytically. We now go step by step through this calculation.

The linear-non-linear model is a common method of calculating the response, i.e. firing rate of a cell, corresponding to a certain stimulus [53, 69]. It consists of two parts, firstly a linear filter acting on the stimulus and secondly, a static non-linearity. The linear filter applied by neurons of primary visual cortex is what we call the *receptive field* (RF). Subsequently the response S is calculated by taking the inner product of the receptive field exposed to a stimulus, in this case an illumination across the retina $L(\mathbf{x})$ so that $S = \int d^2\mathbf{x} RF(\mathbf{x}) L(\mathbf{x})$. Since S can become negative, it is filtered with the static non-linearity N , e.g. it is half-wave rectified [69] or filtered with a sigmoidal function to yield the

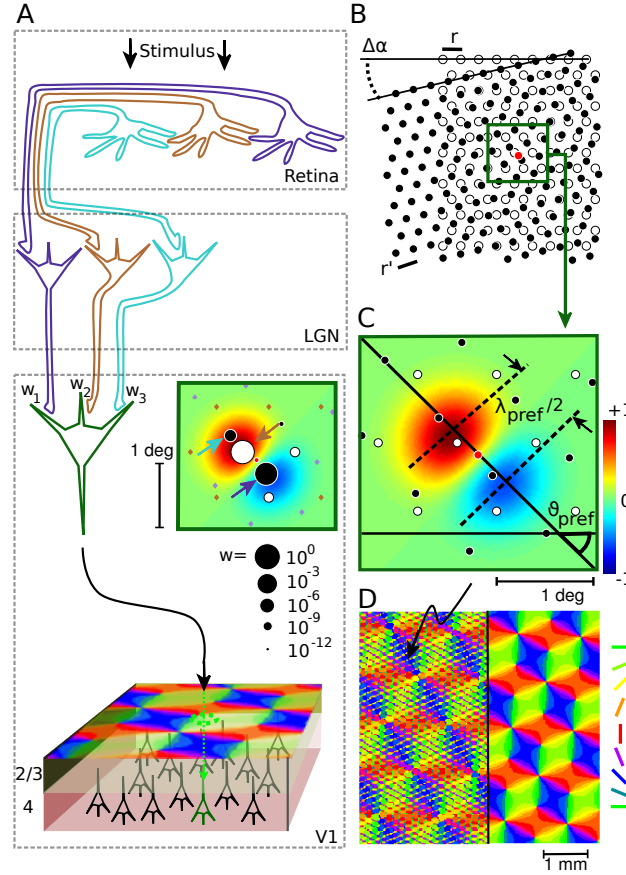


Figure 3.1: **A** Sketch of the early visual pathway as assumed in the model. Each LGN neuron receives input from only 1 RGC, and topography is maintained. A visual cortical neuron (green) receives input from several LGN cells with weights denoted as w_1, w_2, \dots . Different cortical neurons of layer IV (drawn in black) have different receptive fields, creating an OPM across the visual cortex indicated as color. The inset illustrates the synaptic weights for different LGN neurons connected to a V1 neuron encoded as size. Arrows show three important LGN/retinal inputs for this neuron, corresponding schematically to the three RGCs and thalamic neurons shown. Diamond-shaped RGC projections have synaptic weights $< 10^{-12}$ (see C). **B** Moiré-Interference between a hexagonal ON (white dots) and OFF (black dots) RGC lattice with relative orientation $\Delta\alpha$ and lattice constants r and r' respectively (black bars). The red dot in the center of the green square indicates the receptive field center of a cortical neuron. ↗

3. HEXAGONAL RGC MOSAICS AND OPMs

firing rate $\nu = N(S)$. We neglect the non-linearity assuming that it does not change orientation and spatial frequency preference [143, 144]. The common model for a ganglion cell’s receptive field is the difference of two Gaussians [49]. For simplicity and as originally proposed in [143], we model their receptive field (GRF) using a single Gaussian function of uniform width σ_r , localized at the ganglion cell’s receptive field center \mathbf{x}_j

$$\text{GRF}_j(\mathbf{x}) = \pm \exp\left(-\frac{(\mathbf{x}_j - \mathbf{x})^2}{2\sigma_r^2}\right). \quad (3.1)$$

A plus or minus sign in front of the ganglion cell’s receptive field, GRF, indicates an ON respectively OFF center cell. Adding several receptive fields with positive synaptic weights w_j

$$\text{RF}_{\mathbf{y}}(\mathbf{x}) = \sum_j w_j(\mathbf{y}) \text{GRF}_j(\mathbf{x}) \quad (3.2)$$

yields the cortical receptive field (RF) of a V1 neuron with receptive field center at \mathbf{y} sampling from several ganglion cells in a linear approximation [80]. This is indicated in **Fig. 3.1A**. The synaptic weights are chosen to be Gaussian with scale σ_s .

$$w_j(\mathbf{y}) = \exp\left(-\frac{(\mathbf{x}_j - \mathbf{y})^2}{2\sigma_s^2}\right)$$

where \mathbf{x}_j is the center of a retinal receptive field and \mathbf{y} is the center of the cortical receptive field. Thus, the synaptic weights decay rapidly over distance. This is indicated as inset in **Fig. 3.1A**. As a starting point, we assume that ON and OFF center cells are localized on a perfectly hexagonal grid \mathcal{L} , **Fig. 3.1B**,

Figure 3.1: **C** Receptive field of the V1 neuron with receptive field center shown in B and synaptic weights shown in the inset in A. Red hues indicate ON subregions and blue regions indicate OFF subregions. White and black dots mark ON and OFF cell positions. The receptive field corresponds to the green box in B and the inset in A. The center of the receptive field is indicated as a red dot. Dashed black lines show spacing and orientation of the preferred stimulus. The V1 neuron is most responsive to a grating with wavelength λ_{pref} . Solid black lines indicate the construction of the preferred angle ϑ_{pref} of the neuron. **D** The orientation preference of all V1 neurons encoded as color. V1 neurons are aligned on a squared lattice sampling from the retina as indicated in B and C. Right hand side: the low frequency contributions of the OPM (see text for details). The arrow indicates the position of a V1 neuron similar to the one in C.

3.2. Results

with different lattice constants r and r' ,

$$\mathcal{L} = \left(\begin{pmatrix} 1 \\ 0 \end{pmatrix} k + \frac{1}{2} \begin{pmatrix} 1 \\ \sqrt{3} \end{pmatrix} l \right) f \quad \forall k, l \in \mathbb{Z},$$

where $f = r, r'$ is the lattice constant. Later, we include Gaussian noise applied to each lattice point [132, 143], but for now we use the unperturbed lattice. Note that for σ_s on the order of the lattice spacing, each cortical cell samples from a very small number of ganglion cells. Thus, well tuned cortical cells have a receptive field dominated by a small number of ON- and OFF-RGC (see **Fig. 3.1C**).

Every hexagonal lattice can be written as sum $\mathcal{L} = \mathcal{L}_1 + \mathcal{L}_2$ of two rectangular lattices with orthogonal base vectors by separating even and odd numbers in l and shifting the l -sum so that the x-component is 0. Here, the two rectangular lattices are

$$\begin{aligned} \mathcal{L}_1 &= \left(\begin{pmatrix} 1 \\ 0 \end{pmatrix} k + \begin{pmatrix} 0 \\ \sqrt{3} \end{pmatrix} l \right) f & \forall k, l \in \mathbb{Z}, \\ \mathcal{L}_2 &= \left(\begin{pmatrix} 1 \\ 0 \end{pmatrix} k + \begin{pmatrix} 0 \\ \sqrt{3} \end{pmatrix} l + \frac{1}{2} \begin{pmatrix} 1 \\ \sqrt{3} \end{pmatrix} \right) f & \forall k, l \in \mathbb{Z}. \end{aligned}$$

We additionally rotate the lattice vectors of \mathcal{L} by

$$\Omega(\alpha) = \begin{pmatrix} \cos(\alpha) & -\sin(\alpha) \\ \sin(\alpha) & \cos(\alpha) \end{pmatrix}. \quad (3.3)$$

The ON mosaic is rotated with an angle α , the OFF lattice with an angle α' . The difference between the angles is $\Delta\alpha$ as shown in **Fig. 3.1B**. As a consequence of writing the hexagonal lattice as sum of independent rectangular lattices, the sum (Eqn. (3.2)) for the ON and for the OFF-sublattice factorizes into two independent sum which can be evaluated exactly. The result for a single sub-lattice (either ON or OFF) is

$$R_{\alpha,r,y}^{\text{ON/OFF}}(\mathbf{x}) = T(\Theta_3(\mathbf{b}\mathbf{e}_\phi, \tau)\Theta_3(\mathbf{b}\mathbf{e}_r, \xi) + \Theta_4(\mathbf{b}\mathbf{e}_\phi, \tau)\Theta_4(\mathbf{b}\mathbf{e}_r, \xi)) \quad (3.4)$$

where

$$\begin{aligned} \mathbf{b} &= \frac{\mathbf{x}\sigma_s^2 + \mathbf{y}\sigma_r^2}{\sigma_s^2 + \sigma_r^2} \\ \mathbf{e}_r &= -\frac{\pi}{r} \begin{pmatrix} \cos(\alpha) \\ \sin(\alpha) \end{pmatrix} \\ \mathbf{e}_\phi &= -\frac{\pi}{\sqrt{3}r} \begin{pmatrix} -\sin(\alpha) \\ \cos(\alpha) \end{pmatrix} \\ \tau &= e^{-\frac{2\pi^2\sigma_r^2\sigma_s^2}{3r^2(\sigma_r^2 + \sigma_s^2)}} \\ \xi &= e^{-\frac{2\pi^2\sigma_r^2\sigma_s^2}{r^2(\sigma_r^2 + \sigma_s^2)}} \\ T &= \frac{2\pi\sigma_r^2\sigma_s^2}{\sqrt{3}r^2(\sigma_r^2 + \sigma_s^2)} \exp\left(-\frac{(\mathbf{x} - \mathbf{y})^2}{2(\sigma_s^2 + \sigma_r^2)}\right) \end{aligned}$$

3. HEXAGONAL RGC MOSAICS AND OPMs

and Θ_3 and Θ_4 are the third and fourth Jacobi theta functions [176]. For details and the derivation of Eqn. (3.4), see Materials and Methods. ON/OFF indicates that this is the result for one sublattice of lattice constant r , oriented in an angle α , sampling from a receptive field center \mathbf{y} . The full receptive field is generated from the ON and OFF sublattice linearly superposed

$$RF_{\mathbf{y}}(\mathbf{x}) = R_{\alpha,r,\mathbf{y}}^{\text{ON}}(\mathbf{x}) - R_{\alpha',r',\mathbf{y}}^{\text{OFF}}(\mathbf{x}) \quad (3.5)$$

where α and r are the angle and the lattice of the ON lattice and α' and r' are the angle and the lattice constant of the OFF lattice. **Fig. 3.1C** shows a plot of Eqn. (3.5). The parameters used for this plot are given in the Materials and Methods section.

The receptive field calculated here resembles a typical simple cell receptive field with a size of about 1° [88, 111]. Eqn. (3.5) allows to fit experimentally observed receptive fields to estimate receptive field size σ_r , the scale of the synaptic connections σ_s and the properties of the lattice \mathcal{L} . In the following section, we extract the values of preferred angle ϑ_{pref} and preferred spatial frequency λ_{pref} as shown in **Fig. 3.1C** from the receptive field. This is the underpinnings of analyzing OPMs. As we have shown earlier, this calculation gives us an exact result for the linear operator. We assume for the following sections that the non-linearity does not influence preferred angle and spatial frequency; We comment on this issue in more detail below.

Tuning Curves and Power Spectra of Receptive Fields

The receptive field is a function in visual space so that $S = \int d^2\mathbf{x} RF(\mathbf{x}) L(\mathbf{x})$ is the response of a cell associated with an illumination pattern $L(\mathbf{x})$ onto the receptive field. The response for a wave-like illumination, ignoring the phase of the wave, can be calculated by using a plane wave $L(\mathbf{x}) = \exp(-i\mathbf{k}\mathbf{x})$ and subsequently taking the absolute value squared $|S|^2$. The absolute value squared is phase independent and solely a function of the properties of the wave-vector \mathbf{k} . Since this is the Fourier transform, we give the Fourier spectrum of the receptive field a new symbol,

$$\mathcal{R}_{\mathbf{y}}(\mathbf{k}) = \frac{1}{2\pi} \int d^2\mathbf{x} RF_{\mathbf{y}}(\mathbf{x}) e^{-i\mathbf{k}\mathbf{x}}. \quad (3.6)$$

We refer to the absolute value $|\mathcal{R}_{\mathbf{y}}(\mathbf{k})|$ as amplitude spectrum. This is the response to a grating with wave vector $\mathbf{k} = (k \cos(\vartheta), k \sin(\vartheta))$, where ϑ is the orientation and k is the spatial frequency. Ignoring the phase of the stimulus, a *tuning curve* for a specific spatial frequency k corresponds to the absolute value of the Fourier transform,

$$\text{TC}(\vartheta, k) = |\mathcal{R}_{\mathbf{y}}(k \cos(\vartheta), k \sin(\vartheta))|. \quad (3.7)$$

We can calculate the Fourier transform of Eqn. (3.5) by transforming Eqn. (3.1) and subsequently carrying out the sum for the two rectangular lattices \mathcal{L}_1 and

3.2. Results

\mathcal{L}_2 as above. Interchanging sum and integral is valid because the Gaussian sums are uniformly convergent. The result is

$$\mathcal{R}(\mathbf{k})_{\alpha,r,\mathbf{y}}^{\text{ON/OFF}} = U (\Theta_3(\mathbf{ce}_\phi, \nu) \Theta_3(\mathbf{ce}_r, \zeta) + \Theta_4(\mathbf{ce}_\phi, \nu) \Theta_4(\mathbf{ce}_r, \zeta)) \quad (3.8)$$

where

$$\begin{aligned} U &= \frac{2\pi\sigma_r^2\sigma_s^2}{\sqrt{3}r^2} \exp\left(-i\mathbf{ky} - \frac{1}{2}\mathbf{k}^2(\sigma_s^2 + \sigma_r^2)\right) \\ \mathbf{c} &= (\mathbf{y} - i\sigma_s^2\mathbf{k}) \\ \nu &= \exp\left(\frac{-2\pi^2\sigma_s^2}{3r^2}\right) \\ \zeta &= \exp\left(\frac{-2\pi^2\sigma_s^2}{r^2}\right). \end{aligned}$$

This result is valid for one sublattice of lattice constant r , oriented in an angle α . The Fourier spectrum of the full receptive field consists of the ON and OFF sublattice spectra linearly superposed

$$\mathcal{R}_{\mathbf{y}}(\mathbf{k}) = \mathcal{R}(\mathbf{k})_{\alpha,r,\mathbf{y}}^{\text{ON}} - \mathcal{R}(\mathbf{k})_{\alpha',r',\mathbf{y}}^{\text{OFF}}. \quad (3.9)$$

For details of the derivation of Eqn. (3.8) and a discussion of Eqns. (3.5) and (3.9) for different parameters σ_r and σ_s , see Materials and Methods.

Fig. 3.2A shows a normalized amplitude spectrum with parameters as in **Fig. 3.1C**. **Fig. 3.2B** shows the corresponding tuning curves for different spatial frequencies, normalized to their maximum values for comparison.

To extract the preferred spatial frequency $k_{\text{pref}} = 2\pi/\lambda_{\text{pref}}$ and the preferred angle ϑ_{pref} one can follow the proposal by [144] and calculate a complex number μ

$$\begin{aligned} \mu &= \frac{\int d^2\mathbf{k} |\mathcal{R}_{\mathbf{y}}(\mathbf{k})| \cdot e^{2i\arg(\mathbf{k})} |\mathbf{k}|}{\int d^2\mathbf{k} |\mathcal{R}_{\mathbf{y}}(\mathbf{k})|} = \\ &= \frac{\int_0^\infty dk \int_0^{2\pi} d\vartheta k^2 |\mathcal{R}_{\mathbf{y}}(k \cos(\vartheta), k \sin(\vartheta))| e^{2i\vartheta}}{\int_0^\infty dk \int_0^{2\pi} d\vartheta k |\mathcal{R}_{\mathbf{y}}(k \cos(\vartheta), k \sin(\vartheta))|} \end{aligned} \quad (3.10)$$

so that $k_{\text{pref}} = |\mu|$ and $\vartheta_{\text{pref}} = \arg(\mu)/2$. Next, we define a measure for a tuning curve's orientation selectivity, called *orientation selectivity index* (OSI). One such measure is the circular variance [20, 160, 182], generalized for a continuous tuning curve [144]

$$\text{OSI}(k) = \frac{\left| \int_0^{2\pi} d\vartheta \text{TC}(\vartheta, k) e^{2i\vartheta} \right|}{\int_0^{2\pi} d\vartheta \text{TC}(\vartheta, k)}, \quad (3.11)$$

where the tuning curves are defined by Eqn. (3.7). The preferred spatial frequency k_{pref} calculated by $k_{\text{pref}} = |\mu|$ gives the brown tuning curve in

3. HEXAGONAL RGC MOSAICS AND OPMs

Method	$k_{\text{pref}} [\text{mm}^{-1}]$	$k_{\text{pref}} [{}^\circ/\text{deg}]$	OSI
$ \mu $	4.8	1.1	0.15
$\text{argmax}_{\{k\}} (\mathcal{R}(\mathbf{k}))$	12.7	2.9	0.26
$\text{argmax}_{\{k\}} (\text{OSI}(k))$	17.8	4.1	0.27

Table 3.1: Comparison of k_{pref} obtained from the three methods for the receptive field shown in **Fig. 3.1C** and **Fig. 3.2A**. The corresponding OSI (Eqn. (3.11)) is also calculated.

Fig. 3.2C and an orientation selectivity indicated in **Fig. 3.2D** as brown line. The $|\mu|$ – method is derived from the measure of orientation selectivity (Eqn. 3.11) to estimate the position of the center-of-mass of the peaks of the receptive field: by doubling the phase of the vector \mathbf{k} , the function is wrapped around the origin (see **Figs. 3.3F** and **3.3G**). Calculating integral (3.10) gives the center-of-mass of the function shown in **Fig. 3.3G**. For reasons given below, we compare the performance of this method with two different methods. The first method is finding the maximum of the amplitude spectrum

$$k_{\text{pref}} = \text{argmax}_{\{k\}} (|\mathcal{R}(\mathbf{k})|).$$

The second method is optimizing the orientation selectivity

$$k_{\text{pref}} = \text{argmax}_{\{k\}} (\text{OSI}(k)).$$

The results for these three methods are shown in **Fig. 3.2A**, **3.2C** and **3.2D** as brown, yellow and purple curves. To compare the numerical values, all three results are given in **Tab. 3.1**. For the parameters used and details of the conversion from μm^{-1} to ${}^\circ/\text{deg}$, see Materials and Methods or the following chapter. We use the maximum method to find k_{pref} instead of the original proposal for the following reasons. First, experiments use the greatest response to identify the preferred spatial frequency [20, 86, 119]. Following the same method makes our results comparable to data (see **Fig. 3.2F**). Furthermore, it is a natural choice to use the maximum-response of a cortical neuron to quantify the optimal stimulus, analogously as it is done for the preferred angle. Second, the Soodak-Ringach method systematically underestimates the preferred spatial frequency (**Fig. 3.2C** and **Tab. 3.1**). Calculating k_{pref} with the new method yields better tuned cells. Third, a greater orientation-selectivity is equivalent to finding sharper tuning curves which follows the paradigm ‘sharper is better’ (e.g. [155] although this method is disputed[150]). Fourth, as opposed to the other methods monotonic non-linearities being applied to $|\mathcal{R}|$ to calculate a neurons firing rate do not change the position of the maximum. This is consistent with typical non-linearities like half-squaring and over-rectification [69]. Finally, the preferred spatial frequency from the maximum of the receptive field and the frequency for greatest orientation selectivity

3.2. Results

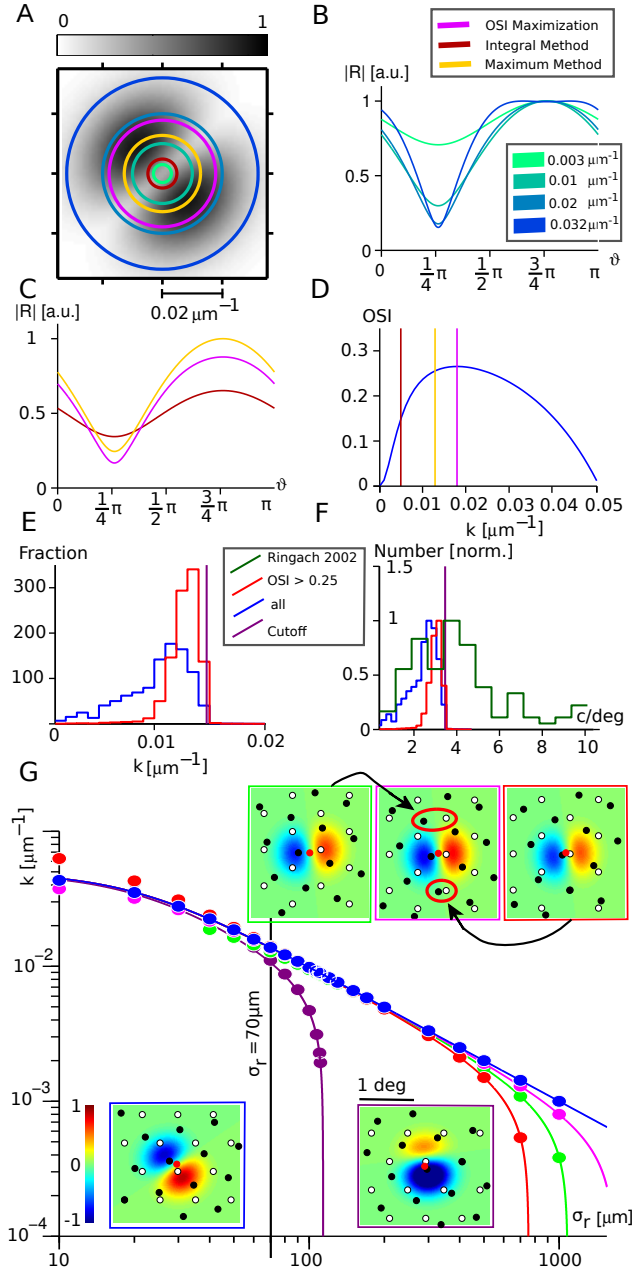


Figure 3.2: **A** Power spectrum of a V1 neuron's receptive field calculated with Eqn. (3.9). The absolute value $|\mathcal{R}|$ is shown as gray scale. The circles indicate different spatial frequencies as shown on the right. The yellow, the brown and the pink circle are defined by three different methods of calculating the preferred spatial frequency. ↗

3. HEXAGONAL RGC MOSAICS AND OPMs

give very similar results, however, finding the maximum of the receptive field is analytically and numerically easily feasible. Note that calculating ϑ_{pref} is very robust since the TC peaks are localized at the same position for different spatial frequencies (**Fig. 3.2B**). Thus, changing the definition of the preferred spatial frequency does not change the outcome of previous studies regarding the preferred angle ϑ_{pref} .

Using the maximum method, we continue to calculate ϑ_{pref} and k_{pref} . With Eqn. (3.9) we find for the absolute value squared of the receptive field

$$|\mathcal{R}(\mathbf{k})|^2 \propto \exp(-\mathbf{k}^2(\sigma_s^2 + \sigma_r^2)) \cdot \\ \cdot \left| \underbrace{\Theta_3^{\alpha,r} \Theta_3^{\alpha,r} + \Theta_4^{\alpha,r} \Theta_4^{\alpha,r} - \Theta_3^{\alpha',r'} \Theta_3^{\alpha',r'} - \Theta_4^{\alpha',r'} \Theta_4^{\alpha',r'}}_{G(\mathbf{k})} \right|^2$$

using the abbreviation $\Theta_i^{\alpha,r} \Theta_i^{\alpha,r} = \Theta_i(\mathbf{ce}_\phi(\alpha, r), \tau) \Theta_i(\mathbf{ce}_r(\alpha, r), \zeta)$. The $|\mathcal{R}(\mathbf{k})|^2$ function is composed of an anisotropic part (the elliptic functions) and a Gaussian envelope. To calculate ϑ_{pref} and k_{pref} , we expand the anisotropic part $|G(\mathbf{k})|^2$ to quadratic order

$$|\mathcal{R}(\mathbf{k})|^2 \approx \exp(-\mathbf{k}^2(\sigma_s^2 + \sigma_r^2)) \left(|G_0|^2 + \frac{1}{2} (k_1 \quad k_2) \mathcal{H}_0 \begin{pmatrix} k_1 \\ k_2 \end{pmatrix} \right) \quad (3.12)$$

Figure 3.2: **B** The (normalized) TCs corresponding to the circles in A. **C** The TCs corresponding to the brown, the yellow and the pink circle in arbitrary units. **D** Orientation selectivity calculated from Eqn. (3.11) and the amplitude spectrum in A as function of frequency. The brown, the yellow and the pink line correspond to the three preferred spatial frequency candidates in **Tab. 3.1**. **E** The distribution of preferred spatial frequencies (calculated with the maximum method). The greatest possible preferred spatial frequency (Eqn. (3.14)) is indicated by the purple line. The blue histogram shows data of all cortical cells, whereas the red one is filtered for cells with orientation selectivity greater 0.25. **F** Same figure as E shown in units of cycles/degree. This allows the comparison with experimental data [20] (shown in green). **G** Preferred spatial frequency for different V1 neurons as a function of the retinal receptive field size σ_r . The colors correspond to different positions on the retina from where the V1 neurons sample. The insets show receptive fields for $\sigma_r = 70 \mu\text{m}$. The three positions on top (red, pink and green) indicate a sequence with increasing ON/OFF RGC distance. All three positions are indicated by the arrows in the second inset. Black and white dots show OFF and ON RGCs. The colors indicate ON and OFF subregion. The purple curve illustrates a V1 neuron with a very asymmetric receptive field and the blue curve one with a very symmetric receptive field.

3.2. Results

where \mathcal{H}_0 is the Hessian at the origin and $G_0 = G(\mathbf{k} = 0)$. As a consequence of the $\mathbf{k} \rightarrow -\mathbf{k}$ symmetry of $|G(\mathbf{k})|$, there are no even terms in the Taylor expansion of $|G(\mathbf{k})|^2$. Note that this approximation is a very good one. The \mathbf{k} -dependent argument of the elliptic functions for biologically reasonable parameters is $\mathbf{ce} \approx |\mathbf{k}| \sigma_s^2 / r \approx 10^{-2}$ (see Eqn. (3.8)). For a numerical comparison of the full function $|\mathcal{R}(\mathbf{k})|^2$ and the approximation with an expanded anisotropic part, see Materials and Methods.

The Hessian

$$\mathcal{H}_0 = \begin{pmatrix} \frac{\partial^2 |G|^2}{\partial k_1^2} & \frac{\partial^2 |G|^2}{\partial k_1 \partial k_2} \\ \frac{\partial^2 |G|^2}{\partial k_2 \partial k_1} & \frac{\partial^2 |G|^2}{\partial k_2^2} \end{pmatrix} \equiv \begin{pmatrix} a & b \\ b & c \end{pmatrix}$$

is composed of derivatives of the elliptic functions. To calculate the preferred orientation, we use that

$$h(\theta) = (\cos(\theta) \quad \sin(\theta)) \mathcal{H}_0 \begin{pmatrix} \cos(\theta) \\ \sin(\theta) \end{pmatrix}$$

gives the second directional derivative in the direction of $(\cos(\theta), \sin(\theta))$. Carrying out this product gives

$$h(\theta) = a \cos(\theta)^2 + 2b \cos(\theta) \sin(\theta) + c \sin(\theta)^2.$$

The preferred angle can be found as the maximum of $h(\theta)$,

$$\vartheta_{\text{pref}} = \text{atan} \left(\frac{\sqrt{(a-c)^2 + 4b^2} - a + c}{2b} \right). \quad (3.13)$$

After identification of the preferred angle, we can calculate the second derivative in the direction of steepest curvature

$$\lambda = (\cos(\vartheta_{\text{pref}}) \quad \sin(\vartheta_{\text{pref}})) \mathcal{H}_0 \begin{pmatrix} \cos(\vartheta_{\text{pref}}) \\ \sin(\vartheta_{\text{pref}}) \end{pmatrix}$$

and calculate the maximum of the power spectrum in this direction

$$o(k) = \exp(-k^2(\sigma_s^2 + \sigma_r^2)) \left(|G_0|^2 + \frac{k^2}{2} \lambda \right),$$

which we find at

$$k_{\text{pref}} = \sqrt{\frac{1}{\sigma_s^2 + \sigma_r^2} - \frac{2|G_0|^2}{\lambda}} \leq \sqrt{\frac{1}{\sigma_s^2 + \sigma_r^2}}. \quad (3.14)$$

Since $\lambda > 0$ ($k = 0$ is a local minimum), Eqn. (3.14) gives a cut-off spatial frequency of $k_{\text{crit}} = \sqrt{\frac{1}{\sigma_s^2 + \sigma_r^2}}$. **Fig. 3.2E** and **Fig. 3.2F** show histograms of

3. HEXAGONAL RGC MOSAICS AND OPMs

the preferred spatial frequency k_{pref} calculated numerically for various RGC mosaics (see Materials and Methods). Taking only well tuned cells (applying the orientation selectivity cutoff at $\text{OSI} > 0.25$ reported in the literature [132, 144]) results in the red histogram, using all cortical cells yields the blue one. Both histograms are localized at smaller frequencies $k < k_{\text{crit}}$ than the cutoff as we expect. Reexpressing the spatial frequency measured in μm^{-1} in cycles per degree (see Materials and Methods) on the retina allows us to compare the results with experimental data [20] (green histogram in **Fig. 3.2F**). We find that the range of preferred spatial frequencies predicted by the model are substantially more narrow than the ones experimentally observed. This is consistent with the idea that retinal input delivers a blueprint upon which cortical signal processing is built. The correlation of highly orientation selective cells and high preferred spatial frequencies is what shifts the red histogram towards the cut-off (firstly observed numerically by [144]). The empirical values shown in green [20] have been measured at eccentricities between 1° and 6° . The cortical magnification in this region changes between 1 mmdeg and 5 mmdeg [38]. The receptive field center size is ≈ 0.04 deg and scatters between 0.01 deg and 0.08deg for P-cells [35]. The model might do better by incorporating the change in cortical magnification and RGC properties. This is, however, difficult to combine with the notion of a hexagonal and crystalline RGC mosaic because the cellular density changes substantially as well.

Now that we understand how to calculate preferred spatial frequency, we discuss the possibility of calculating maps of preferred spatial frequency. Eqn. (3.14) implies that the preferred spatial frequency is only determined by the parameter $\mathfrak{D} = 2|G_0|^2/\lambda$. This parameter can be understood as follows: the ratio between the DC component¹ of the amplitude spectrum and the curvature of the amplitude spectrum is largest for a cortical neuron with a single dominant domain (either ON or OFF) in its receptive field, because in this case the DC component is great whereas the curvature is small. For well-tuned cortical cells with a dipole receptive field, $G_0 = 0$, wherefore they have large preferred spatial frequencies. In this sense it is neither the lattice geometry nor the distance between ON and OFF RGCs, which determines the preferred spatial frequency but only the properties of the receptive field. These properties are determined by eccentricity [35] and thus, the preferred spatial frequency should decrease substantially for larger eccentricity. On the other hand, maps of preferred spatial frequency are isotropic across the cortex (despite local fluctuations) [85, 86] and thus eccentricity independent. The observation that the receptive field properties are essential for spatial frequency preference is quantified in **Fig. 3.2G**. The preferred spatial frequency of the red, pink and green receptive field is almost the same for a wide range of receptive field sizes σ_r , although the distance between the pair of cells is decreasing from

¹Direct current, the zero-frequency contribution of a signal, i.e. the amplitude spectrum component at the origin.

3.2. Results

left to right. The insets show the cortical cell receptive fields. The arrows indicate the position of the green and the red colored cortical cell's receptive field center. The purple curve shows the influence of asymmetry of the dipole (in this case the OFF cell is more dominant). As we expect, the preferred spatial frequency is systematically smaller. The preferred spatial frequency $k \rightarrow 0$, because for greater σ_r , the OFF subregion cancels the response of the ON cell and thus the cortical cell is only selective for $k = 0$. This happens if

$$\frac{1}{\sigma_s^2 + \sigma_r^2} = \lambda.$$

To give an example, this occurs at $\sigma_r = 113.7 \mu\text{m}$ for the purple curve (note that λ is not a function of σ_r). The colored dots in **Fig. 3.2G** are numerically calculated positions of the maximum of $|\mathcal{R}(\mathbf{k})|^2$. The drawn lines show Eqn. (3.14) with values of λ given in **Tab. 3.2**. For a comparison of the maximum of $|\mathcal{R}(\mathbf{k})|^2$ and Eqn. (3.14), the relative error between dots and curve at $\sigma_r = 70 \mu\text{m}$ is calculated and given in **Tab. 3.2**. This is also the value for the receptive field size σ_r for which the insets have been calculated. We chose this particular value because this is the one used throughout this thesis. Again, this comparison shows the validity of the approximation of the non-isotropic term. The sequence of receptive fields and their power spectra for different σ_r shown as blue dots are explicitly shown in Materials and Methods (see **Fig. 3.9**).

We conclude that spatial frequency preference depends only weakly on the distance between RGC cells, from which a V1 cell samples and is mainly determined by the parameters chosen. As a consequence, well tuned cells have a similar preferred spatial frequency whereas poorly tuned cells have a very small one. Selecting cells with a high orientation selectivity makes their preferred spatial frequencies uniform. The Soodak-Ringach model's prediction for preferred spatial frequency maps, after filtering for cells with great orientation selectivity, is thus that it should be very uniform, positively correlated with orientation selectivity and eccentricity dependent. This is in line with previous numerical simulations [144]. OSI-filtered receptive fields in the Soodak-Ringach model cover a range of factor ≈ 2 without the effects of eccentricity. Experimental observations, however, show that preferred spatial frequencies cover about one order of magnitude, independent of eccentricity [20, 85, 86]. Following this analysis of tuning curves and the properties of receptive fields, we continue to calculate orientation preference maps.

Orientation Preference Maps from noise-free RGC mosaics

In the previous calculation we have already obtained an equation (Eqn. (3.13)) to calculate an OPM. A plot of this equation is shown in **Fig. 3.3B**. The corresponding ON/OFF cell mosaic is shown in **Fig. 3.3A**. An intriguing structure is visible with domains of different orientation preference. A small

3. HEXAGONAL RGC MOSAICS AND OPMs

Color	$\lambda/10^{-6}\text{pm}^{-2}$	Error
purple	75.0	3.4%
red	1.75	2.5%
green	0.853	7.2%
magenta	0.361	1.2%
blue	0.000382	0.23%

Table 3.2: Values for the parameter λ for the 5 curves in **Fig. 3.2G**. Additionally, the relative difference between the dots (numerically calculated maxima of $|\mathcal{R}|^2$) and the drawn line (Eqn. (3.14)) for $\sigma_r = 70 \mu\text{m}$ is calculated.

section is magnified in the inset of **Fig. 3.3B**. The small subregions are not an effect of poorly tuned cells but rather a natural outcome of the Moiré-Interference process. **Fig. 3.3C**, **Fig. 3.3D** and **Fig. 3.3E** show cortical cell receptive fields associated with three points on the OPM. The receptive fields illustrate how rapidly orientation preference changes across the map. We calculate (see below) the slowly varying contributions to the OPM across the surface of the cortex: the slowly-varying (or low-frequency) contributions for the map in **Fig. 3.3B** are shown in **Fig. 3.3H**. The circular distance between both maps is shown in **Fig. 3.3J**. This is to illustrate that the small subregions show orthogonal orientation preference in respect to their vicinity.

The procedure of the Soodak-Ringach model is that after filtering cortical cells for those with high orientation selectivity, the orientation preference of the resulting group of cells is smoothed with a Gaussian to generate a continuous orientation preference map [144]. A Gaussian smoothing corresponds to a low-pass filtering of the amplitude spectrum. Thus, to calculate the smoothed OPM of the Soodak-Ringach model we need to identify the low-frequency contributions of the map shown in **Fig. 3.3B**.

Eqn. (3.9) can be rewritten as a sum by expanding the Jacobi theta functions [176] to

$$|\mathcal{R}_y(\mathbf{k})|^2 = \sum_i \left(C_i \exp\left(-\frac{1}{2\sigma^2}(\mathbf{k} - \mathbf{a}_i)^2\right) + C_i \exp\left(-\frac{1}{2\sigma^2}(\mathbf{k} + \mathbf{a}_i)^2\right) \right) \quad (3.15)$$

for some C_i and \mathbf{a}_i (for details see Materials and Methods). This sum is an infinite sum of pairs of Gaussians. The width of the Gaussians is $\sigma = \sqrt{2(\sigma_r^2 + \sigma_s^2)}^{-1}$ and independent of the index i . Every single pair of the sum corresponds to the amplitude spectrum of a Gabor patch with wave vector \mathbf{a}_i and width (in real space) $\tilde{\sigma} = \sqrt{2(\sigma_r^2 + \sigma_s^2)}$. Thus, Soodak-Ringach receptive fields can be written as infinite sums of Gabor patches. The preferred orientation of the infinite sum of Gabor patches is the direction where one can find the center of mass of the Gaussians. We apply this analogously to the calculation of preferred orientation with Eqn. (3.10). Note that this equation may not be a good choice of finding the preferred spatial frequency, however,

3.2. Results

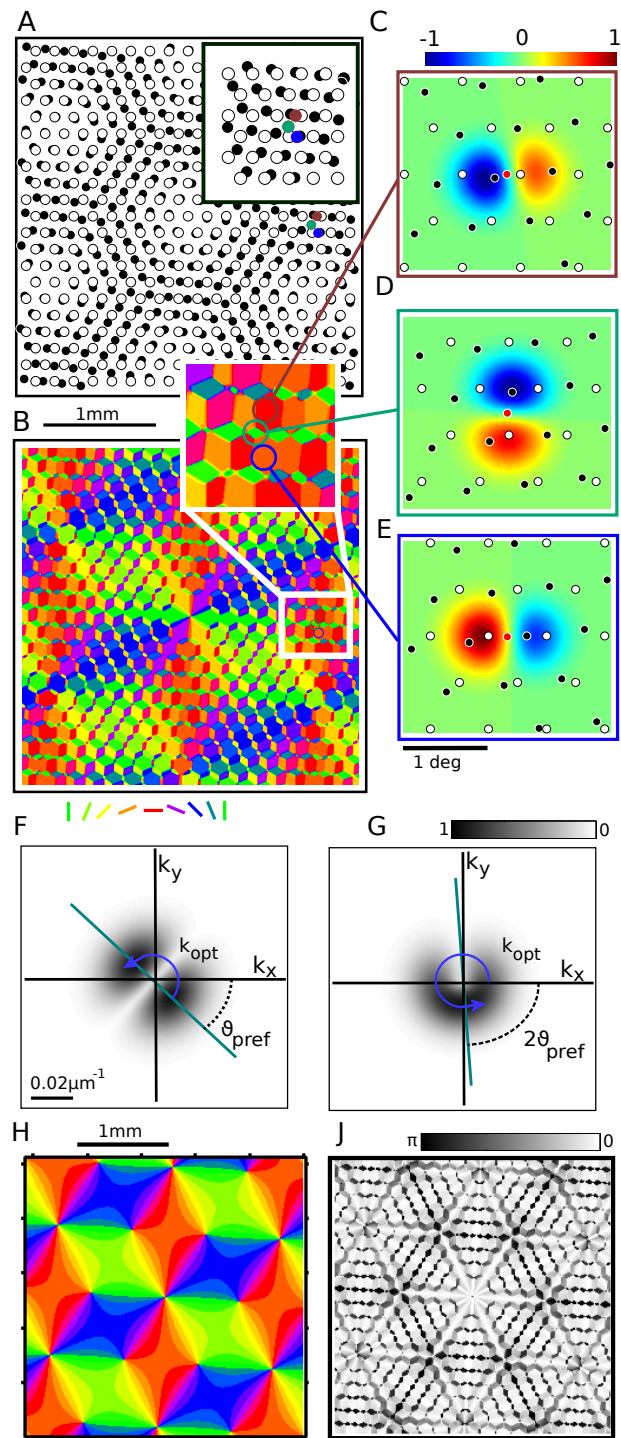


Figure 3.3: Receptive fields & OPMs. ↗

3. HEXAGONAL RGC MOSAICS AND OPMs

it works well for the almost frequency independent preferred angle. The amplitude spectrum of a single Gabor patch is a pair of Gaussians symmetrically arranged around the origin. Due to the π -symmetry, the two peaks are located at angles ϑ and $\pi + \vartheta$. Thus, to calculate the direction towards the center of mass of the peak, one can double the phase and calculate the center-of-mass of the resulting function. Therefore, by calculating the complex number

$$\mu = \sum_i C_i |\mathbf{a}_i| \exp(2i \arg(\mathbf{a}_i)) \quad (3.16)$$

we can find the preferred orientation as $\arg(\mu)/2$. Here $\arg(\mathbf{a})$ is the angle of the vector \mathbf{a} relative to the x-axis. This idea is illustrated in **Fig. 3.3F**, where a amplitude spectrum of a receptive field is shown. **Fig. 3.3G** shows the same amplitude spectrum after both peaks have been overlaid using the π -periodicity, i.e.

$$|\mathcal{R}_{\mathbf{y}}(k \cos(\phi), k \sin(\phi))| \rightarrow |\mathcal{R}_{\mathbf{y}}(k \cos(2\phi), k \sin(2\phi))|. \quad (3.17)$$

Again, this approach is technically the same as Eqn. (3.10). Calculating k_{pref} with this method yields too small results because the center-of-mass of the wrapped amplitude spectrum in **Fig. 3.3G** is substantially smaller than the peak of the function. However, the calculated preferred angle can be considered to be reliable.

The considerate reader might want to have a look at chapter Materials and Methods to confirm that Eqn. (3.16) is an expression for μ in terms of a

Figure 3.3: **A** A section of a ganglion cell mosaic. ON and OFF RGCs are shown as white and black dots. The inset shows a magnified region of the mosaic in which the center of three V1 neurons' receptive fields lie (brown, green and blue). **B** The OPM created from the mosaic in A. The inset is a magnified region of the OPM with three circles corresponding to the three neurons in A. **C-E** The RFs corresponding to neurons encoded in brown (**C**), green (**D**) and blue (**E**). Dots indicate ON and OFF RGCs, colored dots indicate the center of the receptive field. The coloring scheme shows ON and OFF subregions. **F** Power spectrum of a receptive field where the absolute value is encoded as gray scale. The preferred spatial frequency is indicated by the blue arrow, the preferred direction by ϑ_{pref} and the green line. **G** Same amplitude spectrum plotted with doubled phase. The maximum is now at $2\vartheta_{\text{pref}}$, indicated by the green line. The preferred spatial frequency is still on the circle indicated by the blue arrow. **H** The low-frequency contributions of the map shown in B. **J** Circular distance between the B and H shown as gray scale. Note the dark color of the small subdomains, indicating an orthogonal orientation preference of the subdomains in comparison to their vicinity.

3.2. Results

m	n	o	p	\mathbf{k}_i	$ \mathbf{k} $	Phase
1	1	1	1	$2((\mathbf{e}_r - \mathbf{e}'_r) + (\mathbf{e}_\phi - \mathbf{e}'_\phi))$	k_c	$-\frac{1}{2}(1 + i\sqrt{3})\varphi_0$
-1	-1	-1	-1	$-2((\mathbf{e}_r - \mathbf{e}'_r) + (\mathbf{e}_\phi - \mathbf{e}'_\phi))$	k_c	$-\frac{1}{2}(1 + i\sqrt{3})\varphi_0$
1	-1	1	-1	$2((\mathbf{e}_r - \mathbf{e}'_r) - (\mathbf{e}_\phi - \mathbf{e}'_\phi))$	k_c	$-\frac{1}{2}(1 - i\sqrt{3})\varphi_0$
-1	1	-1	1	$-2((\mathbf{e}_r - \mathbf{e}'_r) - (\mathbf{e}_\phi - \mathbf{e}'_\phi))$	k_c	$-\frac{1}{2}(1 - i\sqrt{3})\varphi_0$
0	2	0	2	$4(\mathbf{e}_\phi - \mathbf{e}'_\phi)$	k_c	φ_0
0	-2	0	-2	$-4(\mathbf{e}_\phi - \mathbf{e}'_\phi)$	k_c	φ_0
2	0	2	0	$4(\mathbf{e}_r - \mathbf{e}'_r)$	$\sqrt{3}k_c$	-
-2	0	-2	0	$-4(\mathbf{e}_r - \mathbf{e}'_r)$	$\sqrt{3}k_c$	-

Table 3.3: The low-frequency contributions of the OPM. The sum is evaluated over indices m, n, o, p . The vectors \mathbf{k}_i are the corresponding wave vectors and $|\mathbf{k}_i|$ their absolute values. Phase indicates the phase of the coefficients.

Fourier series in \mathbf{y} . The low frequency contributions of this Fourier series are contained in a sum, explicitly

$$\mu_{\text{lf}}(\mathbf{y}) = \sum_{m,n,o,p} f(m, n, o, p) \exp(2i\mathbf{y}(\mathbf{n}\mathbf{e}_\phi + \mathbf{m}\mathbf{e}_r - \mathbf{o}\mathbf{e}'_r - \mathbf{p}\mathbf{e}'_\phi)), \quad (3.18)$$

with coefficients $f(m, n, o, p)$ and four indices. The index lf in μ_{lf} indicates, that we neglect high frequency contributions. By calculating the first terms of Eqn. (3.18) we can find the low frequency contributions of the orientation map. After evaluating the sum we end up with the contributions shown in **Tab. 3.3**. The low frequency contribution to the OPM is composed of 6 modes with the same frequency

$$k_c = \frac{4\pi}{\sqrt{3}rr'} \sqrt{r^2 + r'^2 - 2rr' \cos(\alpha - \alpha')}, \quad (3.19)$$

and a fixed phase-relation. The common phase

$$\varphi_0 = \frac{e^{i(\alpha+\alpha')} (e^{i\alpha'}r + e^{i\alpha}r')}{e^{i\alpha}r + e^{i\alpha'}r'}$$

is associated with an overall rotation of the map. All 6 modes have the same amplitude. The next modes with smaller amplitude have the frequency $\sqrt{3}k_c$. Defining a complex field $z(\mathbf{y})$ composed of a sum of 6 plane waves with wave-vectors \mathbf{k}_i and the phase relation in **Tab. 3.3**

$$z(\mathbf{y}) = \sum_i \exp(i\mathbf{k}_i \cdot \mathbf{y}),$$

allows us to write the OPM created by the Soodak-Ringach model as the phase of this complex field

$$\vartheta_{\text{pref}}(\mathbf{y}) = \frac{1}{2} \arg(z(\mathbf{y})). \quad (3.20)$$

3. HEXAGONAL RGC MOSAICS AND OPMs

This specific pinwheel crystal, called a *Braitenberg Pinwheel Crystal* by Reichl et al. [19, 139, 140], can be created exclusively by means of self-organization. Braitenberg suggested (relying solely on electrode penetration data) to model OPMs as crystals with orientation preference being radially arranged around centers which are regularly arranged. Reichl et al. studied the interaction of ocular dominance and orientation preference in a self-organization model and found several different Braitenberg Crystals. The OPM predicted by the Soodak-Ringach model corresponds to a crystal discussed in their work [139]. The equation for the typical wavelength of the OPM (Eqn. (3.19)) can be transformed by introduction of a new parameter β and defining

$$r' \rightarrow (1 + \beta)r$$

so that the typical wavelength becomes

$$\Lambda_c \equiv \frac{2\pi}{k_c} = \frac{\sqrt{3}}{2} \cdot S \cdot r, \quad (3.21)$$

using the scaling-factor S which is the distance between two vertices of the Moiré-Pattern in units of r [4, 11, 124]

$$S = \frac{1 + \beta}{\sqrt{\beta^2 + 2(1 - \cos(\Delta\alpha))(1 + \beta)}}.$$

The explanation for the factor $\frac{\sqrt{3}}{2}$ is that $S \times r$ is the distance between two vertices of the Moiré-Interference pattern whereas the typical wavelength is associated with the peaks in reciprocal space. A derivation of this factor is given in the Materials and Methods section. It turns out that the typical scale is the distance between the straight edges of a hexagon unit cell. The difference between both is illustrated in **Fig. 3.4C** and **Fig. 3.4E**. Our results for the periodicity of the Moiré-Pattern and its orientation, following from an analysis of receptive fields, is identical to results derived from Fourier arguments [4] and geometrical arguments [124] for two superposed hexagonal lattices.

The identification of the pinwheel-crystal allows us to calculate the pinwheel density of the OPM analytically. There are $n = 4$ pinwheels per unit cells (shown in **Fig. 3.4C**): one, where each orientation is represented twice. This pinwheel is located in the center of the cell. Each of the six corners carries $1/3$ of a pinwheel where each orientation is represented once. The pinwheel density in this hexagon is $n = 4 \cdot \text{area}^{-1}$. The hexagonal unit cell has an area $A = \frac{3\sqrt{3}}{2} \left(\frac{S \times r}{2}\right)^2$ where $\frac{1}{2}S \times r$ is the side length/radius of the hexagon. To calculate the pinwheel density ρ , we have to rewrite the density to the number of pinwheels per characteristic scale Λ_c^2 . The characteristic scale is calculated in Eqn. (3.21). Therefore $\Lambda_c^2 = \frac{3}{4}(S \times r)^2$ and

$$\rho = n \cdot \frac{A}{\Lambda_c^2} = n \frac{\frac{3\sqrt{3}}{8}(S \times r)^2}{\frac{3}{4}(S \times r)^2} = n \frac{\sqrt{3}}{2} \approx 3.46.$$

3.2. Results

This is the same result found by Reichl et al. [139]. At this point we have shown how receptive fields correspond to Gabor patches, we have calculated the amplitude spectrum of an OPM, its typical frequency and the pinwheel-density.

To conclude this section we compare our findings to numerical simulations. This is done in **Fig. 3.4**. On the left hand side, **Fig. 3.4A** shows the full map of orientation preference calculated analytically. On the right hand side, it shows the orientation preference of all cortical cells calculated numerically (for details, see Materials and Methods). Eqn. (3.13) gives the same result as the simulation. **Fig. 3.4B** shows the amplitude spectrum of the full orientation map. Many high frequency contributions are visible. Below the two figures, we compare directly analytics and numerics. On the right hand side of the figure, we follow the Soodak-Ringach model numerically [132, 144]: cortical cells are filtered for $OSI > 0.25$ (**Fig. 3.4E** left) and subsequently smoothed (**Fig. 3.4E** right). The inset shows a magnified region of OSI-filtered neurons. The amplitude spectrum of this numerically calculated map is shown below (**Fig. 3.4F**). These findings are compared with the analytics on the left hand side of the figure. The low-frequency contributions as calculated above are shown in **Fig. 3.4C** and the corresponding amplitude spectrum from the 6 Moiré-Modes is shown in **Fig. 3.4D**. The cross-like shape of the peaks in **Fig. 3.4F** is a numeric artifact. Calculating the amplitude spectrum of **Fig. 3.4C** numerically, we find the same shape (shown in **Fig. 3.4D**). The amplitude spectrum of Eqn. (3.20) is composed of 6 delta-like peaks.

The faint peaks at greater frequencies in **Fig. 3.4F** are localized at $\sqrt{3}k_c$ as we have seen analytically in **Tab. 3.3**. However, their amplitude is substantially smaller due to the low-pass Gaussian smoothing. The very characteristic pinwheels of winding number 2 are not stable as experimentally observed and split into two pinwheels [132]. Although they are topologically stable (see the theory of planar spins [114]), structurally they are not. High strength phase singularities (where each orientation is represented multiple times) or dislocations in solutions of the wave equation unfold upon perturbation to phase singularities where each orientation is represented once [43].

OPMs from noisy hexagonal RGC mosaics

So far we have studied the idealized situation of noise-free RGC mosaics. After going through the analytic solution to the Soodak-Ringach model, we have checked that numerics and analytics are consistent. Following this test, we proceed to analyze the effect of Gaussian noise on the lattice because adding noise is a necessity to create realistic RGC mosaics and realistic OPMs [131, 132]. The effect of Gaussian noise of standard deviation $\sigma = \eta \cdot r$ being applied to the ganglion cell mosaic is studied in **Fig. 3.5**. The parameter r is the lattice constant and η is the noise level. **Fig. 3.5A** shows two OPMs calculated numerically with the Soodak-Ringach model for noisy mosaics. **Fig. 3.5B**

3. HEXAGONAL RGC MOSAICS AND OPMs

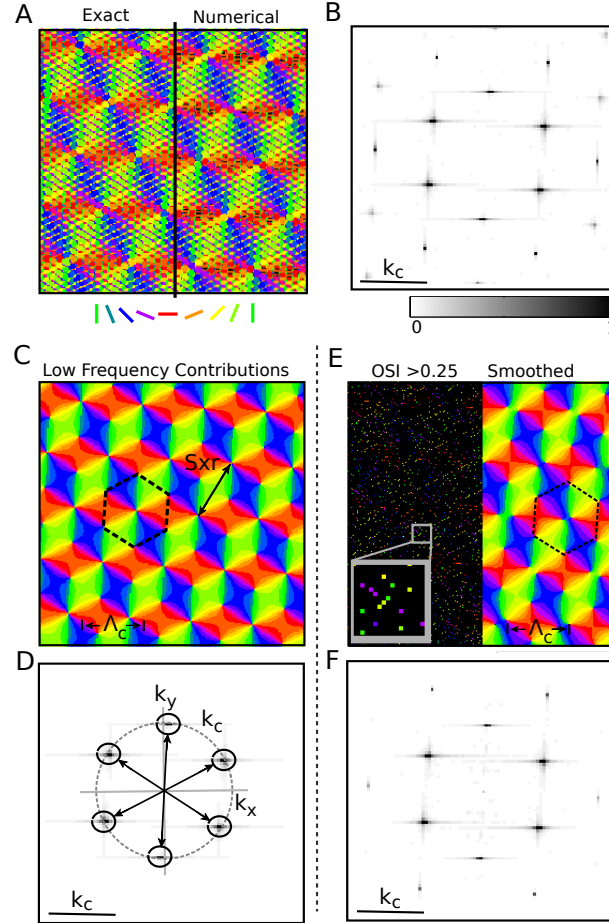


Figure 3.4: **A** The full OPM of the Soodak-Ringach model. The exact result (left) is almost identical to the numerics (right). **B** Power spectrum corresponding to the exact OPM in A. Note the high frequency contributions. Between **C-D** and **E-F**: the vertical dashed line separates numerics from analytics. **C** The low frequency contributions of the map in A calculated using Eqn. (3.20). Λ_c indicates the typical wavelength in the map. The dashed hexagon shows the unit cell used to calculate the pinwheel density. $S \times r$ is the distance between two double pinwheels/vertices of the Moiré-Pattern. ↗

3.2. Results

shows the full map (left) and the map filtered for cells with an $\text{OSI} > 0.25$ (right). What we find are regions around each dipole, similar to voronoi polygons, in which the orientation preference is dominated by this dipole. In addition, we find a substantial scatter of orientation preference. This is discussed in more detail below. **Fig. 3.5C** shows the spectra of the full OPM and the smoothed map. For a noise-level of $\eta = 0.12$ (**Fig. 3.5A** top), the map is still dominated by the Moiré-Modes. For a noise-level of $\eta = 0.5$ (**Fig. 3.5A** bottom), the amplitude spectrum (**Fig. 3.5C** bottom) does not show any indication of the Moiré-Modes. Both maps have been calculated with a physiologically reasonable scaling-factor of $S = 8.2$ [132]. For more details see Materials and Methods. To study the orientation maps, we calculate their marginal amplitude spectrum

$$f(k) = \int_0^{2\pi} d\vartheta |\mathcal{R}(k \cos(\vartheta), k \sin(\vartheta))|.$$

The result is shown in **Fig. 3.5D** and **3.5E**. The red and yellow lines indicate the analytic results for the two most prominent low-frequency contributions (see **Tab. 3.3**). To show that the analytic results hold for increasing noise, we show a magnification of the relevant part of the amplitude spectrum in **Fig. 3.5F** and **Fig. 3.5G**. The peak of the Moiré-Mode does not shift, only its amplitude is decreasing as noise is increasing. The difference between the unsmoothed and the smoothed map is the low-pass filtering with the Gaussian kernel. The white-noise amplitude spectrum of the OPM for large noise is transformed into an OPM with a Gaussian amplitude spectrum. The amplitude spectrum becomes white with increasing noise because the angular correlation between neighboring dipoles is lost: the position of an RGC's neighbor is random rather than defined by a Moiré-Effect.

Noise on a lattice can be understood as convolution of the noise-free lattice points with the noise probability distribution. Therefore we expect the expected value of an OPM amplitude spectrum from noisy mosaics to be the same as the noise-free ones multiplied with the amplitude spectrum of the

Figure 3.4: **D** The amplitude spectrum of the low frequency contributions in C where power is encoded as gray scale. The gray dashed circle is the critical circle at $k_c = 2\pi/\Lambda_c$. The black arrows indicate the theoretical position of the six peaks. This amplitude spectrum is calculated numerically to show that the cross-like shape of the points is a numeric artifact. **E** The entire OPM is filtered for cells with $\text{OSI} > 0.25$ (left) and subsequently smoothed (right). The inset shows a magnified region of the OSI-filtered OPM. The hexagon shows a similar unit cell to the one in C. **F** The amplitude spectrum of the numerically calculated map, shown in E (right).

3. HEXAGONAL RGC MOSAICS AND OPMs

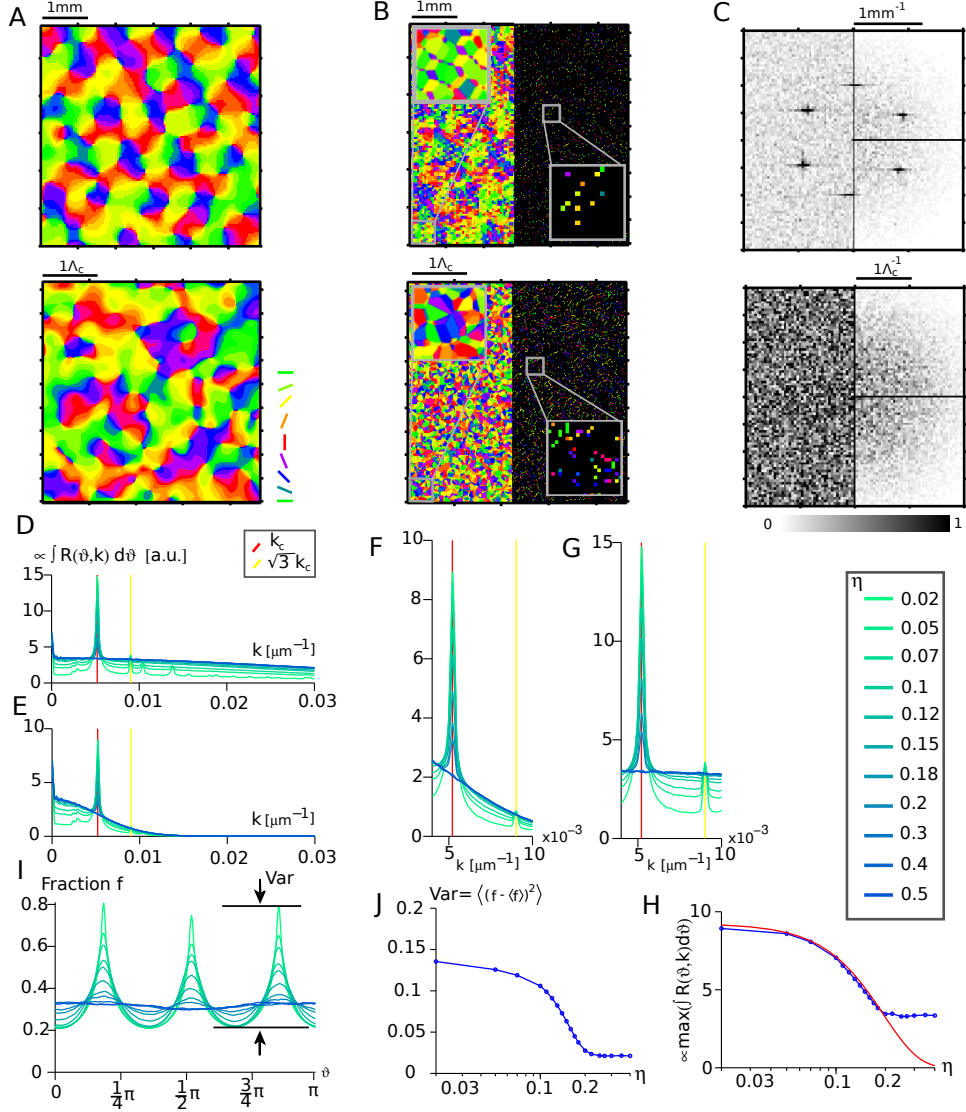


Figure 3.5: **A** Numerically calculated OPMs with noise $\eta = 0.12$ (top) and $\eta = 0.5$ (bottom). **B** The full OPM (left) and the OSI > 0.25 filtered map (right) which generate the plots in A for noise $\eta = 0.12$ and $\eta = 0.5$. Insets show magnified regions. **C** The power spectra of the maps in A and B. Shown is, left, the amplitude spectrum of the full map (B left) and right, the amplitude spectrum of the processed map (A). ↗

3.2. Results

noise probability distribution. This is the reason why there are no peaks at $\sqrt{3}k_c$ visible for $\eta = 0.12$ in the spectra in **Fig. 3.5A**. Consequently, we can quantify how the Moiré-Modes vanish with noise: the vertices of the Moiré-Pattern experience noise of $\sigma_M \approx S \times \eta \times r$, where S is the distance between two vertices of the Moire-Pattern in units of the lattice constant, η is the noise in units of the lattice constant and r is the lattice constant. For a derivation of this estimation, see Materials and Methods. Therefore peaks in the amplitude spectrum at position k_c decrease in height as

$$h(\eta) = \alpha \exp\left(-\frac{1}{2}k_c^2\sigma_M(\eta)^2\right) \quad (3.22)$$

which is the Fourier transform of the probability distribution of Gaussian noise, α is a fit-parameter and k_c is the position of the Moiré-Peak. This equation is plotted in **Fig. 3.5H** together with the peak heights from **Fig. 3.5E**. We see that the peak diminishes in amplitude as predicted by Eqn. (3.22) until at some point it is absorbed in the underlying Gaussian amplitude spectrum. The observation that the Moiré-Peaks decrease in height the same time as an exponential background increases, challenges the established method of estimating the typical wavelength in OPMs as we discuss below.

A different property of Soodak-Ringach OPMs is the non-uniform representation of angles. Binning of the cortical cells' preferred angle yields the histogram in **Fig. 3.5I**. There are 3 distinct peaks visible with a distance of 60° in between. The absolute position of the peaks, however, is not fixed. Rotating the entire OPM shifts this histogram circularly. The non-uniform angle representation can be quantified by calculating the squared deviation from a uniform distribution. This is done in **Fig. 3.5H**. The phenomenon is visible for a wide range of η and common for many types of pinwheel crystals [139, 140].

Following this analysis of the properties of OPMs generated by noisy mosaics, we continue to study the efficiency of the standard method in estimating the typical wavelength of the OPM. In **Fig. 3.6A**, we show an OPM generated with noise of $\eta = 0.12$ for a scaling factor of $S = 8.2$ with obvious hexagonal

Figure 3.5: **D** The marginal power spectra of full OPMs (B left) for different noise levels as function of k . Noise is indicated as color, corresponding to the colorbar bottom-right. The red line shows the exact k_c , the yellow line $\sqrt{3}k_c$. **E** The same as D for the processed map (A). **F** A magnified view of E. **G** A magnified view of D. **H** The height of the peak at k_c in E as function of noise. The blue dots are measured from D, the red curve is Eqn. (3.22). **I** Fraction of neurons selective for ϑ . Var indicates the deviation from uniformity. **J** The mean of the squared deviation from uniformity as function of noise.

3. HEXAGONAL RGC MOSAICS AND OPMs

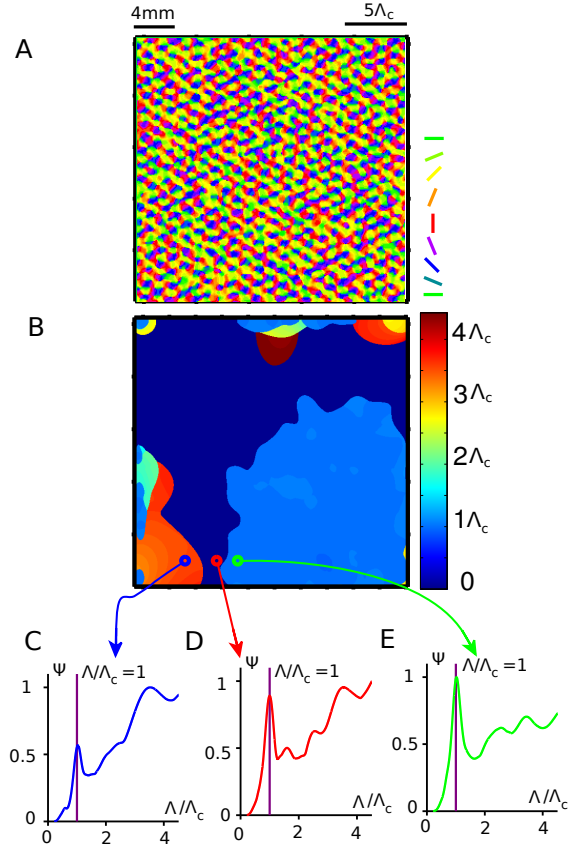


Figure 3.6: **A** An OPM calculated for $\eta = 0.12$. **B** The result of a wavelet-analysis to find the local wavelength $\Lambda_{\text{local}}(\mathbf{y})$ of the OPM in A. Colors encode the wavelength in units of $\Lambda_c = 2\pi/k_c$. See text for details. **C-E** The wavelet coefficients Ψ of a the wavelet estimation, Eqn. (3.24) at the blue (C), red (D) and green (E) position as function of the wavelet's periodicity Λ measured in units of Λ_c . The purple line shows the position of the Moiré-Peak.

3.2. Results

structure. The local scale estimation using a wavelet-analysis is described in the Materials and Methods section and in detail elsewhere [94, 95]. The typical scale $\Lambda_{\text{local}}(\mathbf{y})$ as function of the coordinate \mathbf{y} on the OPM found by the wavelet-analysis (**Fig. 3.6B**) has major regions where it identifies Λ_c correctly (green dot in **Fig. 3.6B**), but also a region where it fails to deliver a correct value. It finds values too high (blue dot in **Fig. 3.6B**) and regions where the wavelength is so close to the upper edge of a reasonable choice of wavelengths, that we neglect the result (red dot in **Fig. 3.6B**). This is a property of the wavelet analysis. If the maximum wavelet coefficient is obtained at the edge of the reasonable region, as in **Fig. 3.6D**, the wavelength is set to zero.

To estimate the typical scale, we calculate the wavelet coefficients Ψ for complex Morlet wavelets with periodicity Λ . The wavelet coefficients are shown in **Fig. 3.6C**, **Fig. 3.6D** and **Fig. 3.6E** as function of Λ , measured in units of Λ_c . The scale is determined by that value Λ which has the greatest wavelet coefficient. The typical wavelength $\Lambda_{\text{local}}(\mathbf{y})$ for the OPM jumps between the low-frequency contribution of the exponential background (the structure at large Λ) and the Moiré-Mode, which is clearly visible in all three figures. The position of the Moiré-Mode is indicated by the purple line at $\Lambda/\Lambda_c = 1$. We find that using a wavelet-estimation, either the Moiré-Mode is identified or the estimated typical scale is very large. For details of this analysis, see Materials and Methods.

After estimating the typical wavelength with the wavelet analysis, we can analyze model OPMs following the procedure for the analysis of experimentally observed maps [96]. The results for Soodak-Ringach maps are shown in **Fig. 3.7**. **Fig. 3.7A** shows the nearest neighbor distance distribution of pinwheels independent of topological charge. The axes show the distance between nearest neighbors and the noise level. Color encodes the (normalized) fraction of pinwheels at this distance. The plots in **Fig. 3.7B-C** show the distance distribution for pinwheels with equal and opposite topological charge. For the noise free case, the distance between pinwheels of both equal and opposite charge is $1/\sqrt{3}$ which can be derived from the hexagonal unit cell, shown in **Fig. 3.4C**. This value is indicated as white line. The horizontal lines shown $\eta = 0.12$, the value claimed to created OPMs with realistic spatial statistics. The three pinwheel distance distributions for $\eta = 0.12$ are shown in **Fig. 3.7D**. **(a)** shows the charge independent distance distribution and **(b)** the distribution for equal and opposite sign. The drawn lines show the experimentally observed distributions (see **Fig. 2.7**). **Fig. 3.7E (a)** shows the typical scale estimated using the wavelet analysis in comparison to the exact wavelength Λ_0 from the Moiré-Effect. The red dots show the values which saturate due to the limited maximum wavelength the numerical tool can detect. The blue dots are reliable. This figure shows that, as expected, the wavelength increases substantially with increasing noise. Accordingly the pinwheel density increases. This is shown in **Fig. 3.7E (b)**. The increasing wavelength is the reason that the mean pinwheel distances, shown in **A-C**,

3. HEXAGONAL RGC MOSAICS AND OPMs

approaches zero. **Fig. 3.7F (a)** shows the pinwheel density calculated for circles of increasing area measured in units of hypercolumns. The green line is our exact result, the red line shows π , which corresponds to the experimentally observed value. This curve has been calculated for $\eta = 0.02$ for which the typical wavelength can be estimated reliably. **Fig. 3.7F (b)** shows the standard deviation of the data shown in (a) for three different noise levels. The data for $\eta = 0.02$ shows the typical oscillations and the scaling for a pinwheel crystal [96]. For increasing noise, the exponent changes towards the exponent for a 2D Poisson process, however, the large typical scale Λ associated with high noise levels makes these curves not very reliable. It is worth noting that first, for weak noise the pinwheel distance distributions, **Fig. 3.7A** and **Fig. 3.7B**, are bimodal. The reason are the structurally unstable double pinwheels [43] which decay into two neighboring pinwheels of equal charge. Accordingly, the distance distribution for pinwheels of opposite sign, **Fig. 3.7C**, is not bimodal. Second, the pinwheel density is stable $\rho = 2\sqrt{3}$ as long as the wavelength is identified correctly. This is the case for $\eta \leq 0.14$, including the noise level with best fit to the RGC data around $\eta = 0.12$. For larger noise levels, the pinwheel density diverges because the typical scale Λ_c diverges.

3.3 DISCUSSION AND CONCLUSION

We have analyzed the Soodak-Ringach model from an analytic perspective. We found exact expressions for receptive fields and their power spectra. These results might be used to fit experimental data to measure the parameters of the model. After calculating receptive fields and their power spectra exactly, we described a method to extract optimal stimuli, which in this case refers to preferred angle and preferred spatial frequency. Instead of the previous method [143, 144] we use the maximum of the amplitude spectrum. Following this approach, we can compare the results with experimental data from *M. fascicularis* [20]. We found that the preferred spatial frequencies in the model cover a region too narrow compared to the data. This is not a surprising finding, considering experimental evidence that there are ≈ 10 ON and ≈ 12 OFF cells connected to a single cortical neuron which allows a wide range of possible preferred spatial frequencies [87]. The average preferred spatial frequency [20] of $3.7\text{cyc}/\text{deg}$ is very close to the cutoff which we observe. This indicates that the size of the ganglion cell's receptive field is smaller than estimated [132]. Furthermore, we have shown that the preferred spatial frequency is basically independent of the lattice. It is constrained by the choice of the receptive field size, the scale of synaptic connections and the shape of the receptive field, however, the distance between RGCs plays only a minor role. Especially after filtering cells with high orientation selectivity, it is difficult to explain the wide range of preferred spatial frequencies observed [85, 86]. Both, experimental findings and this study challenge the dipole approximation of only two RGC to be prominent enough to dominate the structure of a

3.3. Discussion and Conclusion

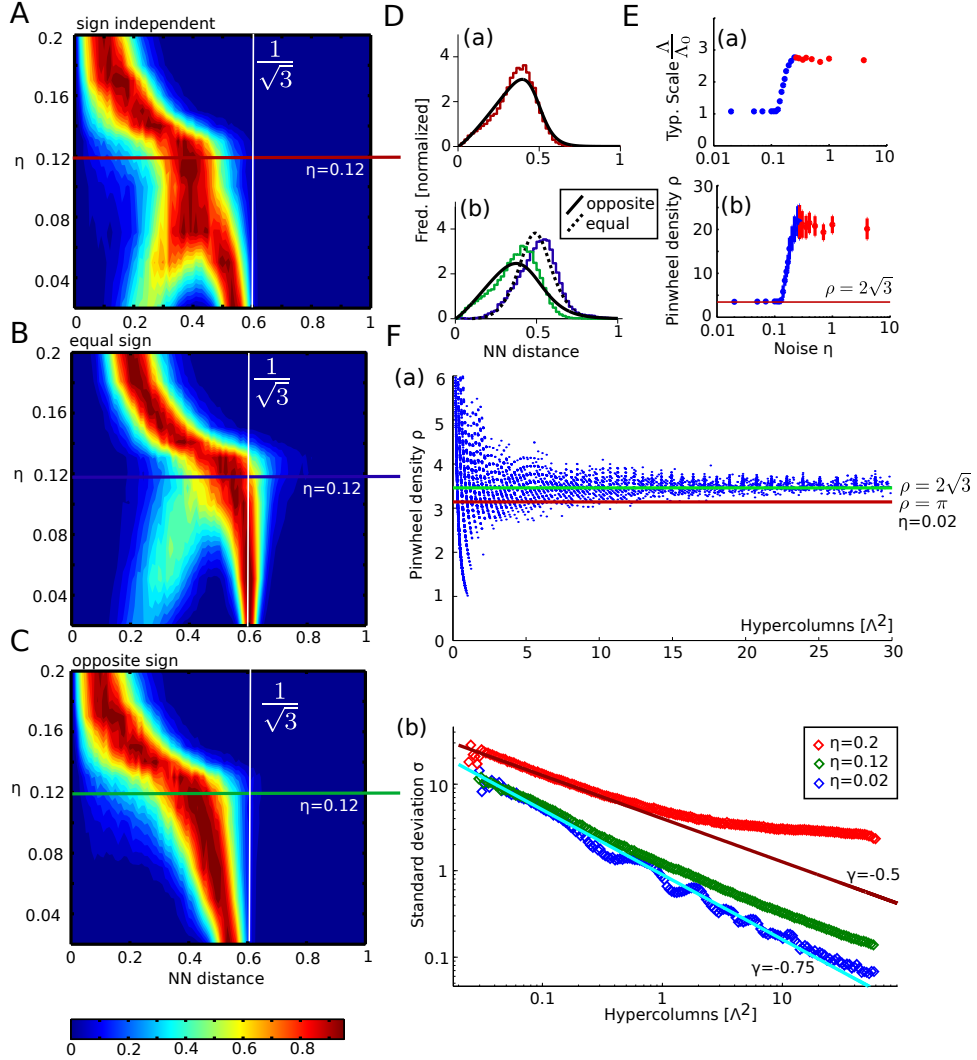


Figure 3.7: A statistical analysis using the wavelet tool for wavelength estimation of model maps. **A** Pinwheel distance distribution independent of topological charge. **B** Pinwheel distance distribution for pinwheels of equal charge. **C** Pinwheel distance distributions for pinwheels of opposite charge. **D** Pinwheel distance distributions for $\eta = 0.12$. The drawn lines show empirically observed curves [96]. **E (a)** The typical scale compared to the Moiré-Scale Λ_0 as function of noise. **E (b)** The pinwheel density as function of noise. Error bars show the standard deviation of 100 independent maps. Red dots show regions for which the wavelet tool is not reliable. **F (a)** Pinwheel density in circles of increasing radius for $\eta = 0.02$. **F (b)** The standard deviation of curves as in (a) for different noise levels.

3. HEXAGONAL RGC MOSAICS AND OPMs

cortical cell’s receptive field [132].

Next, we calculated OPMs and their power spectra for a noise free mosaic. We found a complicated microarchitecture of subdomains with substantial orientation scatter as compared to their vicinity. These subdomains consist of well-tuned cells (something which is actually visible in previous studies [132]). However these subdomains have neither been found in penetration experiments [73, 80], nor in high resolution optical imaging experiments [130]. The absence of these features makes intra-cortical interaction a necessity.

We showed that after smoothing of the OPM, thereby removing the high frequency contributions (and the subdomains), the resulting Soodak-Ringach OPM can be written as the phase of a complex field $z(\mathbf{x})$ composed of 6 plane waves. The same OPM is also created by self-organization models using an interplay between ocular dominance and orientation preference [139, 140] so that hexagonal structure in an OPM [132] is not clear evidence for a Moiré-Interference effect. The model OPM’s pinwheel density of $\rho = 3.48$ is too high and the pinwheel distance statistics are inconsistent with experimental data [96, 98, 117]. Next, we found that noise on the lattice does not transform the peaks of the Moiré-Modes into a ring. Noise decreases the amplitude of the Moiré-Peaks, in this sense interpolating smoothly between the pinwheel-crystal and an OPM with a Gaussian amplitude spectrum. Observed power spectra of OPMs, however, are isotropic with a typical frequency [116, 127]. We also found that the OPMs predicted by the Soodak-Ringach model do not have uniform angle representation. This non-uniformity is very strong, however experimentally, there is no evidence for it [30, 31].

Can these problems be overcome by an interference effect of a different RGC mosaic? The most realistic alternative is a mosaic generated with a pairwise interacting point process (PIPP) [48]. The amplitude spectrum of an OPM generated from a PIPP mosaic is white due to the intrinsic absence of angular correlations between ON and OFF center cells. After smoothing, the amplitude spectrum corresponds to the smoothing function and thus maps from PIPP-mosaics processed with the Soodak-Ringach method give OPMs with a Gaussian amplitude spectrum [76, 144]. Thus, these mosaics alone are not able to reproduce the features of OPMs observed experimentally. Therefore, in chapter 4, we propose a new type of PIPP to generate aperiodic mosaics which create OPMs. This method might overcome the severe problems discovered here.

3.4 MATERIALS AND METHODS

Figure details

All evaluations of the elliptic functions have been done with Wolfram Mathematica 8.0.1 on a 64 bit Linux. Numerical simulations have been carried out with a C++ program. Details for both are given below. The plots for the different figures have been calculated as follows:

Figure 3.1: The ganglion cell mosaic, **Fig. 3.1B**, and the receptive field in **Fig. 3.1C** has been calculated with the following parameters: $r = 170 \mu\text{m}$ and $\alpha = 0^\circ$ for ON and $r' = 170 \mu\text{m}$ and $\alpha' = 13^\circ$ for the OFF cell mosaic. The angle between both lattices is arbitrary and just for illustration, the lattice constant is chosen to be physiologically reasonable [132, 144]. The size of the receptive field is chosen to be $\sigma_r = 70 \mu\text{m}$ and the width of synaptic connection $\sigma_s = 20 \mu\text{m}$. Both are physiologically reasonable [132]. There is no offset between both lattices. The center of the cortical cell receptive field is at $\mathbf{y} = (300 \mu\text{m}, 121 \mu\text{m})$. Shown is Eqn. (3.5). To express the receptive field in units of degree visual angle instead of μm on the retina we convert the units using the geometrically determined ratio of $4.9^\circ/\text{mm}$ at 40° eccentricity in the human retina as an approximation for the Macaque eye [37]. (The value $4.4^\circ/\text{mm}$ for the cat's eye is very similar [7, 10], allowing the same type of analysis for [143, 144]). The inset in **Fig. 3.1A** is the same receptive field as **Fig. 3.1C**, however, the RGC size is determined by the logarithm of the synaptic weight. The OPMs in **Fig. 3.1D** have been calculated with the same parameters as **Figs. 3.1C** and **3.1D**, using Eqn. (3.13) and (3.20) respectively.

Figure 3.2: The amplitude spectrum (**A**) and the tuning curves (**B-D**) are calculated for the same parameters as **Fig. 3.1C**. The OSI (**D**) is calculated numerically with Mathematica from Eqn. (3.8) using the amplitude spectrum shown in **A**. The histograms in **E** are calculated numerically with values similar to **Fig. 3.1**: since this histogram is compared to data, we decreased the twist between both RGC mosaics to 7° . This generates a scaling factor of $S = 8.2$ which is in the middle of the physiologically observed range [132]. To calculate the histograms numerically, we implemented the full Soodak-Ringach model for noisy lattices in C++ using the GNU scientific library. The Code has been compiled with GCC version 4.3.4 on Linux 2.6.32. The simulations have been carried out on two cluster computers *Skadi* and *Frigg*. Frigg is equipped with Intel(R) Xeon(R) X5355 CPUs at 2.66GHz, using 32GB RAM. Skadi is using Intel(R) Xeon(R) E5440 CPUs at 2.83GHz, running with 32GB RAM, too. The conversion to degree visual angle was done with the ratio of $4.26^\circ/\text{mm}$ since the experimental values [20] have been measured at $1^\circ - 6^\circ$ eccentricity in the macaque eye, corresponding to an eccentricity of 0.68 mm. The dots in **G** show the maxima of $|\mathcal{R}|^2$, calculated from Eqn. (3.9) with Mathematica. The parameters for

3. HEXAGONAL RGC MOSAICS AND OPMs

the receptive fields are the same as for **Fig. 3.1**. The centers of the receptive fields are located at $\mathbf{y} = (420 \text{ } \mu\text{m}, 420 \text{ } \mu\text{m})$ (red), $\mathbf{y} = (250 \text{ } \mu\text{m}, 401 \text{ } \mu\text{m})$ (magenta), $\mathbf{y} = (100 \text{ } \mu\text{m}, 384 \text{ } \mu\text{m})$ (green), $\mathbf{y} = (250 \text{ } \mu\text{m}, 185 \text{ } \mu\text{m})$ (blue) and $\mathbf{y} = (420 \text{ } \mu\text{m}, 417 \text{ } \mu\text{m})$ (purple) for $\alpha' = 13^\circ$.

Figure 3.3: Parameters for the plots are the same as for the two figures above: $r = 170 \text{ } \mu\text{m}$, $\alpha = 0^\circ$ for ON and $r' = 170 \text{ } \mu\text{m}$ and $\alpha' = 7^\circ$ for the OFF ganglion cell mosaic, corresponding to a scaling factor of $S = 8.2$. The size of the receptive field is chosen to be $\sigma_r = 70 \text{ } \mu\text{m}$ and the width of synaptic connection $\sigma_s = 20 \text{ } \mu\text{m}$. The OPM, **Fig. 3.3B**, shows Eqn. (3.13) calculated with Mathematica and plotted with Matlab. The three receptive fields are located at $\mathbf{y} = (1150 \text{ } \mu\text{m}, 0 \text{ } \mu\text{m})$ (red), $\mathbf{y} = (1100 \text{ } \mu\text{m}, -78 \text{ } \mu\text{m})$ (green) and $\mathbf{y} = (1160 \text{ } \mu\text{m}, -150 \text{ } \mu\text{m})$ (blue). **Fig. 3.3F** shows the amplitude spectrum of the receptive field shown in **Fig. 3.2**. **Fig. 3.3G** shows the same amplitude spectrum plotted in polar coordinates with doubled angle (Eqn. (3.17)). **Fig. 3.3B** has been calculated with Mathematica using Eqn. (3.13) for the square region between $[-1500 \text{ mm}, 1500 \text{ mm}]$, in $1024 \text{ px} \times 1024 \text{ px}$. **Fig. 3.3H** is a plot of Eqn. (3.20) in the same region with the same parameters. The same $[-1500 \text{ mm}, 1500 \text{ mm}]$ section is shown for the lattices. **Fig. 3.3J** shows the cyclic distance between **B** and **H** calculated with Matlab.

Figure 3.4: OPMs (shown are sections of size $4\Lambda_c \times 4\Lambda_c$) are calculated with the same parameters as in **Fig. 3.3** ($r = 170 \text{ } \mu\text{m}$, $\alpha = 0^\circ$ for ON and $r' = 170 \text{ } \mu\text{m}$ and $\alpha' = 7^\circ$ for the OFF ganglion cell mosaic). The power spectra are calculated numerically with a Fast-Fourier-Transform (embedded in Matlab) and normalized so that the maximum value is 1. The plotrange is $[-2\Lambda_c^{-1}, 2\Lambda_c^{-1}]$. Analytic results (left column) are obtained from Eqn. (3.13) and Eqn. (3.20). Filtered ($\text{OSI} > 0.25$) OPMs, calculated numerically (right column) are smoothed with a Gaussian of width $\sigma = k_c$, corresponding to a width of $5.2 \cdot 10^{-3} \text{ } \mu\text{m}^{-1}$ or $\sigma = 190 \text{ } \mu\text{m}$ in real space (this is similar to the values stated in the literature: “For visualization, a smooth continuous version of the map is obtained by diffusion of orientations with a Gaussian window of $140 \text{ } \mu\text{m}$ in cortical space” [132]). For this simulation, cortical neurons are aligned in a square lattice with lattice constant $6.5 \text{ } \mu\text{m}$. This is extremely dense, however, it allows to resolve fine features in the power spectra. The entire maps of which **Fig. 3.4C** and **3.4E** are a section have a size of $22 \times 22\Lambda_c^2$. The choice of $440\Lambda_c^2$ is arbitrary. With the parameters given, $\Lambda_c = 1200 \text{ } \mu\text{m}$ (from Eqn. (3.21)) so that the OPM corresponds to $26500 \text{ } \mu\text{m} \times 26500 \text{ } \mu\text{m}$. The OPM (from which **Fig. 3.4A** right is a section) is generated from 4096×4096 cortical neurons aligned in a square lattice. The full OPM (**Fig. 3.4A** right) is filtered and smoothed with Matlab to get **Fig. 3.4E** right.

Figure 3.5: The parameters for the numerics are the same as for **Fig. 3.4**. This is, 4096×4096 cortical neurons generate $22\Lambda_c \times 22\Lambda_c$ maps with scaling factor $S = 8.2$. To each RGC mosaic, Gaussian noise of standard deviation $\sigma = \eta \times r$ is added. Full OPMs, **Fig. 3.5B**, are calculated with the C++ program. These OPMs are filtered for cortical cells with orientation selectiv-

3.4. Materials and Methods

ity index $\text{OSI} > 0.25$ and smoothed with a Gaussian of width $\sigma = 190 \mu\text{m}$ with Matlab to get the OPMs (**A**). power spectra (**C**) and marginal power spectra (**D-G**) are calculated with Matlab. The maxima of the peak (**H**) in the marginal spectrum is calculated with Matlab. The maps, **Figs. 3.5A** and **3.5B**, show $4\Lambda_c \times 4\Lambda_c$ sections, where $\Lambda_c = 1200 \mu\text{m}$ is the theoretical value defined by Eqn. (3.21). Thus, the window size is noise-independent. **Fig. 3.5I** is a histogram of all cortical neuron's angle preference, calculated with Matlab. The curve for every noise level shows data of 20 independent $22\Lambda_c \times 22\Lambda_c$ maps combined.

Figure 3.6: **Fig. 3.6A** shows a map of the original size calculated ($22 \times 22\Lambda_c^2$). **Fig 3.5A** for $\eta = 0.12$ is a section of this map, bottom right. Details of the wavelet-transform and the calculation of the wavelet-coefficients are given below. The numerical evaluation of the wavelet analysis was done with Matlab.

Derivation of Eqn. (3.4)

To carry out the sum in Eqn. (3.2), we write the lattice vectors as

$$\mathbf{x}_j = n \mathbf{s} + m \mathbf{t} + \mathbf{u}$$

where $n, m \in \mathbb{Z}$ and where **s** and **t** are the base vectors of the lattice. If $\mathbf{s} \cdot \mathbf{t} \neq 0$, this sum cannot be evaluated. However, by rewriting the lattice into two lattices with orthogonal base vectors (this is what we accomplish with $\mathcal{L} \rightarrow \mathcal{L}_1 + \mathcal{L}_2$), we can avoid this problem. With orthogonal base vectors, we have to evaluate sums of the form

$$\sum_m \exp \left(\underbrace{\left(\frac{(\mathbf{y} - \mathbf{u}) \mathbf{t}}{\sigma_s^2} + \frac{(\mathbf{x} - \mathbf{u}) \mathbf{t}}{\sigma_r^2} \right) m}_{b} - \underbrace{\left(\frac{\mathbf{t}^2}{2\sigma_r^2} + \frac{\mathbf{t}^2}{2\sigma_s^2} \right) m^2}_{a} \right),$$

Or schematically,

$$\sum_m \exp(am^2 + bm)$$

for some a and b . This sum can be evaluated by firstly, completing the square

$$\sum_m \exp(am^2 + bm) = \sum_m \exp\left(-\frac{b^2}{4a}\right) \exp\left(a\left(m + \frac{b}{2a}\right)^2\right)$$

and secondly by application of a transformation equation [8]

$$\sum_{m=-\infty}^{\infty} e^{-a(m+c)^2} = \sqrt{\frac{\pi}{a}} \sum_{m=-\infty}^{\infty} e^{-\frac{\pi^2}{a}m^2 + 2\pi i mc},$$

3. HEXAGONAL RGC MOSAICS AND OPMs

where $c = b/(2a)$. Finally, the result is written to match the sum representation of the Jacobi theta function (this is the definition which is embedded in Mathematica. Other definitions are summarized in Whittaker and Watson's book p. 487 [179]).

$$\begin{aligned} \sum_m \exp(am^2 + bm) &= \sum_m \exp\left(-\frac{b^2}{4a}\right) \exp\left(a\left(m + \frac{b}{2a}\right)^2\right) \\ &= \sqrt{\frac{\pi}{-a}} \exp\left(-\frac{b^2}{4a}\right) \sum_m e^{\frac{\pi^2}{a}m^2 + \pi im\frac{b}{a}} \\ &= e^{-\frac{b^2}{4a}} \sqrt{\frac{\pi}{-a}} \Theta_3\left(\frac{b\pi}{2a}, e^{\frac{\pi^2}{a}}\right) \end{aligned}$$

The same result (after rewriting $\mathcal{L} \rightarrow \mathcal{L}_1 + \mathcal{L}_2$) can be calculated with Wolfram Mathematica.

Derivation of Eqn. (3.9)

As explained in the text, we start with the Fourier spectrum of the receptive field

$$\frac{1}{2\pi} \int d^2x e^{-i\mathbf{k}\mathbf{x}} \exp\left(-\frac{(\mathbf{x} - \mathbf{x}_j)^2}{2\sigma_r^2}\right) = \exp\left(-i\mathbf{k}\mathbf{x}_j - \frac{1}{2}\mathbf{k}^2\sigma_r^2\right) \sigma_r^2.$$

From there, the calculation follows the same procedure as the sum above.

The Validity of the Quadratic Approximation

To test the validity of the quadratic approximation, we have calculated a representation of power spectra, shown left hand side of **Fig. 3.8**, with Eqn. (3.9). The same power spectra with quadratic approximation to the anisotropic term, Eqn. (3.12), are shown on the right hand side of **Fig. 3.8**. The parameters to calculate the power-spectra are summarized in **Tab. 3.4**. Besides the estimation given in the text, this illustrates the validity of the quadratic approximation: It works well for dipole shaped power spectra, however, fails to deliver reasonable values for multimodal receptive fields as shown in **Fig. 3.8A**, case b. This price is acceptable since it is generally difficult to define a preferred stimulus k_{pref} , ϑ_{pref} for this kind of receptive fields.

Exploring the Solutions of Eqn. (3.5) and Eqn. (3.9)

How do receptive fields, Eqn. (3.5), and their power spectra, Eqn. (3.9), change upon a different choice of parameters σ_r and σ_s ? This is shown in **Fig. 3.9**. For all subplots, the center of the cortical receptive field (indicated by the red dot) is fixed. The left two columns, **Fig. 3.9A** show how increasing σ_s acts on

3.4. Materials and Methods

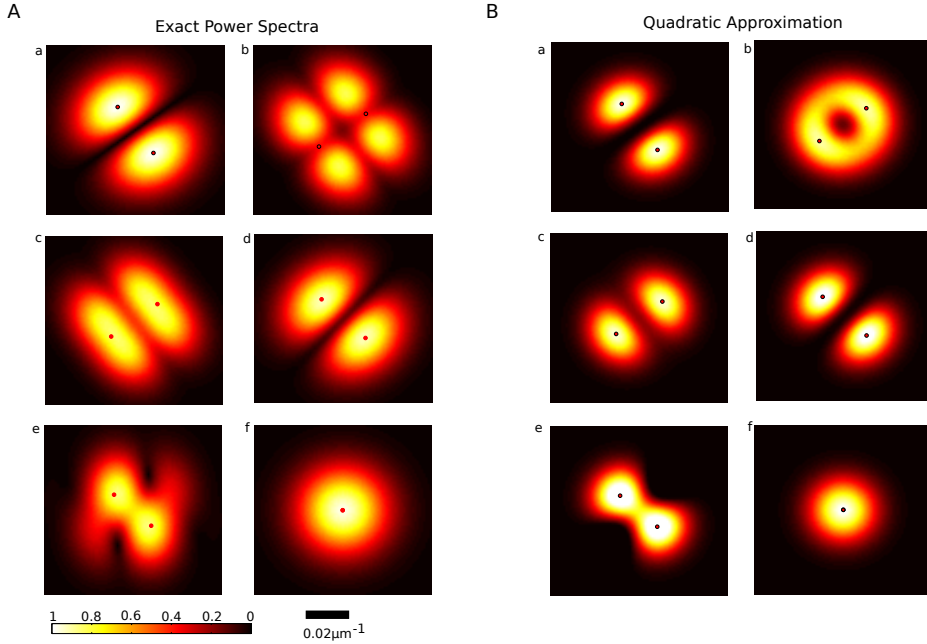


Figure 3.8: Comparison between the full power spectra, Eqn. (3.9), and the quadratic approximation, Eqn. (3.12). **A** Shown are 6 power spectra, labeled a-f. The red dots mark the approximate position of the amplitude spectrum's maximum using the quadratic approximation. **B** Shown are 6 power spectra where the anisotropic part has been expanded to quadratic order. The red dots are at the same position as in A. Note that although the overall-shape of the power spectra differs, the estimation for the maximum is very good. This holds except for the non-dipole shaped amplitude spectrum (b).

the receptive field (left) and the amplitude spectrum (right). For very small σ_s , a cortical cell samples from the closest RGC. This generates a receptive field with a single dominant subregion, in this case OFF-like (**a**). The associated amplitude spectrum has a very strong DC component. This receptive field responds to a constant illumination. With increasing σ_s , more retinal receptive fields contribute to the cortical receptive field. Beginning with the two nearest neighbors to the center of the cortical cell's receptive field with a dipole-shaped amplitude spectrum (**b**), the receptive fields increase in complexity until so many RGC contribute that the hexagonal structure of ON and OFF mosaic are clearly visible (**f**). Cortical receptive fields including several RGCs with Gaussian weights are very complex. It is not straight-forward to come up with a good definition of preferred orientation because tuning curves (**d-f**) become multimodal. The right two columns, **Fig. 3.9B** show how decreasing σ_r acts on receptive fields. Decreasing σ_r creates smaller and smaller receptive

3. HEXAGONAL RGC MOSAICS AND OPMs

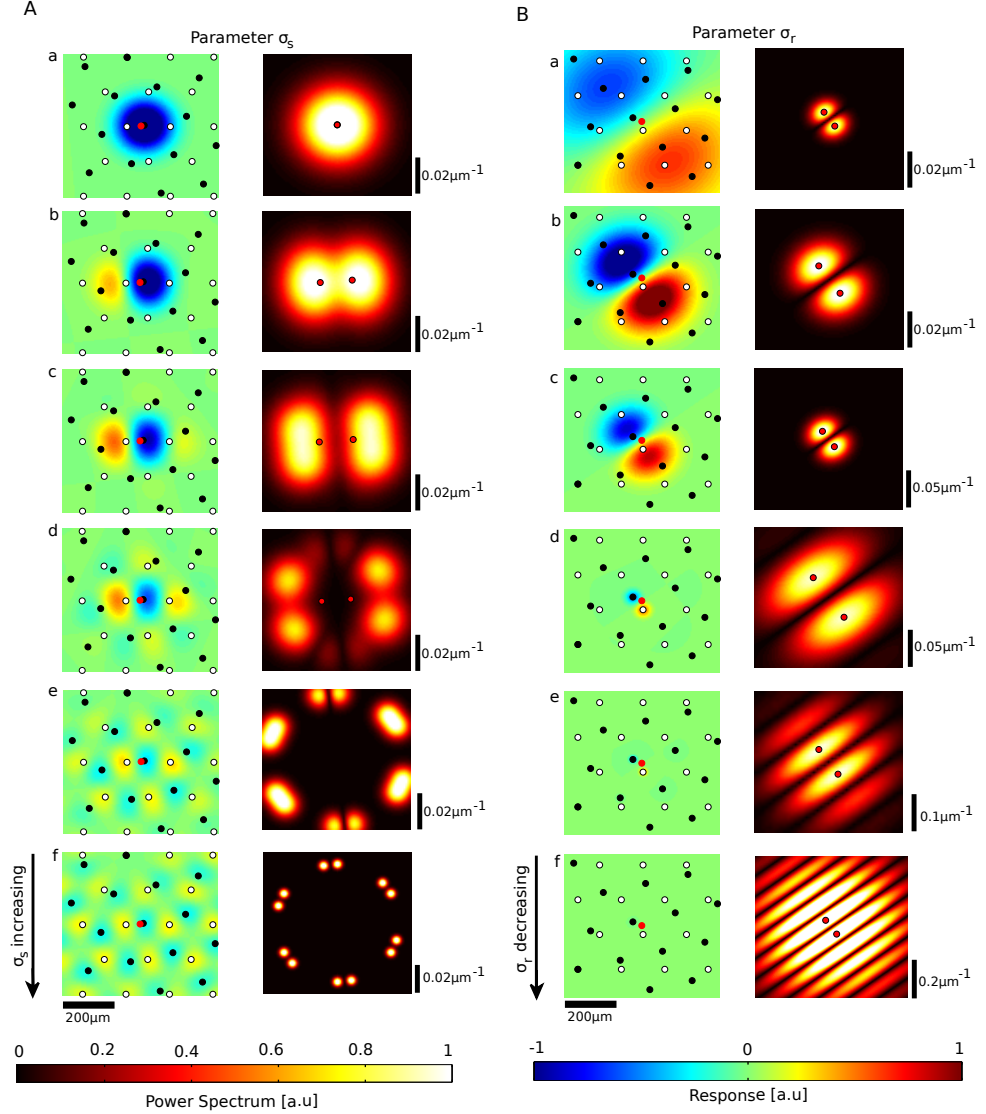


Figure 3.9: Illustration how receptive fields change upon variation of σ_r and σ_s . **A** A sequence of 6 figures (a-f) is shown. From a to f, the value of σ_s is increasing as summarized in Table 3.5. The left sequence of figures shows the receptive field, the right sequence shows the amplitude spectrum. **B** The same sequence as in A is shown, however, this time σ_s is fixed and σ_r is decreasing towards f.

3.4. Materials and Methods

Plot	x	y	α	r	α'	r'	σ_r	σ_s	ϑ_{pref}	k_{pref}
a	250	185	0	170	13°	170	70	20	-0.9338	0.0137
b	300	220	0	170	13°	170	70	20	0.6347	0.0133
c	300	215	0	170	13°	170	70	20	0.6346	0.0131
d	300	120	0	170	13°	170	70	20	-0.7477	0.0137
e	0	750	0	170	13°	170	70	20	-0.7199	0.0113
f	650	150	0	170	13°	170	70	20	0.0848	0

Table 3.4: Parameters for the example power spectra and the quadratic approximation, shown in **Fig. 3.8**. The point $\mathbf{y} = (x, y)$ is the coordinate. The preferred stimulus ϑ_{pref} and k_{pref} are derived from the maximum of the quadratic approximation. The point $(k_{\text{pref}} \cos(\vartheta_{\text{pref}}), k_{\text{pref}} \sin(\vartheta_{\text{pref}}))$ is indicated as red dot in **Fig. 3.8**. Width is given in μm , angle in degree, spatial frequency in μm^{-1} .

fields. These small receptive fields have increasing preferred spatial frequencies (**Figs. a-c**). If σ_r decreases beyond a threshold $\sigma_r \approx d/2$ where d is the distance between two RGCs, the cortical cell's receptive field responds to higher harmonics of the stimulus (**Figs. d-e**). This is easy to understand for point-like ON and OFF center cells. If two of these cells are positioned in a distance d , they respond to frequencies as soon as the condition

$$k_{\text{pref}} = \left(n + \frac{1}{2} \right) \cdot \frac{2\pi}{d} \quad \text{for} \quad n \in \{0, 1, 2, \dots\}$$

is fulfilled. This effect creates the complicated power spectra observed in (**e-f**).

Of course, a wide range of these values is not physiologically reasonable, however, we gain an understanding of how cortical receptive fields look like in the Soodak-Ringach model. The parameters for the plot in **Fig. 3.9** are given in **Tab. 3.5**. It should be noted that connections between several RGCs to generate typical cortical receptive field with distinct ON and OFF subregions [141] cannot be realized with the Soodak-Ringach model.

From Eqn. (3.9) to Eqn. (3.18)

Firstly, we rewrite Eqn. (3.9) as sum by expanding the theta functions,

$$\begin{aligned} \mathcal{R}(\mathbf{k})_{\alpha,r}^s &= \frac{2\pi\sigma_r^2\sigma_s^2}{\sqrt{3}r^2} e^{-i\mathbf{ky}} e^{-\frac{1}{2}\mathbf{k}^2(\sigma_r^2+\sigma_s^2)}. \\ &\cdot \sum_{m,n} e^{-\frac{2\pi^2\sigma_s^2}{3r^2}n^2} e^{-\frac{2\pi^2\sigma_s^2}{r^2}m^2} (1 + (-1)^{m+n}) e^{2inc\mathbf{e}_\phi + 2im\mathbf{c}\mathbf{e}_r}. \end{aligned}$$

3. HEXAGONAL RGC MOSAICS AND OPMs

Fig.	x	y	α	r	α'	r'	σ_r	σ_s	ϑ_{pref}	k_{pref}
A (a)	650	150	0	170	13°	170	70	20	0.08477	0
A (b)	650	150	0	170	13°	170	70	50	0.07811	0.008787
A (c)	650	150	0	170	13°	170	70	70	0.07736	0.009323
A (d)	650	150	0	170	13°	170	70	100	0.07735	0.007968
A (e)	650	150	0	170	13°	170	70	200	-	-
A (f)	650	150	0	170	13°	170	70	500	-	-
B (a)	250	185	0	170	13°	170	200	20	-0.9338	0.004975
B (b)	250	185	0	170	13°	170	100	20	-0.9338	0.009806
B (c)	250	185	0	170	13°	170	70	20	-0.9338	0.01374
B (d)	250	185	0	170	13°	170	20	20	-0.9338	0.03536
B (e)	250	185	0	170	13°	170	10	20	-0.9338	0.04472
B (f)	250	185	0	170	13°	170	4	20	-0.9338	0.049029

Table 3.5: Parameters for the plots in **Fig. 3.9**. The point $\mathbf{y} = (x, y)$ is the coordinate. The preferred stimulus ϑ_{pref} and k_{pref} are calculated using the quadratic approximation. The dash indicates that the algorithm did not converge: for those spectra, the DC component is almost zero and so is the curvature. Width is given in μm , angle in degree, spatial frequency in μm^{-1} .

Since $e^{-i\mathbf{k}\mathbf{y}}$ is a phase which disappears as soon as the absolute value is taken, we neglect it from now. Next, we complete the square using

$$e^{-\frac{1}{2}\mathbf{k}^2(\sigma_r^2 + \sigma_s^2) - \mathbf{a}\mathbf{k}} = \exp\left(-\frac{\sigma_s^2 + \sigma_r^2}{2}\left(\mathbf{k} + \frac{1}{\sigma_s^2 + \sigma_r^2}\mathbf{a}\right)^2 + \frac{\mathbf{a}^2}{2(\sigma_s^2 + \sigma_r^2)}\right)$$

to obtain

$$\mathcal{R}(\mathbf{k})_{\alpha,r}^s = \sum_{m,n} G_{\alpha,r}(m, n) \exp\left(-\frac{\sigma_s^2 + \sigma_r^2}{2}(\mathbf{k} + \mathbf{K}_{\alpha,r}(mn))^2\right)$$

where

$$\begin{aligned} G_{\alpha,r}(m, n) &= \frac{2\pi\sigma_r^2\sigma_s^2}{\sqrt{3}r^2} e^{-\frac{2\pi^2\sigma_s^2}{3r^2}n^2} e^{-\frac{2\pi^2\sigma_s^2}{r^2}m^2} (1 + (-1)^{m+n}) e^{2i\mathbf{y}(n\mathbf{e}_\phi + m\mathbf{e}_r)}. \\ &\quad \cdot \exp\left(\frac{(2n\sigma_s^2\mathbf{e}_\phi + 2m\sigma_s^2\mathbf{e}_r)^2}{2(\sigma_s^2 + \sigma_r^2)}\right) \\ \mathbf{K}_{\alpha,r}(m, n) &= -\frac{2\sigma_s^2}{\sigma_s^2 + \sigma_r^2} (n\mathbf{e}_\phi + m\mathbf{e}_r). \end{aligned}$$

3.4. Materials and Methods

To calculate the absolute value of this expression, we multiply by the complex conjugate to get the following expression

$$|\mathcal{R}(\mathbf{k})|^2 = \sum_{mnop} \left(D_{\alpha,r} \exp \left(-(\sigma_r^2 + \sigma_s^2) \left(\mathbf{k} + \frac{\mathbf{K}_{\alpha,r}(m,n) + \mathbf{K}_{\alpha,r}(o,p)}{2} \right)^2 \right) + \right. \\ + D_{\alpha',r'} \exp \left(-(\sigma_r^2 + \sigma_s^2) \left(\mathbf{k} + \frac{\mathbf{K}_{\alpha',r'}(m,n) + \mathbf{K}_{\alpha',r'}(o,p)}{2} \right)^2 \right) + \\ \left. + E_{\alpha,r,\alpha',r'} \exp \left(-(\sigma_r^2 + \sigma_s^2) \left(\mathbf{k} + \frac{\mathbf{K}_{\alpha,r}(m,n) + \mathbf{K}_{\alpha',r'}(o,p)}{2} \right)^2 \right) \right)$$

where

$$D_{\alpha,r} = G_{\alpha,r}(m,n)G_{\alpha,r}^*(o,p) \exp \left(-\frac{\sigma_s^2 + \sigma_r^2}{4} (\mathbf{K}_{\alpha,r}(m,n) - \mathbf{K}_{\alpha,r}(o,p))^2 \right)$$

$$E_{\alpha,r,\alpha',r'} = -2\text{Re}(G_{\alpha,r}(m,n)G_{\alpha',r'}^*(o,p))$$

$$\exp \left(-\frac{\sigma_s^2 + \sigma_r^2}{4} (\mathbf{K}_{\alpha',r'}(m,n) - \mathbf{K}_{\alpha,r}(o,p))^2 \right).$$

The indices m, n, o, p run over both, negative and positive values, subsequently adding pairs of Gaussians. Re denotes real part. This expression corresponds to Eqn. (3.15). Note that the low-frequency contributions are part of the sum with the E coefficients, because this is where both, $\mathbf{K}_{r,\alpha}$ and $\mathbf{K}_{r',\alpha'}$ appear. Using the definition of G , these coefficients can be written as

$$E_{\alpha,r,\alpha',r'}(m,n,o,p) \propto \exp(i\mathbf{y}(2n\mathbf{e}_\phi + 2m\mathbf{e}_r - 2o\mathbf{e}'_r - 2p\mathbf{e}'_\phi))$$

which is what we need. The low-frequency contributions (the part of the sum with the E -coefficients) to μ are thus

$$\begin{aligned} \mu_{\text{lf}}(\mathbf{y}) &= \sum_{m,n,o,p} E_{\alpha,r,\alpha',r'}(m,n,o,p, \mathbf{y}) \left| \frac{\mathbf{K}_{\alpha,r}(m,n) + \mathbf{K}_{\alpha',r'}(o,p)}{2} \right| . \\ &\quad \cdot \exp \left(2i \arg \left(\frac{\mathbf{K}_{\alpha,r}(m,n) + \mathbf{K}_{\alpha',r'}(o,p)}{2} \right) \right) \\ &= \sum_{m,n,o,p} \exp(2i\mathbf{y}(n\mathbf{e}_\phi + m\mathbf{e}_r - o\mathbf{e}'_r - p\mathbf{e}'_\phi)) \cdot f(m,n,o,p) \end{aligned}$$

which is Eqn. (3.18). f is defined so that it contains all coefficients.

Derivation of the Factor between Moiré-Pattern Lattice Constant and the Typical Scale

The lattice constant of the Moiré-Interference pattern is $f = S \times r$. In the following lines we show that the peaks of the reciprocal lattice are located at

3. HEXAGONAL RGC MOSAICS AND OPMs

$\frac{4\pi}{\sqrt{3}f}$. We follow an approach from crystallography [99].

The primitive translation vectors of a hexagonal lattice are

$$\mathbf{a}_1 = \begin{pmatrix} 1 \\ 0 \\ 0 \end{pmatrix} f \quad \mathbf{a}_2 = \begin{pmatrix} 1 \\ \sqrt{3} \\ 0 \end{pmatrix} \frac{f}{2} \quad \mathbf{a}_3 = \begin{pmatrix} 0 \\ 0 \\ 1 \end{pmatrix} f \quad (3.23)$$

with f as lattice constant. \mathbf{a}_3 is chosen arbitrarily to expand the lattice to three dimensions. The absolute values of the three primitive vectors of the reciprocal lattice [99]

$$\begin{aligned} \mathbf{b}_1 &= 2\pi \frac{\mathbf{a}_2 \times \mathbf{a}_3}{\mathbf{a}_1(\mathbf{a}_2 \times \mathbf{a}_3)} \\ \mathbf{b}_2 &= 2\pi \frac{\mathbf{a}_3 \times \mathbf{a}_1}{\mathbf{a}_1(\mathbf{a}_2 \times \mathbf{a}_3)} \\ \mathbf{b}_3 &= 2\pi \frac{\mathbf{a}_1 \times \mathbf{a}_2}{\mathbf{a}_1(\mathbf{a}_2 \times \mathbf{a}_3)} \end{aligned}$$

are thus

$$|\mathbf{b}_1| = |\mathbf{b}_2| = \frac{4\pi}{\sqrt{3}f}$$

and $|\mathbf{b}_3| = \frac{2\pi}{f}$. The reciprocal lattice is also a hexagonal lattice, however, rotated by 30° in respect to the original lattice.

An Approximation of the Standard Deviation of the Moiré-Pattern Perturbation

In this section, we estimate the standard deviation of the Moiré-Vertex shift if both lattices \mathcal{L}_1 and \mathcal{L}_2 are subject to Gaussian noise of standard deviation σ . For simplicity, we assume both lattices to have the same lattice constant r so that $\sigma = \eta r$. This is illustrated in **Fig. 3.10**. One standard deviation for the lattice points is indicated by the gray shaded areas. The rhombic intersection of both is the region in which we expect the vertex of the Moiré-Pattern to shift. Firstly we notice that this area is not isotropic. The vertex can move with the approximate standard deviation σ_1 along the long diagonal whereas movement along the short one is not as prominent with standard deviation σ_2 . Although we expect the likelihood for a single vertex shift to be anisotropic, we should keep in mind that there are many Moiré-Vertices of different orientation, even within a single row/column. This justifies the notion of a common typical shift σ_M which we now estimate. From simple geometry, we note that $\sigma = k \sin(\Delta\alpha)$, $\sigma_1 = k \sqrt{2(1 - \cos(180^\circ - \Delta\alpha))}$ and

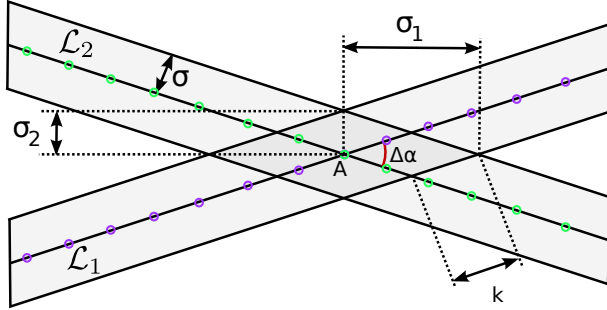


Figure 3.10: The construction for the standard deviation of each Moiré-Pattern vertex. \mathcal{L}_1 and \mathcal{L}_2 show a single row of RGCs of each lattice. RGCs are indicated as green and purple dots. The gray shaded region is the area in which the RGCs are shifted due to noise of amplitude σ . $\Delta\alpha$ is the relative rotation between both lattices. The point A is the noise-free vertex of the Moiré-Pattern. With noise, the vertex moves anisotropically with approximate standard deviations σ_1 and σ_2 .

$\sigma_2 = k \sqrt{2(1 - \cos(\Delta\alpha))}$. This can be rewritten to

$$\begin{aligned}\sigma_1 &= \sigma \sqrt{\frac{2}{1 - \cos(\Delta\alpha)}} = 2S\sigma \\ \sigma_2 &= \sigma \sqrt{\frac{2}{1 + \cos(\Delta\alpha)}} \approx \sigma.\end{aligned}$$

In the last step, we used that $\Delta\alpha$ is small. Next, we present two different methods of estimating σ_M . Assuming the vertex is subject to Gaussian noise, we can calculate the typical shift

$$\langle r \rangle = \int dx \int dy \mathcal{G}(\sigma_1, x) \mathcal{G}(\sigma_2, y) \sqrt{x^2 + y^2}$$

where $\mathcal{G}(\sigma, x)$ is a Gaussian distribution around mean $\mu = 0$ of width σ . Evaluating the integral above can be done with Mathematica. The result is

$$\langle r \rangle = \sqrt{\frac{8}{\pi}} S\sigma E\left(1 - \frac{1}{4S^2}\right) \approx \sqrt{\frac{8}{\pi}} S\sigma$$

where $E(x)$ is the complete elliptic integral of the second kind. Since S is large, we expand the elliptic integral $E(1-x) = 1 - \frac{1}{4}x + \dots$ to leading order. This is done in the last step. Since the typical shift obeys

$$\langle r \rangle = \int dx \int dy \mathcal{G}(\sigma, x) \mathcal{G}(\sigma, y) \sqrt{x^2 + y^2} = \sigma \sqrt{\frac{\pi}{2}},$$

3. HEXAGONAL RGC MOSAICS AND OPMs

we can estimate the typical perturbation of the Moiré-Pattern as

$$\sigma_M = \sqrt{\frac{2}{\pi}} \langle r \rangle = \frac{4}{\pi} S\sigma \approx S\sigma.$$

A second, very simple method is taking the average of both deviations

$$\sigma_M = \frac{1}{2} (\sigma_1 + \sigma_2) \approx S\sigma,$$

again assuming large S. On first glance, it seems strange to take the average of two standard deviations. In our case it is reasonable, because some of the vertices in a single row/column are shifted with σ_1 , some are shifted with σ_2 . This qualifies the average as a typical shift. Both rather crude estimations yield similar results which we use to derive Eqn. (3.22). Considering the simplicity of this derivation, it is remarkable how well Eqn. (3.22) describes the data. We cannot help but wonder if there might be a better way of estimating σ_M .

Wavelet Analysis

To estimate the typical scale of an OPM, we firstly transform the OPM $\vartheta_{\text{pref}}(\mathbf{y})$ to a complex field $z(\mathbf{y}) = \exp(2i\vartheta_{\text{pref}}(\mathbf{y}))$. Next, we calculate wavelet-coefficients defined by

$$\Psi(\mathbf{y}, \Lambda) = \int \frac{d\varphi}{\pi} \left| \int d^2\mathbf{x} z(\mathbf{x}) \cdot \phi_{\mathbf{y}}(\mathbf{x}, \Lambda, \varphi) \right| \quad (3.24)$$

where \mathbf{y} is the position, φ the orientation and Λ the scale of the wavelet $\phi_{\mathbf{y}}(\mathbf{x}, \Lambda, \varphi)$. We are only interested in the typical wavelength of the OPM: therefore we average over the wavelet orientations φ . We use complex Morlet wavelets composed of a Gaussian envelope and a plane wave

$$\phi(\mathbf{x}) = \frac{1}{\sigma} \exp\left(-\frac{\mathbf{x}^2}{2\sigma^2}\right) \cdot \exp(i\mathbf{k}_{\phi}\mathbf{x})$$

and

$$\phi_{\mathbf{y}}(\mathbf{x}, \Lambda, \varphi) = \phi(\Omega^{-1}(\varphi)(\mathbf{y} - \mathbf{x})).$$

The matrix $\Omega(\varphi)$ is the two-dimensional rotation matrix (Eqn. (3.3)). Applying the inverse rotation matrix to the argument $\mathbf{y} - \mathbf{x}$ is equivalent to rotate the wavelet by an angle φ . After fixing Λ , the parameters of the Morlet wavelet are chosen as

$$\begin{aligned} \mathbf{k}_{\phi} &= \frac{2\pi}{\Lambda} \begin{pmatrix} 1 \\ 0 \end{pmatrix} \\ \sigma &= \frac{7\Lambda}{2\pi}. \end{aligned}$$

The factor 7 in the width of the wavelet is chosen as in the literature [96]. The wavelet analysis has been done numerically with Λ equally spaced between $0.2\Lambda_c$ and $4.5\Lambda_c$ in steps of $0.2\Lambda_c$. If the identified local wavelength exceeds $4.1\Lambda_c$, the result is neglected. The orientation average was carried out with 16 equally spaced orientations.

The wavelet-coefficients for fixed position \mathbf{y} as function of Λ are shown in **Fig. 3.6C-3.6E**. **Fig. 3.6** shows the wavelength with the greatest wavelet coefficient

$$\Lambda_0(\mathbf{y}) = \operatorname{argmax}_{\Lambda} (\Psi(\mathbf{y}, \Lambda))$$

calculated for every position \mathbf{y} . To increase the resolution of the wavelength estimation, we included a second wavelength estimation around the result of the first coarse wavelet estimation Λ_0 . The second wavelet analysis runs from -0.2 to 0.2 around the previous result Λ_0 in steps of $\Delta\Lambda = 0.02$. The result gives the value for $\Lambda_{\text{local}}(\mathbf{y})$.

Details for the C++ Code

The results presented here have been calculated with a C++ program in which the Soodak-Ringach model was implemented. This program was written for this thesis and is of the following structure. The class "*rfanalyzer*" contains all the necessary routines. Furthermore, two example files are given: One to calculate the properties of a single neuron, "*calculate_single_neuron.cpp*", and one to calculate a map of these properties "*calculate_map.cpp*". In the following lines, we describe this program and its performance in comparison to the exact results.

The class "*rfanalyzer*" firstly generates a noisy hexagonal lattice. This lattice is stored on the hard drive as a list of point coordinates. It generates two files, one for the ON and one for the OFF sublattice. These lattices are used to calculate receptive fields. Secondly, a neuron's receptive field is calculated by summation of RGC receptive fields. This cortical receptive field is stored as a matrix. The size of this matrix is determined by the parameters *scale* and *points*. *scale* is measured in μm . A square of this side-length, from $-\text{scale}/2$ to $\text{scale}/2$, is the region in which the RF is calculated. This square is sampled into a grid of size *points*². The matrix with *points* \times *points* entries is the form in which the RF is stored and processed. This matrix is Fourier transformed using the GNU scientific library. Next, a search is performed for the entire transformed matrix for the entry with greatest absolute value. Eqn. (3.10) is implemented by an element wise multiplication. The spatial frequency with greatest orientation selectivity is estimated by finding the greatest OSI, Eqn. (3.11), calculated for a list of the spatial frequencies, equally binned between 0 and $2 \times k_{\text{crit}}$ (see Eqn. (3.14)) in steps of $0.001 \times 2\pi/\text{scale} \approx 0.0000013 \mu\text{m}^{-1}$. All integrals are carried out as sums

3. HEXAGONAL RGC MOSAICS AND OPMs

of matrix entries. Increasing the number of matrix entries or an interpolation would make the results more precise, however, slows down the code substantially. We use the given version of the code as a reasonable compromise between speed and precision. Following the identification of the preferred spatial frequency, orientation selectivity for all three options are calculated. Alternatively to the circular variance, we implemented a second measure of orientation selectivity

$$\text{OSI}_c = \frac{\text{TC}(\vartheta_{\text{pref}}) - \text{TC}(\vartheta_{\text{pref}} + \pi/2)}{\text{TC}(\vartheta_{\text{pref}}) + \text{TC}(\vartheta_{\text{pref}} + \pi/2)}. \quad (3.25)$$

Tab. 3.6 shows a comparison between numerically calculated values (for the case $\eta = 0$) and *exact* ones, calculated with Mathematica. Again, we find that this C++ program is a good trade-off between numerical precision and speed. Since all cortical neurons are independent, this program can easily be

Parameter	C++ Program	exact
ϑ_{pref}	-0.747703	-0.747703
$k_1 \equiv \text{argmax}_{\{k\}}(\mathcal{R}(\mathbf{k}))$	0.0124401	0.01276
$k_2 \equiv \mu $	0.00484116	0.00484116
$k_3 \equiv \text{argmax}_{\{k\}}(\text{OSI}(k))$	0.0175376	0.0178287
$\text{OSI}_c(k_1)$	0.596224	0.606767
$\text{OSI}_c(k_2)$	0.337576	0.307671
$\text{OSI}_c(k_3)$	0.668642	0.679553
$\text{OSI}(k_1)$	0.253289	0.255566
$\text{OSI}(k_2)$	0.152857	0.148103
$\text{OSI}(k_3)$	0.269673	0.265418

Table 3.6: Test run for the neuron located at $\mathbf{y} = (300, 121)$. A comparison between values calculated with the C++ program and exact results calculated with Mathematica. Both agree within $\approx 1\%$. The RF considered here is the one shown in **Fig. 3.1C** and **Fig. 3.2A**. Therefore some of the values here are also given in **Tab. 3.1**. Angles are measured in rad, spatial frequency is measured in μm^{-1} .

parallelized. The program *"calculate_map.cpp"* contains code which calculates a single strip of an OPM. We used this methods to calculate large OPMs on a cluster computer. **Tab. 3.7** summarizes the parameters used. The parameters *scale* and *points* are discussed above. The parameter *boxlim* is the side length of the OPM which is calculated. Its value is given in μm . The OPMs calculated by this code have a square shape. The parameter *length* is the number of pixels per side in which the OPM is stored.

For the parameters given in **Tab. 3.7**, the scaling factor is $S = 8.2$, therefore $\Lambda_c = 1206 \mu\text{m}$. The entire OPM calculated is thus $\text{boxlim}/\Lambda_c = 27564/1206 \approx 22.86\Lambda_c$ wide. We make sure to avoid boundary effects by cutting off 80px

3.4. Materials and Methods

from each edge. Thus the final map created has a width of $4096 \times 4096 px^2$ ($length - 160 = 4096$) measured in $22.86 \times 4096/4256 \approx 22.00\Lambda$.

Parameter	Name in Program	Typical Value
$\sigma_s [\mu m]$	sigmas	20
$\sigma_r [\mu m]$	sigmar	70
$r [\mu m]$	r	170
$r' [\mu m]$	rd	170
α in rad	alpha	0
α' in rad	alphad	$7\pi/180$
η	eta	0
Size of RF in μm	scale	5000
Size of matrix for the RF	points	256
Max. number of RGCs used	MAX	99950
Side length of the square [μm]	boxlim	27564
Side length of the square [px]	length	4256
Path data storage	path	"./"
Random Seed	seed	1

Table 3.7: Typical parameters for the program written for this thesis to calculate orientation preference maps.

APERIODIC RGC MOSAICS AND OPMS

“Die gegenwärtige Welt eröffnet uns einen so unermeßlichen Schauplatz von Mannigfaltigkeit, Ordnung, Zweckmäßigkeit und Schönheit, man mag diese nun in der Unendlichkeit des Raumes, oder in der unbegrenzten Teilung desselben verfolgen, daß selbst nach den Kenntnissen, welche unser schwacher Verstand davon hat erwerben können, alle Sprache, über so viele und unabsehlich große Wunder, ihren Nachdruck, alle Zahlen ihre Kraft zu messen, und selbst unsere Gedanken alle Begrenzung vermissen, so, daß sich unser Urteil vom Ganzen in ein sprachloses, aber desto beredteres Erstaunen auflösen muß.”

Immanuel Kant: “Kritik der reinen Vernunft” [91]

4. APERIODIC RGC MOSAICS AND OPMs

4.1 INTRODUCTION

Orientation preference of primary visual cortical neurons is organized into a functional map across the surface of the cortex. These maps have been observed in cats [34, 151], tree shrews [18], galagos [184], ferrets[25, 177] and many primates [126], including humans [185]. Orientation preference maps (OPMs) are aperiodic with a typical scale [94, 95]. They contain topological defects [16, 17, 120, 126, 161, 181] on a cellular level [130] which can be used to quantify the statistical properties of these maps [96, 98]. Remarkably, OPMs show universal statistical properties, indicating a common underlying origin for these different species. Most theories to account for the observed universality rely on intracortical neurocircuitry creating neural orientation tuning which self-organizes into OPMs (e.g. [47, 101, 127, 161, 180, 181]). However, a very simple model has recently been proposed [132] interpreting OPMs as a geometric effect.

ON/OFF center ganglion cells in the retina with distinct center-surround receptive fields project to the lateral geniculate nucleus (LGN) of the thalamus. Thalamic receptive fields mirror retinal receptive fields in shape, size and spatial distribution [28, 29] and project directly into the cortex. Orientation preference of cortical neurons is created by an elongated receptive field with distinct ON and OFF subregions [141]. This receptive field can be modeled as a linear sum of center-surround geniculate receptive fields [79, 80]. A location on the surface of the cortex corresponds to a specific position in visual space. This is called retinotopy [38, 45, 163, 166] and allows two neighboring retinal/thalamic ON and OFF center cells to project to neighboring neurons in the cortex. Most nearest neighbor cells are ON/OFF pairs [174]. Assuming cortical neurons to sample exclusively from geniculate projections in their vicinity [2], this creates receptive fields dominated by a single ON and OFF subregion [143]. These *dipoles* resemble cortical receptive fields. Consequently, orientation preference across the surface of the cortex should mirror the dipole distribution of the ON/OFF center ganglion cell mosaic in the retina [143, 153, 154]. Since this model builds on previous studies by Soodak, we refer to it as the Soodak-Ringach model. Without any order in the ganglionic mosaic, it is difficult to account for the typical scale of OPMs. As solution, Paik and Ringach [131, 132] suggested to model ON and OFF cell mosaics as two hexagonal lattices. Superposing two lattices creates an interference effect, a so-called Moiré-Pattern. This pattern is mapped into the cortex and creates a map with a typical scale, set by the scale of the Moiré-Pattern.

Although this model creates OPMs which on first sight look realistic, there are two major drawbacks. Firstly, OPMs created by the Soodak-Ringach model have statistical properties and power spectra distinct from experimentally observed ones. This is what we showed in the previous chapter. Secondly, the ganglion cell mosaic is not hexagonal. Instead of using noisy hexagonal lattices [143], ganglion cell mosaics in agreement with experimental data have

successfully been simulated using pairwise interacting point processes [48, 76, 186]. These mosaics are non-random but aperiodic: there is no long-range order which would be necessary to create a Moiré-Interference pattern. The explicit long range order is a key difference between a hexagonal lattice and a PIPP mosaic [76]. OPMs calculated from PIPP mosaics do not express a typical scale due to the absent correlation between ON and OFF lattice [76, 143, 144]. These two findings challenge the assumptions of hexagonal mosaics and the Moiré nature of OPMs and lead to the question: can one find an aperiodic RGC mosaic whose ON/OFF dipoles generate an OPMs and which shows the same statistical properties as experimentally observed mosaics [48, 76]?

To answer this question we start with model OPMs, generated as maximum entropy ensemble [148] from experimentally observed cat marginal power spectra. We develop a method to reverse-engineer a ganglion cell mosaic of which the dipoles correlate with a seeding model OPM. The reverse-engineering algorithm presented in this chapter builds on previous work on pairwise interacting point processes (PIPPs) [48, 76]. We present a parsimonious extention of this PIPP model because it is known to fit the data. Nonetheless it is an extention to obtain OPMs with typical columns spacing. Since there is no direct way of enforcing a certain dipole correlation function in a PIPP, the approach of encoding the correlation in the pairwise interaction seems obvious. After the presentation of the algorithm, we show that it is possible to find an aperiodic ganglion cell mosaic which generates OPMs with typical column spacing. We analyze the statistical properties of the ganglion cell mosaics obtained and find that distance-statistics agree well with experimentally observed mosaics. A requirement for creating an OPM from the ganglion cell mosaic is the angular correlation of ON/OFF dipoles, corresponding to the angular correlation of the OPM. A recent poster presentation at the *SfN 2012 Meeting* finds angular correlation [133], however, it is unclear how. After quantifying the correlation function of our model mosaics, we compare the results with experimental data from cat beta cell mosaics [172, 186], which are considered to seed OPMs [143, 144]. We find that experimentally observed beta cell mosaics do not have any long-range angular correlations. In summary, this work shows that ganglion cell mosaics do not have the necessary spatial statistics to generate OPMs.

4.2 RESULTS

The model

Should it be the case that the OPMs are already embedded in the mosaic of ganglion cells? To illustrate the train of thought we show a ganglion cell mosaic from a cat retina [173], **Fig. 4.1A**. Two very prominent features are the area centralis, the region of greatest ganglion cell density, corresponding to the greatest visual acuity. A second one is the visual streak, a horizontal

4. APERIODIC RGC MOSAICS AND OPMs

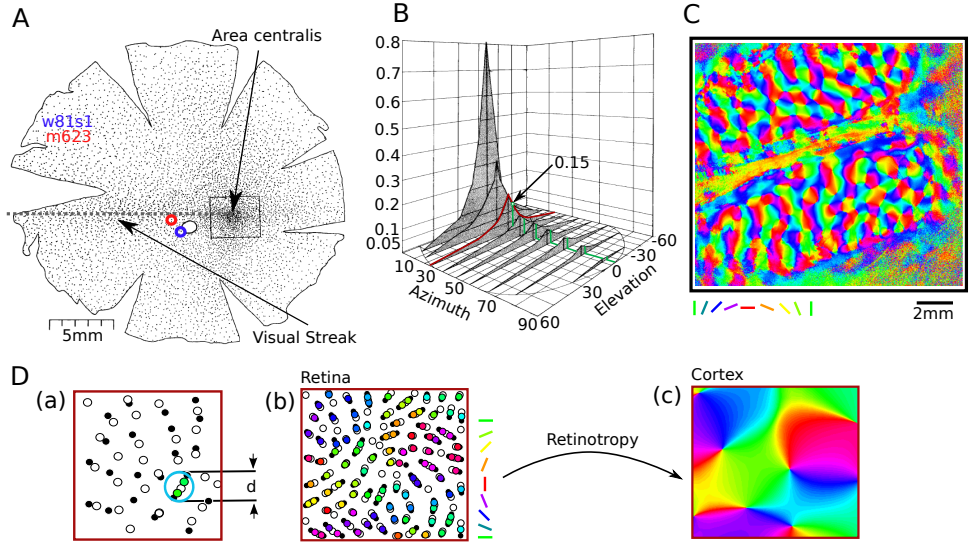


Figure 4.1: **A** Retina of a cat’s left eye with cell positions indicated as dots, measured in a cresyl-violet stained mount [173]. Indicated are two distinct anatomical features, the visual streak and the area centralis (see text). The red and blue circles show the position of two ganglion cell mosaics which we use later. **B** Cortical magnification factor of the cat in mm^2 cortex per deg^2 visual field [166]. The indicated point corresponds to the mosaics used (see text). **C** OPM of a cat primary visual cortex [187]. **D** Defining *dipoles*, neighboring ON/OFF pairs closer than a distance d . The indicated ON cell has two OFF cells in its vicinity, thus creating two dipoles. The color encodes the dipole orientation. The dipole position is half way between ON and OFF cell. **(b)** This particular mosaic of ON/OFF cells creates an OPM. **(c)** The OPM created by the mosaic in **(b)**.

line of relatively high ganglion cell density [146]. Both are indicated in the figure and both features are important below. We have also indicated two points, about 5 mm from the area centralis below the visual streak. They show the position of the ganglion cell mosaics which we use later. The retinal ganglion cells’ position in visual space is mapped into the cortex by cortical magnification, **Fig. 4.1B**. The value of cortical magnification depends on the position in the visual field. The elevation is given in angle above the horizon (the visual stroke). The origin (zero elevation, zero azimuth) is the center of gaze, corresponding to the area centralis. In the primary visual cortex, orientation preference maps can be observed **Fig. 4.1C**. The cortical magnification factor for the published mosaics which we discuss later is indicated in **B**. Ganglion cell somata and their dendritic trees are arranged in an aperiodic and non-random mosaic [174]. There is no evidence that different cell types,

as ON and OFF center cells, have a spatial relationship [76], except that their somata and dendrites do not overlap. However, within one class of neurons, each cell is surrounded by an exclusion zone in which it is unlikely to find another one [48, 76].

We assume a pair of ON/OFF ganglion cells to form a dipole if their distance is smaller than d , a free parameter in this model. A dipole is defined as a vector going from ON to OFF center RGC. The dipole's position is defined as half way between both cells. The dot's color corresponds to the angular orientation. This is shown in **Fig. 4.1D (a)**. Empty circle show ON center cells, filled circles show OFF center cells. In the vicinity of a specific ON center cell, two OFF center cells can be found. This defines two dipoles. In **Fig. 4.1D (b)**, we show the dipoles calculated for a mosaic generated with the algorithm presented in the next section. Already visually, the dipoles' orientation changes more or less smoothly and generates an OPM. **Fig. 4.1D (c)** shows the corresponding OPM created by this mosaic.

An OPM modulated PIPP

Retinal ganglion cells are not distributed randomly. They form an aperiodic mosaic with distinct statistical properties. The properties have been analyzed in detail, specifically regarding the density recovery profiles, autocorrelation function, nearest neighbor distance distribution, topological disorder (measured by the number of edges of voronoi polygons) and the expectation value of finding a cell within a certain distance [48, 76]. This thorough investigation allowed to simulate mosaics with realistic statistical properties, using a Pairwise Interacting Point Process (PIPP), a method of generation a spatial distribution of points. It is called a Pairwise interacting process, because the interaction of points is determined by an interaction function between pairs. The product of the interaction functions for a specific location for all possible pairs of points gives the probability of finding a point at this particular spot. In the model presented here, this works as follows. A number of ganglion cells is randomly distributed and subsequently subjected to an update rule which is repeated for all cells several times until the result converges. A number of n_{ON} ON and n_{OFF} OFF center RGCs are positioned in a patch of the retina of finite size $x \times y$. The ganglion cells' positions \mathbf{x}_{ON}^i and $\mathbf{x}_{\text{OFF}}^j$ are initialized randomly. Following the initialization, the ON ganglion cell i is selected. A new candidate position is assigned randomly and accepted with probability

$$p_i = \prod_{j=1, i \neq j}^{n_{\text{ON}}} h_{11}(|\mathbf{x}_{\text{ON}}^i - \mathbf{x}_{\text{ON}}^j|) \cdot \prod_{j=1}^{n_{\text{OFF}}} h_{12}(|\mathbf{x}_{\text{ON}}^i - \mathbf{x}_{\text{OFF}}^j|) \cdot h_\kappa(\mathbf{x}_{\text{ON}}^i, \mathbf{x}_{\text{OFF}}^j).$$

4. APERIODIC RGC MOSAICS AND OPMs

After updating all ON cell's positions, the procedure is repeated for the OFF center cells, here for the cell number i

$$p_i = \prod_{j=1, i \neq j}^{n_{\text{OFF}}} h_{22}(|\mathbf{x}_{\text{OFF}}^i - \mathbf{x}_{\text{OFF}}^j|) \prod_{j=1}^{n_{\text{ON}}} h_{12}(|\mathbf{x}_{\text{ON}}^j - \mathbf{x}_{\text{OFF}}^i|) \cdot h_\kappa(\mathbf{x}_{\text{ON}}^j, \mathbf{x}_{\text{OFF}}^i).$$

In our simulations, we performed both the ON and the OFF loop 50 times. The functions h_{11} , h_{12} and h_κ are chosen as

$$\begin{aligned} h_{12}(r) &= \begin{cases} 0 & \text{if } r \leq \delta \\ 1 & \text{if } r > \delta \end{cases} \\ h_{22}(r) &= \begin{cases} 0 & \text{if } r \leq \delta \\ 1 - \exp\left(-\left|\frac{r-\delta}{\phi}\right|^\alpha\right) & \text{if } r > \delta \end{cases} \\ h_\kappa(\mathbf{x}, \mathbf{y}) &= \begin{cases} 1 - \exp\left(\kappa(\cos(\arg(\mathbf{x} - \mathbf{y}) - \theta(\frac{\mathbf{x} + \mathbf{y}}{2})) - 1)\right) & \text{if } r \leq d \\ 1 & \text{if } r > d \end{cases} \end{aligned}$$

where $\theta(\mathbf{x})$ is an OPM used to seed the process. The function $h_{22}(r)$ describes the self-interaction of different ON, respectively OFF center RGCs. This function generates an exclusion zone around every RGC in which it is unlikely to find another one. The parameter ϕ is the width and α the slope of the transition distance δ of the interaction function. The function h_{12} captures the interaction between ON and OFF center RGCs. In this case, the somata cannot overlap. The function h_κ employs the OPM. If κ is zero, the OPM does not influence the positioning of the dipoles. In this limit, the PIPP reproduces the methods proposed by Eglen et al. [48]. If κ is large, the angle between ON and OFF ganglion cells is strongly influenced by the OPM. This interaction function aligns dipoles in a way that they reproduce an OPM. We refer to this method as a modulated PIPP (mPIPP). To seed the ganglion cell mosaics, we use OPMs generated with a Gaussian random field, specifically the method proposed in [148]. Instead of using a model marginal amplitude spectrum, we average the spectra of 13 cat OPMs and generate the maximum entropy ensemble for the observed marginal amplitude spectrum. This is shown in **Fig. 4.2**. **Fig. 4.2A** shows a Gaussian random OPM and **Fig. 4.2B** the associated amplitude spectrum. The process of generating a Gaussian random field works as follows. A marginal amplitude spectrum is chosen. A complex matrix is filled with Gaussian entries for real and imaginary part. This matrix is subsequently multiplied with the amplitude spectrum and inversely transformed. The Gaussian OPM is the phase of the result. The experimental power spectra are shown in **Fig. 4.2C**. Pink curves show all marginal power spectra used, the purple drawn line is the mean. All power spectra have been scaled in x so that the maximum is located at 1. For a comparison, **Fig. 4.2D** shows the amplitude spectrum of a cat's OPM. Using this marginal amplitude spectrum and the same Gaussian random map construction, we obtain an OPM as shown in **Fig. 4.2E** with the spectrum as in **Fig. 4.2F**. This is a

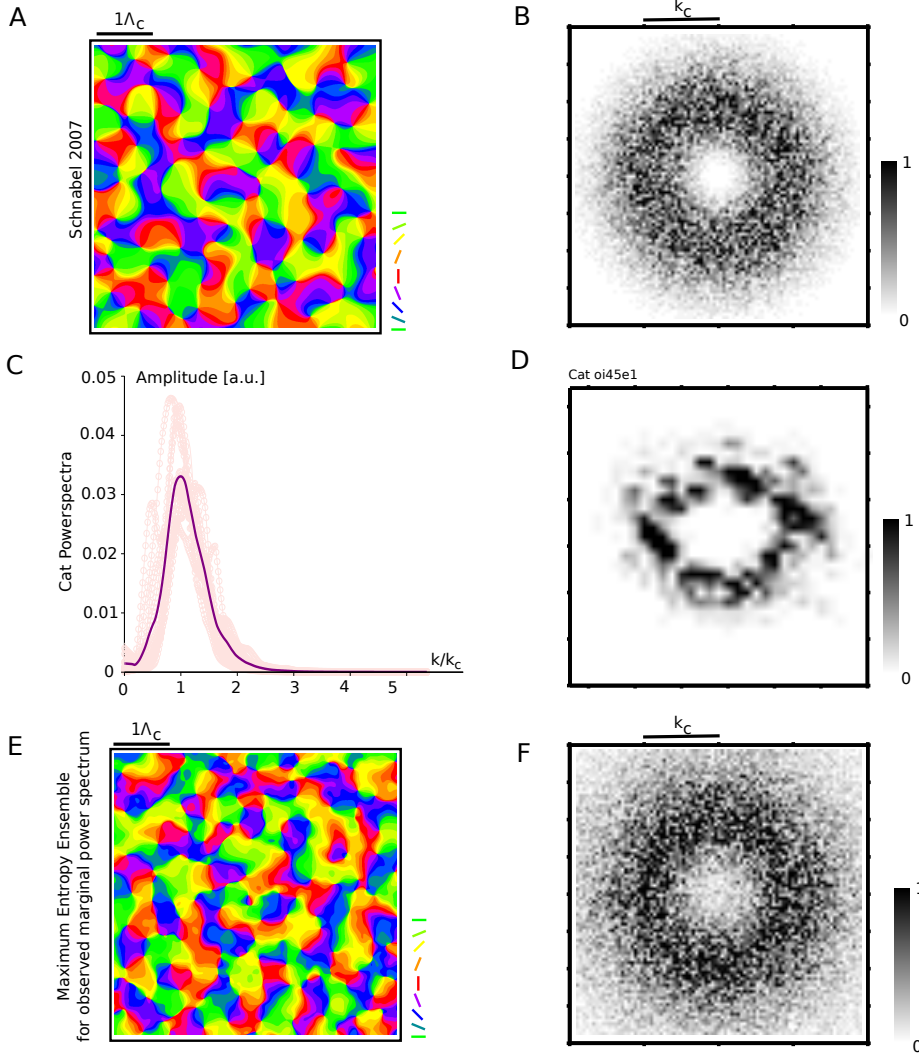


Figure 4.2: **A** A Gaussian random OPM, generated with the algorithm presented in [148]. The parameter used for the spectrum's width is $\beta = 5$. **B** The amplitude spectrum of the map in A. **C** Shown in pink are the marginal power spectra of 13 cat OPMs. The purple drawn line is the average of the maps. All cat maps have been normalized so that the maximum coincides at $k/k_c=1$. **D** An example amplitude spectrum of a cat's OPM. **E** A Gaussian OPM generated with the marginal amplitude spectrum in C. This is a section of the OPM which is used to modulate the PIPP. **F** The amplitude spectrum of the map in E.

4. APERIODIC RGC MOSAICS AND OPMs

fragment of the map used to modulate the PIPP process. It has more high frequency contributions than the original map because the averaged spectrum is slightly wider than a single cat OPM spectrum. It should be noted that the pinwheel density for Gaussian random maps is too large. Nevertheless, we use this method as an approximation for real maps with finite bandwidth.

To evaluate angular correlation, we use the measure proposed by Fisher and Lee [55, 56]. It is equivalent to the Pearson product-moment correlation coefficient for the sine of the angles, respectively the sine of the angle's covariance, normalized with its standard deviation. The circular correlation function is defined as follows. For n dipoles in a retinal patch, there are $n(n - 1)/2$ pairs of dipoles with different distances. We calculate these dipoles and save the distance and the angle of both dipoles in a list. Next, the length is binned from 0 to the size of the diagonal of the rectangular retinal section (the greatest possible distance between two dipoles) in 20 equidistant bins and every dipole pair assigned to the corresponding bin. We store the values $p_i = (\theta_i, \phi_i)$ which are the two angles for each pair of dipoles which falls within this bin. The index i is in the range $i = 1, \dots, t$ where t is the number of dipoles in this distance bin. The circular correlation for the group k is defined as

$$C_k = \frac{\sum \sin(\theta_i - \theta_j) \sin(\phi_i - \phi_j)}{\sqrt{\sum \sin^2(\theta_i - \theta_j)} \sqrt{\sum \sin^2(\phi_i - \phi_j)}}. \quad (4.1)$$

Each summation is in the range $1 \leq i < j \leq p$. A simple statistical error estimation can be done by calculating the standard deviation of the sum in the nominator and denominator and using propagation of error. We define the standard error as

$$\begin{aligned} \text{err}_1 &= \frac{1}{p} \text{std}(\sin(\theta_i - \theta_j) \sin(\phi_i - \phi_j)) \\ \text{err}_2 &= \frac{1}{p} \text{std}(\sin^2(\phi_i - \phi_j)) \\ \text{err}_3 &= \frac{1}{p} \text{std}(\sin^2(\theta_i - \theta_j)). \end{aligned}$$

The function `std()` calculates the standard deviation. Note that we calculate the standard error in terms of p , the number of dipole pairs and not the number of terms in the sums in Eqn. (4.1). We find this estimation more conservative because there are only p independent dipole pairs which can be used to calculate the circular correlation. Subsequently, we use standard error propagation to calculate the error

$$s_k = \sqrt{\left(\frac{\text{err}_1}{\sqrt{m_2 m_3}}\right)^2 + \left(\frac{m_1 m_3}{(m_2 m_3)^{3/2}} \frac{\text{err}_2}{2}\right)^2 + \left(\frac{m_1 m_2}{(m_2 m_3)^{3/2}} \frac{\text{err}_3}{2}\right)^2}. \quad (4.2)$$

for bin k . The numbers m_i are the mean for the sums in Eqn. (4.1) for which err_i is the standard error.

4.2. Results

Secondly, we also implemented a more sophisticated error measure. We used jackknifing to estimate the error as proposed by Fisher [6, 55]. Briefly, for every bin the p dipole pairs are assigned to $g = 5$ groups with p/g dipole pairs in each. Then, we carry out calculation Eqn. (4.1), however, ignoring one of the groups. The standard error can be estimated by

$$s_k = \sqrt{\frac{1}{g-1} \sum_{i=1}^g (C - C_i)^2}$$

where C_i are the results of the jackknife estimation. It seems that his measure substantially underestimates the error. A likely reason is that the total number of dipole pairs is very limited. Thus, these jackknife estimated correlations are very similar to the correlation calculated by all dipole pairs. Because of the more conservative error estimation and the substantially smaller computational effort, we calculate error estimates using propagation of errors. A third option of error estimation, similarly a form of resampling, is bootstrapping. We did not implement this alternative.

The calculation of the correlation function for rectangular patches of retina creates large errors for very small distances (only few dipoles are very close) and large errors for large distances (only dipoles at the edges of the retina patch can contribute). Between the extremes, the error is smaller. Using the model OPM for the described modulated PIPP gives mosaics as shown in **Fig. 4.3**. **Fig. 4.3A** shows a mosaic calculated for $\kappa = 0$ (**(a)**) and $\kappa = 28$ (**Fig. (b)**). A dipole is defined as a vector from ON to OFF. Colored dots are located at the center of these vectors, illustrating dipole positions. The color of the dots indicates the dipole orientation. Black and white dots indicate OFF, respectively ON mosaic. Underlying the mosaic is the OPM used to modulate the PIPP. In the case $\kappa = 0$ the OPM did not influence the mosaic. This reproduces the original PIPP [48]. For $\kappa = 28$, the dipoles are clearly aligned with the OPM. **Fig. 4.3B** shows the dipole correlation function, Eqn. (4.1), for the maps in A. As expected, there is no correlation in the $\kappa = 0$ map, but clear long range order for $\kappa = 28$. The errors are estimated using standard error propagation, Eqn. (4.2), as discussed above. A RGC mosaic which can generate an OPM has a substantial correlation on the scale of $\leq 0.3\Lambda$. This is shown in **(b)** for $\kappa = 28$. **Fig. 4.3C** shows the distance distribution between ON and OFF center cells. In respect to this distribution, there is now significant difference between large and small κ for single mosaics. Calculating these distributions for a substantially greater number of RGCs yields the plots shown in **Fig. 4.3D**. Here we can find a larger ON-OFF nearest neighbor distribution function. Pairs of cells tend to align close to the lower cutoff $\delta = 20 \mu\text{m}$ to form stable dipoles. For the distribution of ON and OFF center cells, there is no significant difference. The parameters used for this simulation are the same as proposed by Eglen et al. [48] and summarized in **Tab. 4.1**. The cells have been distributed using the

4. APERIODIC RGC MOSAICS AND OPMs

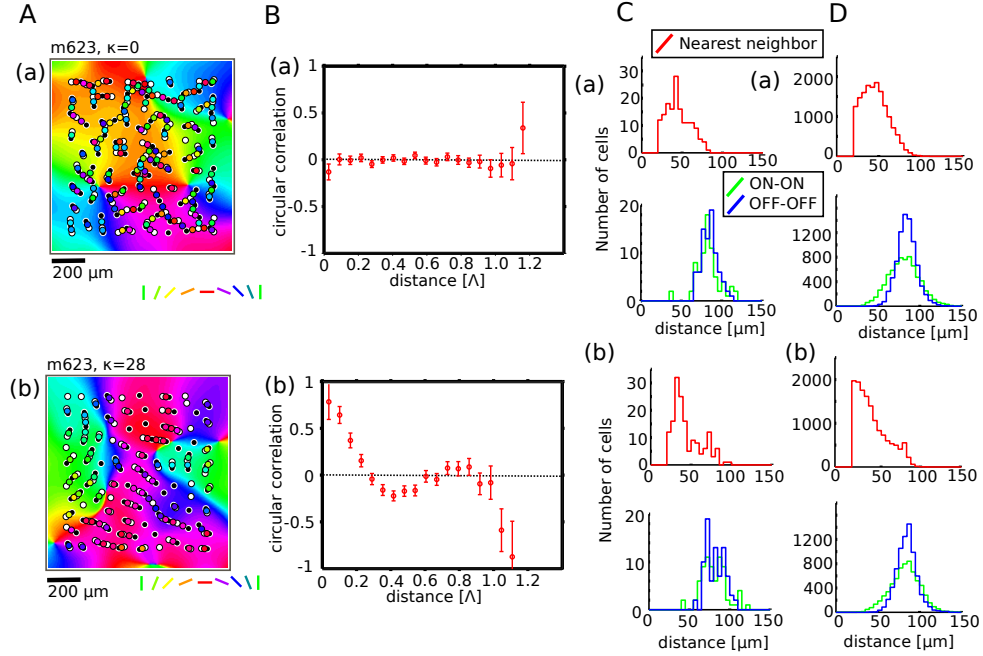


Figure 4.3: **A** The result of the modulated PIPP. Ganglion cells are indicated as empty (ON) and filled (OFF) dots. Dipoles are indicated as colored dots. The color corresponds to the preferred angle as indicated. The underlying OPM is the map which modulates the PIPP. Dipoles have been calculated for $d = 80 \mu\text{m}$. **B** Angular correlation calculated with Eqn. (4.1) for 20 bins for the mosaic shown in A. Empty bins are not shown. The error is estimated with Eqn. (4.2). **C** Nearest neighbor distance distribution of all cells (top) and of ON-ON and OFF-OFF nearest neighbors (bottom). Green is the ON-ON distance, blue is OFF-OFF distance. **D** shows the same ON/OFF distance distribution as C but with data from ≈ 10000 RGCs. The top row (**a**) shows a simulation for $\kappa = 0$, the bottom row (**b**) shows a simulation for $\kappa = 28$. We used the parameters for the m623 mosaic, summarized in **Tab. 4.1**.

4.2. Results

Name	ϕ [μm]	α	δ [μm]	size [μm]	number ON	number OFF
m623 h_{11}	112.79	3.05				
m623 h_{22}	65.46	8.11				
m623 h_{12}			20			
m623 size x				860		
m623 size y				920		
m623 cells					74	82
w81s1 h_{11}	67.94	7.81				
w81s1 h_{22}	66.27	5.40				
w81s1 h_{12}			18			
w81s1 size x				620		
w81s1 size y				820		
w81s1 cells					65	70

Table 4.1: Parameters used for the PIPP to reproduce mosaics with the same statistical properties as the two mosaics m623 and w81s1, shown in **Fig. 4.4**. Values are copied from [48].

parameters for mosaic m623. To summarize, the proposed modulated PIPP generates aperiodic mosaics of ON and OFF center cells of which the dipoles correspond to an OPM. Each ON/OFF mosaics alone does not have substantial long range order, yet they generate OPMs with realistic power spectra. In the next section, we analyze cat X-cell mosaics with respect to ON/OFF dipole correlation. Should the ganglion cell mosaic seed the OPM, we should find this correlation, similarly as it appears in **Fig. 4.3B (b)**.

Correlation in Cat Data

In this section we use cat beta cell mosaics published in [174] (w81s1) and [186] (m623). To our knowledge, these mosaics are the only ones published. These are also the ones used by Eglen et al. to construct the PIPP with the parameters given in **Tab. 4.1**. [48]. The mosaics, neighbor distance distributions, dipoles and angular correlations are shown in **Fig. 4.4**. **Fig. 4.4A** shows the mosaic m623 and **Fig. 4.4B** mosaic w81s1. **(a)** shows the mosaics, copied from [48]. **(b)** shows the distance distribution of the ON/OFF center cells. Red is the distance between nearest neighbors, green is ON-ON and blue is OFF-OFF distance. **Fig. 4.4C** shows the identified ganglion cell ON-OFF dipoles for mosaic m623. **(a)** shows the dipoles found with a critical distance of $d = 50 \mu\text{m}$. **(b)** shows the dipoles found with a critical distance of $d = 80 \mu\text{m}$. Of course, an increasing number of dipoles can be found as the critical distance becomes greater. **Fig. 4.4D** shows the dipoles found for the mosaic w81s1. **Fig. 4.4E** shows the angular correlation function for both mosaics. **(a)** shows the angular correlation for dipoles identified with $d = 50 \mu\text{m}$, **(b)** shows the

4. APERIODIC RGC MOSAICS AND OPMs

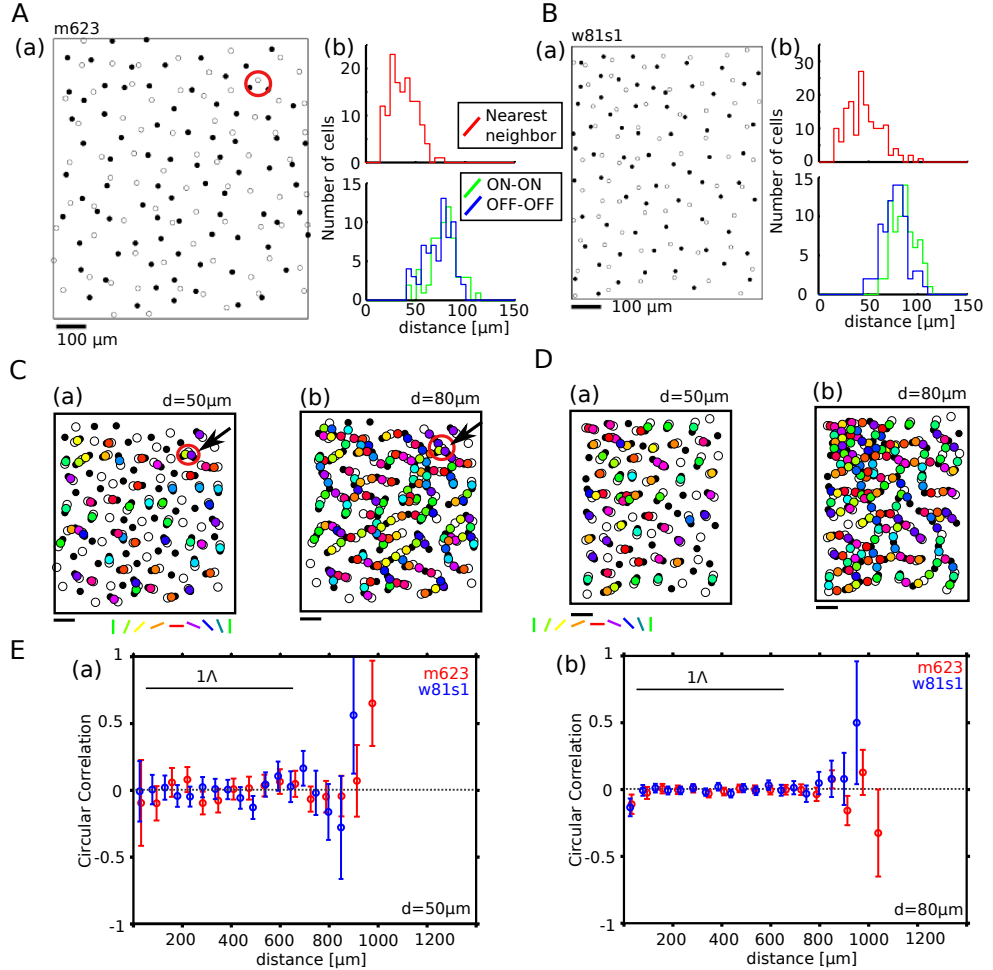


Figure 4.4: **A** Data for the mosaic *m623* [186]. (a) shows the ganglion cell mosaic used (copied from [48]). Black/white symbols indicate OFF/ON center cells. (b) shows the distance distribution between nearest neighbors (red) and ON-ON (green), OFF-OFF pairs (blue). **B** The same as in A for the mosaic *w81s1* [174]. **C** shows the dipoles identified in the mosaics. The bars are 100 μm . (a) shows the dipoles (colored dots) calculated for a distance $d = 50 \mu\text{m}$, (b) shows the dipoles calculated for a distance of $d = 80 \mu\text{m}$. The red circles show the same position in the mosaics and how increasing d increases the number of identified dipoles.

correlation function for dipoles identified with $d = 80 \mu\text{m}$. The dashed line shows the zero correlation line. Errors are estimated with error propagation. This figure illustrates that there is no measurable correlation in the reported mosaics. How much correlation would we expect? To answer this question, we calculate the region of an OPM to which these mosaics correspond. The

center of mosaic w81s1 was located 19° below the mid line of the visual streak, 4mm from the area centralis [186]. For the definition of these terms and for an illustration where this point is located, see **Fig. 4.1A**. We need to reexpress this value in degree visual field to get the cortical magnification factor, **Fig. 4.1B**. Firstly, the coordinates are

$$\begin{pmatrix} 4 \text{ mm} \cos(19^\circ) \\ 4 \text{ mm} \sin(19^\circ) \end{pmatrix} = \begin{pmatrix} 1.3 \text{ mm} \\ 3.8 \text{ mm} \end{pmatrix}$$

in respect to a coordinate system of which the x-axis goes along the visual streak and the area centralis sets the origin. In the cat retina, 1 mm corresponds to 4.4 deg visual angle [7, 10]. Thus

$$\begin{pmatrix} 1.3 \text{ mm} \\ 3.8 \text{ mm} \end{pmatrix} \rightarrow \begin{pmatrix} 5.9^\circ \\ 17.2^\circ \end{pmatrix}.$$

The cortical magnification for elevation 5.9° and azimuth 17.2° is shown in **Fig. 4.1B** and about $0.15 \frac{\text{mm}_c^2}{\text{deg}^2}$. Thus, we can calculate the factor between surface on the retina and on the cortex for the mosaic w81s1.

$$\sqrt{0.15 \frac{\text{mm}_c^2}{\text{deg}^2}} \cdot 4.4 \frac{\text{deg}}{\text{mm}_r} = 1.7 \frac{\text{mm}_c}{\text{mm}_r}$$

Here mm_r means mm on the retina and mm_c means mm on the cortex. The typical scale of a cat OPM is $\Lambda = (1.0 \pm 0.1) \text{ mm}_c$ on the cortex [138]. This value corresponds to $\Lambda_r = (0.59 \pm 0.06) \text{ mm}_r$.

The mosaic m623 has been obtained from 5mm eccentricity and 5.5 deg below the mid line of the visual streak. This corresponds to the point $(2.1^\circ, 22.6^\circ)$ in the visual field, which has the same cortical magnification (within the readout error of **Fig. 4.1B**) and thus $\Lambda_r = (0.59 \pm 0.06) \text{ mm}_r$. Remembering the results from **Fig. 4.3**, we should find a strong angular correlation at least until $\approx 200 \mu\text{m}$. This is not the case. In fact, the experimental data is consistent with the absence of angular correlations. In the next section, we calculate an upper boundary for the value κ .

Figure 4.4: **D** shows the same as C for the mosaic w81s1. **E (a)** shows the circular correlation calculated for a distance of $d = 50 \mu\text{m}$ for both mosaics. Circular correlation is calculated as described in the text. The line shows the expected scale for dipole correlation, 1Λ . For details, see text. **(b)** shows the circular correlation for $d = 80 \mu\text{m}$. The errors in b are substantially smaller because more dipoles can be used to calculate this figure. Errors are calculated by propagation of uncertainty as discussed in the text.

4. APERIODIC RGC MOSAICS AND OPMs

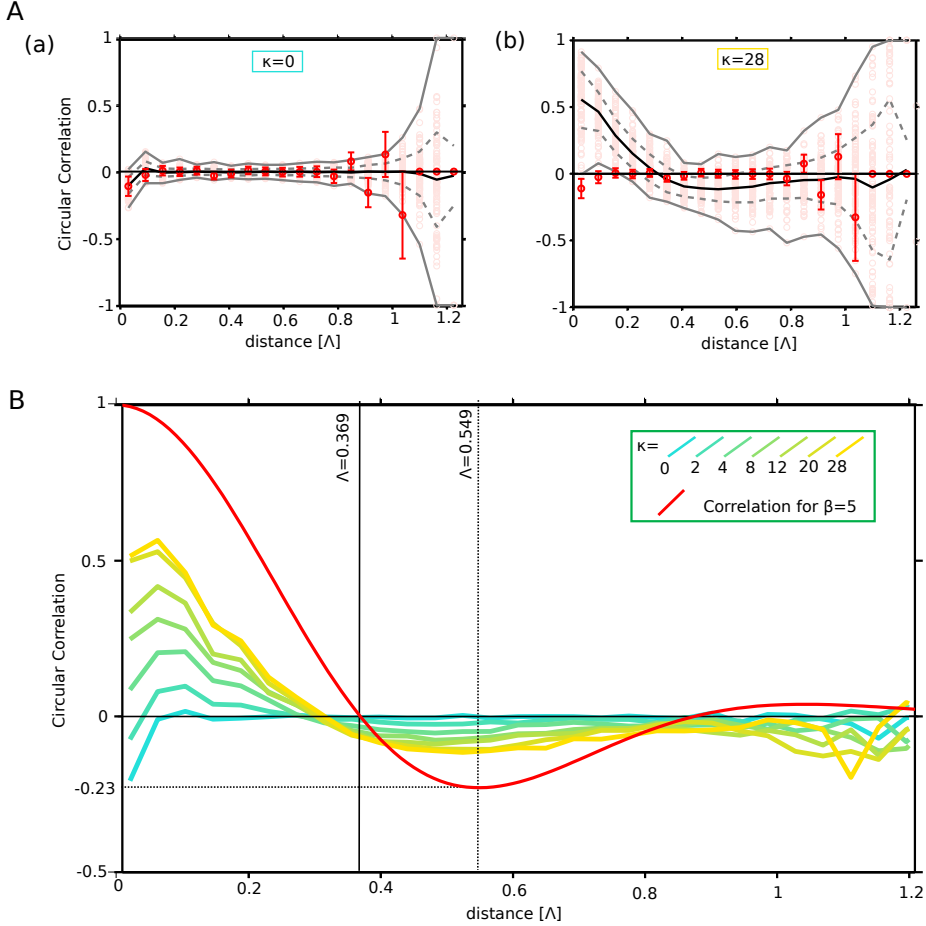


Figure 4.5: **A** Angular correlation function in comparison to data. The pink dots show 100 realizations of the modulated PIPP. The pale pink dots show the values obtained. The black drawn line is the average, the dashed lines show $\pm 1\sigma$. The gray drawn lines show the curve through the maximum/minimum values obtained. The red dots show the correlation for m623. The parameters used are summarized in **Tab. 4.1**. **(a)** calculated for $\kappa = 8$, **(b)** for $\kappa = 28$. **B** The mean correlation function for different values of κ , encoded as color and shown in the legend. The red drawn line is Eqn. (4.3), the theoretical correlation function for a maximum entropy ensemble with a amplitude spectrum parameter $\beta = 5$ [148].

Comparison between PIPP and Data

The cat data shows no indication for a dipole angular correlation. To set a constraint on the tuning parameter κ , we compare the cat data with several realizations of PIPP mosaics. This is done as follows. We choose a cortical magnification factor ξ and a parameter κ . A simulation is initialized by selecting a random position on a simulated OPM [148], calculated as described above. Around this spot, we use a rectangular region of which the size is set by ξ to modulate the PIPP. The values for the PIPP are fixed (and summarized in **Tab. 4.1**). Once the mosaic is generated, we calculate the dipole correlation function. This procedure is repeated 100 times. The cat correlation function is subsequently compared to this data. This is shown in **Fig. 4.5A**. Pink dots show the circular correlation calculated for 100 independent modulated PIPP runs with the m623 parameter set. The gray drawn line connects the maximum and the minimum values. The dashed gray lines mark $\pm 1\sigma$. The drawn black line is the average of the simulations. The data for mosaic m623 with errors estimated by propagation of errors is shown in red. In the case $\kappa = 0$, **Fig. 4.5A (a)**, we find the experimental data consistent with the simulations. **Fig. 4.5A (b)** shows the same modulated PIPP, however, the parameter $\kappa = 28$. In this case we find a strong correlation for dipole distances $\lesssim 0.3\Lambda$. In the case of $\kappa \rightarrow \infty$, we should expect the dipoles' orientation to align exactly with the modulating PIPP. The correlation function should thus approach the correlation function of OPMs. This is shown in **Fig. 4.5B**. The different colors show the mean correlation of 100 modulated PIPP runs for different κ . The red drawn line shows the OPM correlation function for a Gaussian map with marginal amplitude spectrum

$$P_\beta(k) = A|\mathbf{k}|^\beta e^{-|\mathbf{k}|^2 B}$$

where

$$\begin{aligned} A &= 2 \frac{\Gamma\left(\frac{2+\beta}{2}\right)^{1+\beta}}{\Gamma\left(\frac{1+\beta}{2}\right)^{2+\beta}} \\ B &= 2 \frac{\Gamma\left(\frac{2+\beta}{2}\right)^2}{\Gamma\left(\frac{1+\beta}{2}\right)^2}. \end{aligned}$$

These values are chosen to have the amplitude spectrum normalized and to set the expected value to one, $\langle k \rangle = \int P(k) k dk = 1$. The correlation function here is defined for a complex field as $C(\mathbf{r}) = \langle z(\mathbf{x}) \bar{z}(\mathbf{x} + \mathbf{r}) \rangle$. The phase of this complex field is the OPM. Note that this definition is different to the measure used here. The result [148] is

$$C(r) = {}_1F_1\left(\frac{2+\beta}{2}; 1; -\frac{r^2}{4B}\right). \quad (4.3)$$

4. APERIODIC RGC MOSAICS AND OPMs

Here, ${}_1F_1$ is the confluent hypergeometric function of the first kind. Since both measures of angular correlation are similar, we expect both measures to give similar results. The red line in the figure is Eqn. (4.3) calculated for $\beta = 5$ (see **Fig. 4.2**). We find that for increasing κ the dipole correlation function approaches the OPM's correlation function. Since the experimental data is consistent with no correlation at all, we can estimate a greatest possible κ consistent with the observed absence of correlation.

Firstly, we calculate the mean and the standard deviation from the 100 independent realizations of the modulated PIPP. This way, we get a prediction C_i^{mc} and a standard deviation σ_i^{mc} for every bin i . These values are compared to the experiment C_i^{data} . Subsequently, we calculate the average deviation from this prediction in units of standard deviations.

$$\langle \sigma \rangle = \sqrt{\frac{1}{n} \sum_i^n \frac{(C_i^{\text{mc}} - C_i^{\text{data}})^2}{(\sigma_i^{\text{mc}})^2}}. \quad (4.4)$$

Secondly, we calculate the associated probability of finding this value

$$p = 1 - \text{erf}\left(\frac{\langle \sigma \rangle}{\sqrt{2}}\right). \quad (4.5)$$

The result is shown in **Fig. 4.6** for 30 bins. The contour plots, **Fig. 4.6A (a)** and **Fig. 4.6A (b)** show $\langle \sigma \rangle$ calculated with the free parameters κ and cortical magnification. The row below shows the associated probability as calculated with Eqn. (4.5). The cortical magnification which we estimated from the literature is indicated by the red line. **Fig. 4.6A** shows the results for the mosaic m623, **Fig. 4.6B** shows the results for w81s1. We find that for small cortical magnifications, a wider range of κ is allowed as compared to larger cortical magnifications (see (a) left hand side is more blue than right hand side and (b): left hand side is more orange than right hand side). The reason is as follows: If a small region on the retina corresponds to a large region on the cortex, a relatively large area of an OPM is represented by a relatively small mosaic. Therefore despite the strong correlation of OPM with the dipole angle, the angular correlation is relatively small because nearby dipoles can have very different orientations.

For mosaic w81s1, we find that $\kappa < 5$ for which the deviation between Monte-Carlo and experimental data is small and uniform. For increasing κ , the deviation $\langle \sigma \rangle$ increases continuously. For mosaic m623, the quality of the estimation is rather κ independent. This might be an indication that the PIPP is not as good in simulating a mosaic with a great spatial extend as m623. Considering the inhomogeneity of the RGC density on a retina as shown in **Fig. 4.1A**, it is reasonable to assume that as PIPP is better suited for the simulation of small retinal patches where a uniform density is a good approximation.

4.3. Discussion and Conclusion

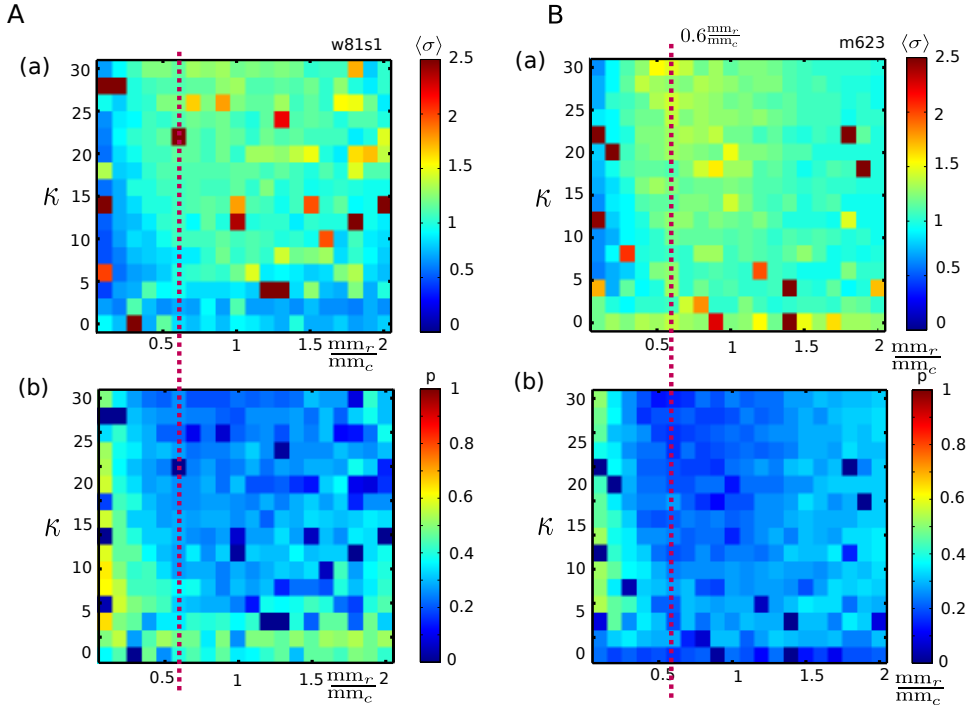


Figure 4.6: Comparison of modulated PIPP correlation functions with experimental data. **A** (a) Shown is the average deviation between experiment and simulation $\langle \sigma \rangle$ as calculated with Eqn. (4.4). **A** (b) The probability of finding the deviation in (a) accidentally. This value is calculated with Eqn. (4.5). **B** The same plots as Fig. A for mosaic m623. The red dashed line indicates the theory value for cortical magnification.

4.3 DISCUSSION AND CONCLUSION

In this chapter we presented a novel method to reverse-engineer a ganglion cell mosaic from a model OPM. The reverse-engineering algorithm builds on previous work on pairwise interacting point processes [48, 76]. After the presentation of the algorithm, we showed that it is possible to find an aperiodic ganglion cell mosaic which generates OPMs with a typical column spacing. We analyzed the statistical properties of the obtained ganglion cell mosaics and found that distance-statistics agree well with experimentally observed mosaics. This is not very surprising because our modification did only address angular correlations. The rest of the PIPP's interaction functions generate realistic mosaics similar to the unmodified one. We also defined a parameter κ which is a natural measure for dipole-OPM influence. For $\kappa \rightarrow 0$, the presented PIPP reproduces the results presented by [48] which is no angular correlation between dipoles, thus no OPM with a typical scale can be created.

4. APERIODIC RGC MOSAICS AND OPMs

For $\kappa \rightarrow \infty$, every dipole angle is very specifically chosen. In this case, there is a long range correlation mirroring the OPM's angular correlation. Generally, it is a requirement for creating an OPM from the ganglion cell mosaic to have angular ON/OFF dipole correlations. After quantifying the correlation function of our model data, we compared the results with experimental data from cat beta cell mosaics [172, 186]. The reason for using beta cells is that they are supposed to have a major influence on the OPM formation [143, 144]. Alternatively, one might use Y cells or parasol/midget cell mosaics for a primate retina. At this point, there is no reason to think of one pathway over the other so that it is a reasonable assumption that all of them contribute to the OPM formation.

The mosaics which we used are not mosaics of receptive field centers but of ganglion cell's somata. We could not find any correlation in retinal beta cell mosaics. Thus, it is unlikely to find them in receptive field center positions, however, it should be checked. A statistical analysis of the tuning parameter κ showed a large region inconsistent with data, in fact we can exclude $\kappa > 5$. This chapter shows that, within certain assumptions, ganglion cell mosaics do not have the necessary spatial statistics to generate OPMs.

CONCLUSIONS

“Nothing shocks me. I’m a scientist.”

Indiana Jones

5. CONCLUSIONS

5.1 CONCLUSION AND PERSPECTIVE

In this thesis we analyzed a new model to account for the universal occurrence of cortical orientation preference maps. Se-Bum Paik and Dario Ringach proposed that ON and OFF center ganglion cell mosaics form two hexagonal lattices with a different lattice constant, shifted against each other by an angle. This creates an interference effect, a Moiré-Pattern. This pattern is mapped into the cortex and creates a map with a typical scale, set by the scale of the Moiré-Pattern. The emergence of a typical scale in this simple geometric model motivated us to conduct a more thorough investigation. The effect of lattice noise on an OPM in the linear feed-forward model has not been well understood. Furthermore, it was not clear if and how the interference model can reproduce the universal properties of OPMs found in different species. We addressed both questions by calculating OPMs, their power spectra and the pinwheel-density analytically. We showed that the pinwheel-density of $\rho = 2\sqrt{3}$ is too large to fit observations in different species. For increasing noise on the ganglion cell mosaic, we showed that the peaks of the Moiré-Modes in the amplitude spectrum are absorbed into a Gaussian background which is inconsistent with experimental data. We also showed that the hexagonal OPMs predicted by the Soodak-Ringach model can be created by self-organization alone. In summary, we presented a series of model predictions which firstly, challenge previous arguments for this model and secondly, stand in contrast to experimental observations. This part of the thesis shows that hexagonal and noisy lattices are unlikely to drive OPM formation.

Stephen Eglen et al. have shown independently that the ganglion cell mosaic is substantially better described by a pairwise interacting point process without long range order than by a hexagonal and noisy lattice. Such a point process generates uncorrelated ON and OFF mosaics. With uncorrelated ON/OFF mosaic, however, it is difficult to account for the typical scale of OPMs. In the second part of the thesis, we asked the question: Which are the properties of ganglion cell mosaics which create realistic OPMs? Can we design a modified PIPP which generates OPMs from two aperiodic lattices? We approached this question by reverse engineering. We calculated model OPMs which we used to seed a PIPP. Thus, we obtained mosaics of which the ON/OFF dipoles' angles correlate strongly with the seeding OPM. Next, we quantified the statistical properties of these mosaics. We found that distance statistics are almost unaffected by our modification. Secondly, we found a strong angular correlation of ON/OFF pairs. We showed that this correlation is necessary because it mirrors the correlation of the underlying OPM. Using published cat beta cell mosaics, we could not find any such correlation in experimental data. We used the missing evidence in the experiment to calculate a constraint on a tuning parameter κ which captures how strongly a ganglion cell mosaic and the OPM interact. In this part of the thesis we showed that observed mosaics do not have the properties to create OPMs.

5.1. Conclusion and Perspective

This thesis presents a series of arguments and observations which lead to the conclusion that this newly proposed model is insufficient to understand the emergence of OPMs. Which are the consequences of this finding? Instead of geometric reasons, crucial features of the spatial layout as the periodicity with typical scale are likely to be formed by cortical self-organization i.e. experience-dependent mechanisms. Current challenges for self-organization models, as the observed finite bandwidth of the amplitude spectrum, might be the effect of retino-thalamic bias. In this sense, it is worth incorporating perturbative effects into self-organization models. Should the white-noise bias from ON/OFF dipoles on self-organized OPM formation not contribute substantially, it is difficult to uphold the idea that retino-thalamic input is important. Understanding the interplay between a retino-thalamic bias and self-organization is crucial and the next logical step following this thesis.

5. CONCLUSIONS

5.2 ZUSAMMENFASSUNG UND AUSBLICK

In dieser Arbeit wurde ein neuartiges Modell untersucht, um das universelle Auftreten von Orientierungskarten zu erklären und zu modellieren. Se-Bum Paik und Dario Ringach schlugen vor, die Mosaiken retinaler ON und OFF center Zellen als hexagonale Gitter zu modellieren. Mit verschiedener Gitterkonstante und/oder gegeneinander verdreht, würde dies einen Interferenzeffekt verursachen, ein sog. Moiré Muster. Dieses Muster würde in den Kortex projiziert und könnte eine Orientierungskarte mit typischer Skala erzeugen. Diese Beobachtung motivierte uns, eine genauere Untersuchung anzustellen. Die Auswirkungen von Störungen auf das retinale Zellmosaik waren in diesem Modell nicht gut verstanden. Es war außerdem nicht klar, wie und ob dieses Modell die universellen Eigenschaften von Orientierungskarten reproduzieren könnte. Beide Fragen wurden in dieser Arbeit adressiert, indem wir Orientierungskarten, ihre Spektren und die Dichte von Pinwheels exakt berechneten. Wir zeigten, dass die Pinwheel Dichte von $\rho = 2\sqrt{3}$ zu groß ist, um die Beobachtungen in verschiedenen Spezies zu erklären. Wir zeigten, dass für zunehmendes Gitterrauschen die scharfen Moiré-Peaks des Spektrums in einen Gaussischen Untergrund absorbieren werden. Ein solcher Untergrund wurde experimentell nicht beobachtet. Wir zeigten außerdem, dass die vom Modell vorhergesagten hexagonalen Orientierungskarten exklusiv durch Selbstorganisation erstellt werden können. Wir präsentierten also eine Reihe von Modellvorhersagen, die (erstens) frühere Argumente für dieses Modell relativieren und (zweitens) im Gegensatz zu experimentellen Daten stehen. Dieser Teil der Arbeit zeigte, dass hexagonale ON/OFF center Zellmosaiken ungeeignet sind, die Bildung von Orientierungskarten zu erklären.

Stephen Eglen und Mitarbeiter haben unabhängig zu dieser Arbeit gezeigt, dass die genannten Ganglionzellmosaiken besser durch paarweise wechselwirkende Punktprozesse ohne langreichweite Ordnung beschrieben werden können als durch hexagonale Gitter. Solche Punktprozesse erzeugen unkorrelierte ON und OFF Mosaiken. Mit unkorrelierten Mosaiken ist es jedoch schwer, die typische Skala einer Orientierungskarte zu generieren. Im zweiten Teil dieser Arbeit adressierten wir also die folgenden Fragen: Erstens, was sind die Eigenschaften von Ganglionzellmosaiken, die realistische Orientierungskarten erzeugen. Zweitens, können wir einen paarweise wechselwirkenden Punktprozess erzeugen, der ein aperiodisches Mosaik erzeugt aus dem sich eine Orientierungskarte erstellen lässt? Wir sind diese Fragen durch Nachkonstruktion nachgegangen. Wir berechneten Modell-Orientierungskarten und verwendeten sie, um einen paarweise wechselwirkenden Punktprozess zu modulieren. Wir erhielten damit Mosaiken, deren ON/OFF Dipole stark mit der Modell-Orientierungskarte korrelierten. Im nächsten Schritt quantifizierten wir die statistischen Eigenschaften dieser Mosaiken. Wir entdeckten, dass die Abstandsstatistik durch unsere Modifikation nahezu unverändert geblieben ist. Außerdem fanden wir eine starke Winkelkorrelation von ON/OFF Dipolen.

5.2. Zusammenfassung und Ausblick

Wir zeigten, dass diese Korrelation notwendig ist, denn sie spiegelt die Korrelation der darunterliegenden Orientierungskarte wieder. Wir versuchten anschließend, eine solche Korrelation in publizierten Daten von Katzen Netzhäuten zu finden. In den experimentellen Daten war kein Hinweis auf Korrelation zu finden. Wir nutzen die Abwesenheit einer Winkelkorrelation um eine Einschränkung für einen Tuningparameter κ zu geben, den wir in dieser Arbeit definierten und der beschreibt, wie stark ON/OFF center Zellmosaike und Orientierungskarte wechselwirken. In diesem Teil der Arbeit zeigten wir, dass Ganglionzellmosaike nicht die Eigenschaften haben, um Orientierungskarte zu erzeugen.

Diese Arbeit präsentiert eine Reihe von Argumenten und Beobachtungen, die zum Schluss führen, dass das untersuchte Modell unzureichend ist um das Auftreten von Orientierungskarten zu erklären. Was sind die Konsequenzen? Anstelle von geometrischen Gründen werden die essentiellen Eigenschaften von Orientierungskarten vermutlich durch kortikale Selbstorganisation geformt. Aktuelle Schwierigkeiten dieser Selbstorganisationmodelle (wie beispielsweise die endliche Bandbreite des Orientierungskartenspektrums) könnten ein Effekt von retinalem Input sein. In diesem Sinne ist es lohnenswert, perturbativen Input in Selbstorganisationsmodellen zu studieren. Das Wechselspiel zwischen retinemalem Input und kortikaler Selbstorganisation ist also der nächste sinnvolle Punkt um nach dieser Arbeit anzusetzen.

5. CONCLUSIONS

5.3 ACKNOWLEDGEMENTS

Mein Dank gilt natürlich Wolfgang Kinzel für seine Offenheit, die aufgebrachte Zeit und die Unterstützung, die es ermöglichen, eine Masterarbeit in Zusammenarbeit mit dem Max-Planck-Institut für Dynamik und Selbstorganisation in Göttingen zu verfassen.

Mein besonderer Dank gilt Fred Wolf, der die Problemstellung dieser Arbeit vorschlug. Seine unermüdliche Neugier und Kritik haben maßgeblich die Qualität dieser Arbeit beeinflusst. Dank bin ich ihm verpflichtet für sein mir entgegengebrachtes Vertrauen in selbstständige Arbeit und die damit einhergehenden Freiheiten, meine eigenen Interessen zu verfolgen; jedoch nie, ohne die ursprüngliche Fragestellung aus den Augen zu verlieren. Wolfgang Keil danke ich für sein stets offenes Ohr, die zahlreichen Diskussionen, nicht nur über Fachliches, die ausgezeichnete Betreuung und die Zeit, die er mir und diesem Projekt gewidmet hat.

Korrektur gelesen haben diese Arbeit Frank Stollmeier, Bettina Hein, Markus Helmer, Michael Seißinger und Wolfgang Keil; herzlichen Dank dafür. Dem Max-Weber Programm danke ich für die mir entgegengebrachte Unterstützung während meines Studiums; selbes gilt für das FOKUS Programm und den DAAD.

BIBLIOGRAPHY

- [1] D L Adams and J C Horton. “Shadows cast by retinal blood vessels mapped in primary visual cortex.” In: *Science* **298** (2002), pp. 572–576.
- [2] J M Alonso, W M Usrey, and R C Reid. “Rules of connectivity between geniculate cells and simple cells in cat primary visual cortex.” In: *The Journal of Neuroscience* **21** (2001), pp. 4002–4015.
- [3] K W Alt, C Jeunesse, and C H Buitrago-Téllez. “Evidence for stone age cranial surgery.” In: *Nature* **387** (1997), pp. 360–361.
- [4] I Amidror. *The Theory of the Moiré Phenomenon, Volume I*. 2nd ed. Springer, 2009, p. 551. ISBN: 9781848821804.
- [5] A Anishchenko et al. “Receptive field mosaics of retinal ganglion cells are established without visual experience.” In: *The Journal of Neurophysiology* **103** (2010), pp. 1856–1864.
- [6] J N Arvesen. “Jackknifing U-statistics.” In: *The Annals of Mathematical Statistics* **40** (1969), pp. 2076–2100.
- [7] H B Barlow, R Fitzhugh, and S W Kuffler. “Change of organization in the receptive fields of the cat’s retina during dark adaptation.” In: *The Journal of Physiology* **137** (1957), pp. 338–354.
- [8] R Bellman. *A Brief Introduction to Theta Functions*. Holt (June 1961), 1961, p. 78. ISBN: 0030103606.
- [9] J Bernstein. *Elektrobiologie: Die Lehre von den elektrischen Vorgängen im Organismus auf moderner Grundlage dargestellt*. Braunschweig: Friedrich Vieweg und Sohn, 1912, p. 280. URL: <http://vlp.mpiwg-berlin.mpg.de/library/data/lit39671?>.
- [10] P O Bishop, W Kozak, and G J Vakkur. “Some quantitative aspects of the cat’s eye: axis and plane of reference, visual field co-ordinates and optics.” In: *The Journal of Physiology* **163** (1962), pp. 466–502.
- [11] H T Blair, A C Welday, and K Zhang. “Scale-invariant memory representations emerge from moiré interference between grid fields that produce theta oscillations: a computational model.” In: *The Journal of Neuroscience* **27** (2007), pp. 3211–3229.
- [12] G G Blasdel. “Orientation selectivity, preference, and continuity in monkey striate cortex.” In: *The Journal of Neuroscience* **12** (1992), pp. 3139–3161.
- [13] G G Blasdel and G Salama. “Voltage-sensitive dyes reveal a modular organization in monkey striate cortex.” In: *Nature* **321** (1986), pp. 579–585.

BIBLIOGRAPHY

- [14] J Boardman, J Griffin, and O Murray. *The Oxford history of the classical world*. Oxford University Press (Juli 1986), 1986, p. 882. ISBN: 0198721129.
- [15] E Bois-Reymond. *Untersuchungen über thierische Elektricität*. Ed. by Georg Reimer. Berlin: Verlag von G. Reimer, 1848, p. 807. URL: <http://vlp.mpiwg-berlin.mpg.de/library/data/lit92?>.
- [16] T Bonhoeffer and A Grinvald. “Iso-orientation domains in cat visual cortex are arranged in pinwheel-like patterns.” In: *Nature* **353** (1991), pp. 429–431.
- [17] T Bonhoeffer and A Grinvald. “The layout of iso-orientation domains in area 18 of cat visual cortex: optical imaging reveals a pinwheel-like organization.” In: *The Journal of Neuroscience* **13** (1993), pp. 4157–4180.
- [18] W H Bosking et al. “Orientation selectivity and the arrangement of horizontal connections in tree shrew striate cortex.” In: *The Journal of Neuroscience* **17** (1997), pp. 2112–2127.
- [19] V Braitenberg and C Braitenberg. “Geometry of orientation columns in the visual cortex.” In: *Biological Cybernetics* **33** (1979), pp. 179–186. URL: <http://www.springerlink.com/index/g7k5231q522r6354.pdf>.
- [20] C E Bredfeldt and D L Ringach. “Dynamics of spatial frequency tuning in macaque V1.” In: *The Journal of Neuroscience* **22** (2002), pp. 1976–1984.
- [21] K Brodmann. *Brodmann's Localisation in the Cerebral Cortex*. Ed. by L J Garey. Springer, 2005. ISBN: 0387269177.
- [22] S R y Cajal. *Comparative study of the sensory areas of the human cortex*. Nabu Press, 2010, 1899, p. 80. ISBN: 1148925902. URL: <http://archive.org/details/comparativestud00cajagoog>.
- [23] S R y Cajal. “Estructura de los centros nerviosos de las aves.” In: *Revista Trimestral de Histología Normal y Patológica* **1** (1888), pp. 1–10.
- [24] B Chapman, I Gödecke, and T Bonhoeffer. “Development of orientation preference in the mammalian visual cortex.” In: *The Journal of Neurobiology* **41** (1999), pp. 18–24.
- [25] B Chapman, M P Stryker, and T Bonhoeffer. “Development of orientation preference maps in ferret primary visual cortex.” In: *The Journal of Neuroscience* **16** (1996), pp. 6443–6453.

BIBLIOGRAPHY

- [26] B Chapman, K R Zahs, and M P Stryker. “Relation of cortical cell orientation selectivity to alignment of receptive fields of the geniculocortical afferents that arborize within a single orientation column in ferret visual cortex.” In: *The Journal of Neuroscience* **11** (1991), pp. 1347–1358.
- [27] P G Clarke and D Whitteridge. “The cortical visual areas of the sheep.” In: *The Journal of Physiology* **256** (1976), pp. 497–508.
- [28] B G Cleland, M W Dubin, and W R Levick. “Simultaneous recording of input and output of lateral geniculate neurones.” In: *Nature* **231** (1971), pp. 191–192.
- [29] B G Cleland and B B Lee. “A comparison of visual responses of cat lateral geniculate nucleus neurones with those of ganglion cells afferent to them.” In: *The Journal of Physiology* **369** (1985), pp. 249–268.
- [30] D M Coppola and L E White. “Visual experience promotes the isotropic representation of orientation preference.” In: *Visual Neuroscience* **21** (2004), pp. 39–51.
- [31] D M Coppola et al. “Unequal representation of cardinal and oblique contours in ferret visual cortex.” In: *PNAS* **95** (1998), pp. 2621–2623.
- [32] M C Crair, D C Gillespie, and M P Stryker. “The role of visual experience in the development of columns in cat visual cortex.” In: *Science* **279** (1998), pp. 566–570.
- [33] M C Crair et al. “Emergence of ocular dominance columns in cat visual cortex by 2 weeks of age.” In: *The Journal of Comparative Neurology* **430** (2001), pp. 235–249.
- [34] M C Crair et al. “Ocular dominance peaks at pinwheel center singularities of the orientation map in cat visual cortex.” In: *Journal of Neurophysiology* **77** (1997), pp. 3381–3385.
- [35] L J Croner and E Kaplan. “Receptive fields of P and M ganglion cells across the primate retina.” In: *Vision Research* **35** (1995), pp. 7–24.
URL: <http://www.ncbi.nlm.nih.gov/pubmed/7839612>.
- [36] D M Dacey. “The mosaic of midget ganglion cells in the human retina.” In: *The Journal of Neuroscience* **13** (1993), pp. 5334–5355.
- [37] D M Dacey and M R Petersen. “Dendritic field size and morphology of midget and parasol ganglion cells of the human retina.” In: *PNAS* **89** (1992), pp. 9666–9670.
- [38] P M Daniel and D Whitteridge. “The representation of the visual field on the cerebral cortex in monkeys.” In: *The Journal of Physiology* **159** (1961), pp. 203–221.

BIBLIOGRAPHY

- [39] J G Daugman. “Uncertainty relation for resolution in space, spatial frequency, and orientation optimized by two-dimensional visual cortical filters.” In: *The Journal of the Optical Society of America* **2** (1985), pp. 1160–1169.
- [40] P Dayan and L F Abbott. *Theoretical Neuroscience*. London, England; Cambridge, Massachusetts: The MIT Press, 2002, p. 460. ISBN: 0262041995.
- [41] J De Carlos and J Borrell. “A historical reflection of the contributions of Cajal and Golgi to the foundations of neuroscience.” In: *Brain Research Reviews* **55** (2007), pp. 8–16.
- [42] G C DeAngelis, I Ohzawa, and R D Freeman. “Receptive-field dynamics in the central visual pathways.” In: *Trends in Neurosciences* **18** (1995), pp. 451–458.
- [43] M R Dennis. “Topological Singularities in Wave Fields.” PhD thesis. University of Bristol, 2001, p. 246. URL: www.bris.ac.uk/physics/media/theory-theses/dennis-mr-thesis.pdf.
- [44] S H DeVries and D A Baylor. “Mosaic arrangement of ganglion cell receptive fields in rabbit retina.” In: *Journal of Neurophysiology* **78** (1997), pp. 2048–2060.
- [45] R L Djavadian and B A Harutiunian-Kozak. “Retinotopic organization of the lateral suprasylvian area of the cat.” In: *Acta Neurobiologiae Experimentalis* **43** (1983), pp. 251–262.
- [46] P M Dunn. “Galen (ad 129–200) of Pergamum: anatomist and experimental physiologist.” In: *Archives of Disease in Childhood-Fetal and Neonatal Edition* **88** (2003), pp. 441–443.
- [47] R Durbin and G Mitchison. “A dimension reduction framework for understanding cortical maps.” In: *Nature* **343** (1990), pp. 644–647.
- [48] S J Eglen, P J. Diggle, and J B Troy. “Homotypic constraints dominate positioning of on-and off-center beta retinal ganglion cells.” In: *Visual Neuroscience* **22** (2005), pp. 859–871.
- [49] C Enroth-Cugell and J G Robson. “The contrast sensitivity of retinal ganglion cells of the cat.” In: *The Journal of Physiology* **187** (1966), pp. 517–552.
- [50] U A Ernst et al. “Intracortical origin of visual maps.” In: *Nature Neuroscience* **4** (2001), pp. 431–436.
- [51] E Erwin, K Obermayer, and K Schulten. “Models of orientation and ocular dominance columns in the visual cortex: A critical comparison.” In: *Neural Computation* **7** (1995), pp. 425–468.
- [52] P Fara. “A microscopic reality tale.” In: *Nature* **459** (2009), pp. 642–644.

BIBLIOGRAPHY

- [53] D Ferster. “Linearity of synaptic interactions in the assembly of receptive fields in cat visual cortex.” In: *Current Opinion in Neurobiology* **4** (1994), pp. 563–568.
- [54] G D Field and E J Chichilnisky. “Information Processing in the Primate Retina: Circuitry and Coding.” In: *Annual Review of Neuroscience* **30** (2007), pp. 1–30.
- [55] N I Fisher and A J Lee. “A correlation coefficient for circular data.” In: *Biometrika* **70** (1983), pp. 327–332.
- [56] N I Fisher and A J Lee. “Time series analysis of circular data.” In: *Journal of the Royal Statistical Society. Series B* **56** (1994), pp. 327–339.
- [57] M Foster and C S Sherrington. *A Text Book of Physiology, Part III.* New York: Macmillan and Co. Limited, 1897, p. 364.
- [58] E H Froeschner. “Two examples of ancient skull surgery.” In: *Journal of Neurosurgery* **76** (1992), pp. 550–552.
- [59] S Gaukroger. *Descartes’ System of Natural Philosophy.* Cambridge; New York: Cambridge University Press, 2002, p. 267. URL: <http://ebooks.cambridge.org/ref/id/CB09780511606229>.
- [60] J L Gauthier et al. “Receptive fields in primate retina are coordinated to sample visual space more uniformly.” In: *PLoS Biology* **7** (2009), e1000063.
- [61] J Gerlach. “Ueber die Struktur der grauen Substanz des menschlichen Grosshirns.” In: *Zentralblatt fuer die medizinischen Wissenschaften* **10** (1872), pp. 273–275.
- [62] S V Girman, Y Sauvé, and R D Lund. “Receptive field properties of single neurons in rat primary visual cortex.” In: *Journal of Neurophysiology* **82** (1999), pp. 301–311.
- [63] I Gödecke et al. “Development of orientation preference maps in area 18 of kitten visual cortex.” In: *The European Journal of Neuroscience* **9** (1997), pp. 1754–1762.
- [64] C Golgi. “Sulla struttura della sostanza grigia del cervello (Comunicazione preventiva).” In: *Gazzetta Medica Italiana, Lombardia* **33** (1873), pp. 244–246.
- [65] S Greenblatt, T Dagi, and M Epstein. *A History of Neurosurgery: In its Scientific and Professional Contexts.* Thieme Medical Publishers, 1997, p. 625.
- [66] A Grinvald et al. “Functional architecture of cortex revealed by optical imaging of intrinsic signals.” In: *Nature* **324** (1986), pp. 361–364.
- [67] C G Gross. “Aristotle on the brain.” In: *The Neuroscientist* **1** (1995), pp. 245–250.

BIBLIOGRAPHY

- [68] F Guterl. “Searching for Clues to Calamity.” In: *New York Times* **20. July** (2012). URL: http://www.nytimes.com/2012/07/21/opinion/the-climate-change-tipping-point.html?_r=0.
- [69] D J Heeger. “Nonlinear model of neural responses in cat visual cortex.” In: *Computational Models of Visual Processing*. Ed. by M Landy and J. A. Movshon. The MIT Press, 1991, p. 406. ISBN: 9780262121552. URL: <http://www.cns.nyu.edu/heegerlab/content/publications/heeger-cmvp91.pdf>.
- [70] H Helmholtz. “Note sur la vitesse de propagation de l’agent nerveux dans les nerfs rachidiens.” In: *Competes Rendus des Seances de l’academie des sciences* **30** (1850), pp. 204–208.
- [71] H Helmholtz. “Vorläufiger Bericht über die Fortpflanzungsgeschwindigkeit der Nervenreizung.” In: *Archiv fuer Anatomie, Physiologie und wissenschaftliche Medicin* (1866), pp. 71–73. URL: <http://vlp.mpiwg-berlin.mpg.de/references?id=lit29168>.
- [72] S Herculano-Houzel. “The remarkable, yet not extraordinary, human brain as a scaled-up primate brain and its associated cost.” In: *PNAS* **109** (2012), pp. 10661–10668.
- [73] P A Hetherington and N V Swindale. “Receptive field and orientation scatter studied by tetrode recordings in cat area 17.” In: *Visual Neuroscience* **16** (1999), pp. 637–652.
- [74] Hippocrates. *The Law, Oath of Hippocrates, On the Surgery, and On the Sacred Disease*. Ed. by Francis Adams. 2009, p. 48. URL: http://en.wikisource.org/wiki/On_the_Sacred_Disease.
- [75] R Hooke. *Micrographia or some physiological Descriptions of Minute Bodies*. London: By the Council of the Royal Society of London for Improving of Natural Knowledge, 1665. URL: <http://www.gutenberg.org/ebooks/15491>.
- [76] V R A Hore, J B. Troy, and S J Eglen. “Parasol cell mosaics are unlikely to drive the formation of structured orientation maps in primary visual cortex.” In: *Visual Neuroscience FirstView* (2012), pp. 1–17.
- [77] J C Horton. “Ocular integration in the human visual cortex.” In: *Canadian Journal of Ophthalmology* **41** (2006), pp. 584–593. URL: <http://www.ncbi.nlm.nih.gov/pubmed/17016529>.
- [78] D H Hubel and T N Wiesel. “Integrative action in the cat’s lateral geniculate body.” In: *The Journal of Physiology* **155** (1961), pp. 385–398.
- [79] D H Hubel and T N Wiesel. “Receptive fields and functional architecture of monkey striate cortex.” In: *The Journal of Physiology* **195** (1968), pp. 215–43.

BIBLIOGRAPHY

- [80] D H Hubel and T N Wiesel. “Receptive fields, binocular interaction and functional architecture in the cat’s visual cortex.” In: *The Journal of Physiology* **160** (1962), pp. 106–154.
- [81] D H Hubel and T N Wiesel. “Receptive fields of cells in striate cortex of very young, visually inexperienced kittens.” In: *The Journal of Physiology* **26** (1963), pp. 994–1002.
- [82] D H Hubel and T N Wiesel. “Receptive fields of single neurones in the cat’s striate cortex.” In: *The Journal of Physiology* **148** (1959), pp. 574–591.
- [83] D H Hubel, T N Wiesel, and S LeVay. “Plasticity of Ocular Dominance Columns in Monkey Striate Cortex.” In: *Philosophical Transactions of the Royal Society B: Biological Sciences* **278** (1977), pp. 377–409.
- [84] M Hübener et al. “Spatial relationships among three columnar systems in cat area 17.” In: *The Journal of Neuroscience* **17** (1997), pp. 9270–9284.
- [85] N P Issa, A Rosenberg, and T R Husson. “Models and measurements of functional maps in V1.” In: *The Journal of Neurophysiology* **99** (2008), pp. 2745–54.
- [86] N P Issa, C Trepel, and M P Stryker. “Spatial frequency maps in cat visual cortex.” In: *The Journal of Neuroscience* **20** (2000), pp. 8504–8514.
- [87] J Jin et al. “Population receptive fields of ON and OFF thalamic inputs to an orientation column in visual cortex.” In: *Nature neuroscience* **14** (2011), pp. 232–238.
- [88] J P Jones and L A Palmer. “An evaluation of the two-dimensional Gabor filter model of simple receptive fields in cat striate cortex.” In: *The Journal of Neurophysiology* **58** (1987), pp. 1233–1258.
- [89] E R Kandel, J H Schwartz, and T M Jessell. *Principles of neural science*. 4th ed. New York: McGraw-Hill New York, 2000, p. 1232.
- [90] Ku Kang, M Shelley, and H Sompolinsky. “Mexican hats and pinwheels in visual cortex.” In: *PNAS* **100** (2003), pp. 2848–2853.
- [91] I Kant. *Kritik der reinen Vernunft*. Riga: Johann Friedrich Hartknoch, 1781. URL: http://de.wikisource.org/wiki/Critik_der_reinen_Vernunft_\%281781\%29.
- [92] J S Karling. “Schleiden’s contribution to the cell theory.” In: *American Naturalist* **73** (1939), pp. 517–537.
- [93] M Kaschube, M Schnabel, and F Wolf. “Self-organization and the selection of pinwheel density in visual cortical development.” In: *New Journal of Physics* **10** (2008), p. 015009.

BIBLIOGRAPHY

- [94] M Kaschube et al. “Genetic influence on quantitative features of neocortical architecture.” In: *The Journal of Neuroscience* **22** (2002), pp. 7206–7217.
- [95] M Kaschube et al. “The pattern of ocular dominance columns in cat primary visual cortex: intra- and interindividual variability of column spacing and its dependence on genetic background.” In: *European Journal of Neuroscience* **18** (2003), pp. 3251–3266.
- [96] M Kaschube et al. “Universality in the evolution of orientation columns in the visual cortex.” In: *Science* **330** (2010), pp. 1113–1116.
- [97] W Keil and F Wolf. “Orientation Preference Maps lack hexagonal symmetry.” In: *To be published* (2012).
- [98] W Keil et al. “Response to Comment on ”Universality in the Evolution of Orientation Columns in the Visual Cortex”.” In: *Science* **336** (2012), pp. 413–413.
- [99] C Kittel. *Introduction to Solid State Physics*. 8th ed. Wiley, 2004, p. 704.
- [100] H Kolb. *The Organization of the retina and visual system*. 2007. URL: <http://webvision.med.utah.edu/book/>.
- [101] A A Koulakov and D B Chklovskii. “Orientation preference patterns in mammalian visual cortex: a wire length minimization approach.” In: *Neuron* **29** (2001), pp. 519–527.
- [102] A Leewenhoek. “Microscopical Observations of Mr. Leewenhoek, Concerning the Optic Nerve.” In: *Philosophical Transactions of the Royal Society of London* **10** (1675), pp. 378–380. URL: <http://rstl.royalsocietypublishing.org/cgi/doi/10.1098/rstl.1675.0032>.
- [103] S LeVay and M P Stryker. “The development of ocular dominance columns in the cat.” In: *Society for Neuroscience Symposia* **4** (1979), pp. 83–98.
- [104] R Linsker. “From basic network principles to neural architecture: emergence of orientation columns.” In: *PNAS* **83** (1986), pp. 8779–8783.
- [105] R Linsker. “From basic network principles to neural architecture: emergence of orientation-selective cells.” In: *PNAS* **83** (1986), pp. 8390–8394.
- [106] R Linsker. “From basic network principles to neural architecture: emergence of spatial-opponent cells.” In: *PNAS* **83** (1986), pp. 7508–7512.
- [107] F Lopez-Munoz et al. “The pineal gland as physical tool of the soul faculties: A persistent historical connection.” In: *Neurologia* **27** (2012), pp. 161–168.
- [108] A Magnus. *Philosophia pauperum, sive Philosophia naturalis*.

BIBLIOGRAPHY

- [109] H A Mallot. “An Overall Description of Retinotropic Mapping in the Cat’s Visual Cortex Areas 17, 18 and 19.” In: *Biological Cybernetics* **52** (1985), pp. 45–51.
- [110] R H Masland. “The fundamental plan of the retina.” In: *Nature Neuroscience* **4** (2001), pp. 877–886.
- [111] J A Mazer et al. “Spatial frequency and orientation tuning dynamics in area V1.” In: *PNAS* **99** (2002), pp. 1645–1650.
- [112] P Mazzarello. “A unifying concept: the history of cell theory.” In: *Nature Cell Biology* **1** (1999), E13–5.
- [113] B A McGuire et al. “Targets of horizontal connections in macaque primary visual cortex.” In: *The Journal of Comparative Neurology* **305** (1991), pp. 370–392.
- [114] N D Mermin. “The topological theory of defects in ordered media.” In: *Reviews of Modern Physics* **51** (1979), pp. 591–648.
- [115] S. Mikula et al. *A digital stereotaxic atlas of the brain of the monkey, Macaca mulatta*. 2012. URL: www.brainmaps.org.
- [116] K D Miller. “A model for the development of simple cell receptive fields and the ordered arrangement of orientation columns through activity-dependent competition between ON- and OFF-center inputs.” In: *The Journal of Neuroscience* **14** (1994), pp. 409–441.
- [117] K D Miller. “ π = visual cortex.” In: *Science* **330** (2010), pp. 1059–1060.
- [118] J Milton. *Paradise Lost*. 1667. URL: http://en.wikisource.org/wiki/Paradise_Lost_\%281674\%29.
- [119] J A Movshon, I D Thompson, and D J Tolhurst. “Spatial and temporal contrast sensitivity of neurones in areas 17 and 18 of the cat’s visual cortex.” In: *The Journal of Physiology* **283** (1978), pp. 101–120.
- [120] T Müller et al. “An analysis of orientation and ocular dominance patterns in the visual cortex of cats and ferrets.” In: *Neural Computation* **12** (2000), pp. 2573–95.
- [121] E H Murphy and N Berman. “The rabbit and the cat: a comparison of some features of response properties of single cells in the primary visual cortex.” In: *The Journal of Comparative Neurology* **188** (1979), pp. 401–427.
- [122] W Nernst. “Die elektromotorische Wirksamkeit der Ionen.” In: *Zeitschrift für physikalische Chemie* **4** (1899), pp. 9–181. URL: <http://electrochem.cwru.edu/estir/hist/hist-13-Nernst-1.pdf>.

BIBLIOGRAPHY

- [123] W Nernst. “Zur Theorie des elektrischen Reizes.” In: *Archiv für die gesamte Physiologie des Menschen und der Tiere* **122** (1897), pp. 275–314. URL: <http://link.springer.com/article/10.1007\%2FBF01677956?LI=true>.
- [124] Y Nishijima and G Oster. “Moire Patterns: Their Application to Refractive Index and RefractiveIndex Gradient Measurements.” In: *The Journal of the Optical Society of America* **54** (1964), pp. 1–5.
- [125] S Nishimoto et al. “Reconstructing visual experiences from brain activity evoked by natural movies.” In: *Current Biology* **21** (2011), pp. 1641–1646.
- [126] K Obermayer and G G Blasdel. “Singularities in primate orientation maps.” In: *Neural Computation* **9** (1997), pp. 555–575.
- [127] K Obermayer, G G Blasdel, and K Schulten. “Statistical-mechanical analysis of self-organization and pattern formation during the development of visual maps.” In: *Physical Review A* **45** (1992), pp. 7568–7589.
- [128] K Obermayer, H Ritter, and K Schulten. “A principle for the formation of the spatial structure of cortical feature maps network layer input layer.” In: *PNAS* **87** (1990), pp. 8345–8349.
- [129] K Ohki et al. “Functional imaging with cellular resolution reveals precise micro-architecture in visual cortex.” In: *Nature* **433** (2005), pp. 597–603.
- [130] K Ohki et al. “Highly ordered arrangement of single neurons in orientation pinwheels.” In: *Nature* **442** (2006), pp. 925–928.
- [131] S B Paik and D L Ringach. “Link between orientation and retinotopic maps in primary visual cortex.” In: *PNAS* **109** (2012), pp. 7091–7096.
- [132] S B Paik and D L Ringach. “Retinal origin of orientation maps in visual cortex.” In: *Nature Neuroscience* **14** (2011), pp. 919–925.
- [133] S B Paik et al. *Analysis of ON/OFF-dipole spatial statistics in retinal ganglion cell mosaics*. 2012.
- [134] J G Parnavelas, R A Burne, and C S Lin. “Receptive field properties of neurons in the visual cortex of the rat.” In: *Neuroscience Letters* **27** (1981), pp. 291–296.
- [135] B N Pasley et al. “Reconstructing speech from human auditory cortex.” In: *PLoS Biology* **10** (2012), e1001251.
- [136] J Pevsner. “Leonardo da Vinci’s contributions to neuroscience.” In: *Trends in Neurosciences* **25** (2002), pp. 217–220.
- [137] M Piccolino. “Luigi Galvani and animal electricity: two centuries after the foundation of electrophysiology.” In: *Trends in Neurosciences* **20** (1997), pp. 443–448.

BIBLIOGRAPHY

- [138] S Rathjen, K E Schmidt, and S Löwel. “Postnatal growth and column spacing in cat primary visual cortex.” In: *Experimental Brain Research* **149** (2003), pp. 151–158.
- [139] L Reichl et al. “Coordinated optimization of visual cortical maps (I) Symmetry-based analysis.” In: *PLoS Computational Biology* **8** (2012), e1002466.
- [140] L Reichl et al. “Coordinated optimization of visual cortical maps (II) Numerical studies.” In: *PLoS Computational Biology* **8** (2012), e1002756.
- [141] R C Reid and J M Alonso. “Specificity of monosynaptic connections from thalamus to visual cortex.” In: *Nature* **378** (1995), pp. 281–283.
- [142] F P Retief and C Cilliers. “The influence of Christianity on Graeco-Roman medicine up to the Renaissance.” In: *Acta Theologica Supplementum* **7** (2005), pp. 259–277.
- [143] D L Ringach. “Haphazard wiring of simple receptive fields and orientation columns in visual cortex.” In: *The Journal of Neurophysiology* **92** (2004), pp. 468–476.
- [144] D L Ringach. “On the origin of the functional architecture of the cortex.” In: *PLoS one* **2** (2007), e251.
- [145] R W Rodieck. “Quantitative analysis of cat retinal ganglion cell response to visual stimuli.” In: *Vision Research* **5** (1965), pp. 583–601.
- [146] M H Rowe and J Stone. “Properties of ganglion cells in the visual streak of the cat’s retina.” In: *The Journal of Comparative Neurology* **169** (1976), pp. 99–125.
- [147] J D Schall, V H Perry, and A G Leventhal. “Ganglion cell dendritic structure and retinal topography in the rat.” In: *The Journal of Comparative Neurology* **257** (1987), pp. 160–165.
- [148] M Schnabel et al. “Random waves in the brain: Symmetries and defect generation in the visual cortex.” In: *The European Physical Journal Special Topics* **145** (2007), pp. 137–157.
- [149] T Schwann. *Mikroskopische Untersuchungen über die Übereinstimmung in der Struktur und dem Wachstum der Tiere und Pflanzen*. Vdm Verlag Dr. Müller; Auflage: 1 (2006), 1839, p. 248. ISBN: 3836401266.
- [150] P Series, P E Latham, and A Pouget. “Tuning curve sharpening for orientation selectivity: coding efficiency and the impact of correlations.” In: *Nature Neuroscience* **7** (2004), pp. 1129–1135.
- [151] A Shmuel and A Grinvald. “Coexistence of linear zones and pinwheels within orientation maps in cat visual cortex.” In: *PNAS* **97** (2000), pp. 5568–5573.

BIBLIOGRAPHY

- [152] H Z Shouval et al. “Structured long-range connections can provide a scaffold for orientation maps.” In: *The Journal of Neuroscience* **20** (2000), pp. 1119–1128.
- [153] R E Soodak. “The retinal ganglion cell mosaic defines orientation columns in striate cortex.” In: *PNAS* **84** (1987), pp. 3936–3940.
- [154] R E Soodak. “Two-dimensional modeling of visual receptive fields using Gaussian subunits.” In: *PNAS* **83** (1986), pp. 9259–9263.
- [155] H Spitzer, R Desimone, and J Moran. “Increased attention enhances both behavioral and neuronal performance.” In: *Science* **240** (1988), pp. 338–340.
- [156] P Sterling. “Microcircuitry of the cat retina.” In: *Annual Review of Neuroscience* **6** (1983), pp. 149–185.
- [157] R Sullivan. “The identity and work of the ancient Egyptian surgeon.” In: *The Journal of the Royal Society of Medicine* **89** (1996), pp. 467–473.
- [158] N V Swindale. “A model for the coordinated development of columnar systems in primate striate cortex.” In: *Biological Cybernetics* **230** (1992), pp. 217–230.
- [159] N V Swindale. “A model for the formation of orientation columns.” In: *Proceedings of the Royal Society of London. Series B* **215** (1982), pp. 211–230.
- [160] N V Swindale. “Orientation tuning curves: empirical description and estimation of parameters.” In: *Biological Cybernetics* **78** (1998), pp. 45–56.
- [161] N V Swindale. “The development of topography in the visual cortex: a review of models.” In: *Network: Computation in Neural Systems* **7** (1996), pp. 161–247.
- [162] M Takao. “Changes in Visual Response Properties of Cat Retinal Ganglion Cells within Two Weeks after Axotomy.” In: *Experimental Neurology* **177** (2002), pp. 171–182.
- [163] R B Tootell et al. “Deoxyglucose analysis of retinotopic organization in primate striate cortex.” In: *Science* **218** (1982), pp. 902–904.
- [164] J B Troy and T Shou. “The receptive fields of cat retinal ganglion cells in physiological and pathological states: where we are after half a century of research.” In: *Progress in Retinal and Eye Research* **21** (2002), pp. 263–302.
- [165] D Y Ts’o et al. “Functional organization of primate visual cortex revealed by high resolution optical imaging.” In: *Science* **249** (1990), pp. 417–420.

BIBLIOGRAPHY

- [166] R J Tusa, L A Palmer, and A C Rosenquist. “The retinotopic organization of area 17 (striate cortex) in the cat.” In: *The Journal of Comparative Neurology* **177** (1978), pp. 213–235.
- [167] S D Van Hooser et al. “Orientation selectivity without orientation maps in visual cortex of a highly visual mammal.” In: *The Journal of Neuroscience* **25** (2005), pp. 19–28.
- [168] A Verkhratsky, O A Krishtal, and O H Petersen. “From Galvani to patch clamp: the development of electrophysiology.” In: *Pflugers Archiv : European Journal of Physiology* **453** (2006), pp. 233–247.
- [169] A Vesalius. *De humani corporis fabrica libri septem 3/7 (On the fabric of the human body in seven books 3/7)*. Ed. by W F Richardson and J B Carman. Jeremy Norman Co., Edition 2003, 1543, p. 286. ISBN: 0930405838. URL: http://books.google.de/books?id=eJI1A70WeKsC&pg=PA163&source=gbs_toc_r&cad=4#v=onepage&q&f=false.
- [170] R L K Virchow. *Die Cellularpathologie*. Nabu Press, Edition from 2010, 1858, p. 494. ISBN: 1142274896.
- [171] H Wässle. “Parallel processing in the mammalian retina.” In: *Nature Reviews Neuroscience* **5** (2004), pp. 747–757.
- [172] H Wässle, B B Boycott, and R B Illing. “Morphology and mosaic of on- and off-beta cells in the cat retina and some functional considerations.” In: *Proceedings of the Royal Society of London. Series B* **212** (1981), pp. 177–195.
- [173] H Wässle, W R Levick, and B G Cleland. “The distribution of the alpha type of ganglion cells in the cat’s retina.” In: *The Journal of Comparative Neurology* **159** (1975), pp. 419–438.
- [174] H Wässle, L Peichl, and B B Boycott. “Morphology and topography of on- and off-alpha cells in the cat retina.” In: *Proceedings of the Royal Society of London. Series B* **212** (1981), pp. 157–175.
- [175] H Wassle, L Peichl, and BB Boycott. “A spatial analysis of on-and off-ganglion cells in the cat retina.” In: *Vision Research* **23** (1983), pp. 1151–1160.
- [176] E. W. Weisstein. *Jacobi Theta Functions*. URL: <http://mathworld.wolfram.com/JacobiThetaFunctions.html> (visited on 2012).
- [177] L E White, D M Coppola, and D Fitzpatrick. “The contribution of sensory experience to the maturation of orientation selectivity in ferret visual cortex.” In: *Nature* **411** (2001), pp. 1049–1052.
- [178] L E White and D Fitzpatrick. “Vision and cortical map development.” In: *Neuron* **56** (2007), pp. 327–338.

BIBLIOGRAPHY

- [179] E T Whittaker and G N Watson. *Course of Modern Analysis*. 4th ed. Cambridge University Press, 2009, p. 620.
- [180] F Wolf. “Symmetry, Multistability, and Long-Range Interactions in Brain Development.” In: *Physical Review Letters* **95** (2005), pp. 1–4.
- [181] F Wolf and T Geisel. “Spontaneous pinwheel annihilation during visual development.” In: *Nature* **395** (1998), pp. 73–78.
- [182] F Wörgötter and U T Eysel. “Quantitative determination of orientational and directional components in the response of visual cortical cells to moving stimuli.” In: *Biological Cybernetics* **355** (1987), pp. 349–355.
- [183] F Wörgötter and C Koch. “A detailed model of the primary visual pathway in the cat: comparison of afferent excitatory and intracortical inhibitory connection schemes for orientation selectivity.” In: *The Journal of Neuroscience* **11** (1991), pp. 1959–1979.
- [184] X Xu et al. “Functional organization of visual cortex in the owl monkey.” In: *The Journal of Neuroscience* **24** (2004), pp. 6237–6247.
- [185] E Yacoub, N Harel, and K Ugurbil. “High-field fMRI unveils orientation columns in humans.” In: *PNAS* **105** (2008), pp. 10607–10612.
- [186] X J Zhan and J B Troy. “Modeling cat retinal beta-cell arrays.” In: *Visual Neuroscience* **17** (2000), pp. 23–39.
- [187] J X Zhang et al. “The representation of complex images in spatial frequency domains of primary visual cortex.” In: *The Journal of Neuroscience* **27** (2007), pp. 9310–9318.

Erklärung

Hiermit bestätige ich, **Manuel Schottdorf**, dass ich die vorliegende Arbeit selbstständig und nur mit den angegebenen Hilfsmitteln erstellt habe und dass ich sie erstmalig als Prüfungsleistung verwende.

Würzburg, den 1. Dezember 2012

Manuel Schottdorf